6-1-1994

State-of-the-Practice and Instability Analysis of Single-Layer Aluminum Latticed Geodesic Domes

A. K. Maze

C. N. Kostem

Recommended Citation

Maze, A. K. and Kostem, C. N., "State-of-the-Practice and Instability Analysis of Single-Layer Aluminum Latticed Geodesic Domes" (1994). ATLSS Reports. ATLSS report number 94-07:.
http://preserve.lehigh.edu/engr-civil-environmental-atlss-reports/199

ATLSS

ADVANCED TECHNOLOGY FOR
LARGE
STRUCTURAL SYSTEMS

Lehigh University

STATE-OF-THE-PRACTICE
AND
INSTABILITY ANALYSIS OF SINGLE-LAYER ALUMINUM LATTICED GEODESIC DOMES

by

A. K. Maze
Research Assistant

C. N. Kostem
Professor of Civil Engineering

ATLSS Report No. 94-07

June 1994

ATLSS Engineering Research Center
Lehigh University
117 ATLSS Dr., Imbt Laboratories
Bethlehem, PA 18015-4729
(610) 758-3525

An NSF Sponsored Engineering Research Center

TABLE OF CONTENTS

Page

ACKNOWLEDGEMENTS iii

ABSTRACT iv

1. INTRODUCTION 1-1
    1.1 Background 1-1
    1.2 Objectives 1-3
    1.3 Specific Details
        1.3.1 Overview Of The Dome Being Studied 1-3
        1.3.2 Geometric Properties 1-3
        1.3.3 Material Properties 1-5
        1.3.4 Loading Characteristics 1-5
    Section 1 Figures 1-6

2. STATE-OF-THE-PRACTICE 2-1
    2.1 Focus 2-1
    2.2 Mathematical Model Assessments 2-2
        2.2.1 Background 2-2
        2.2.2 Continuous Mathematical Models- General Instability 2-2
            2.2.2A Conventional Shell Theory 2-2
            2.2.2B Equivalent Shell Theory 2-3
            2.2.2C Split Rigidity Method 2-3
    2.2.3 Discrete Mathematical Models- General Instability 2-5
            2.2.3A Finite Difference Analysis 2-5
            2.2.3B Matrix Formulation 2-5
    2.3 Finite Element Analysis Applicability 2-6
        2.3.1 Background 2-6
        2.3.2 Bifurcation Buckling Approach 2-7
        2.3.3 Newton-Raphson Technique 2-8
        2.3.4 Riks-Wempner Technique 2-9
    2.4 Nonlinear Solution Feasibility 2-10
    2.5 Linear vs Nonlinear Finite Element Analysis 2-10
    Section 2 Figures 2-12

TABLE OF CONTENTS (continued)

Page

3. FINITE ELEMENT CASE STUDY 3-1
  3.1 Background 3-1
  3.2 Orientation 3-1
  3.3 Modeling Information 3-2
    3.3.1 Nodes 3-2
    3.3.2 Spars 3-2
    3.3.3 Cladding 3-3
    3.3.4 Base Support 3-3
    3.3.5 Spar Lateral Constraint 3-3
    3.3.6 Model Optimization 3-3
    3.3.7 Geometric/Material Information 3-4
  3.4 Loading Information 3-4
  3.5 Solution Evaluation Information 3-5
  3.6 Load Cases 3-6
  3.7 Finite Element Results 3-6
    3.7.1 DSNLB Results 3-6
    3.7.2 DSNLCB Results 3-9
    3.7.3 DHSNLB Results 3-11
    3.7.4 DHSNLCB Results 3-13
  3.8 Comparison of Runs 3-16
  Section 3 Figures (Supplement) 3-18

4. CRITICAL BUCKLING EQUATION MODIFICATION 4-1
  4.1 Background 4-1
  4.2 Assumptions 4-1
  4.3 Modification Formulation 4-2
  Section 4 Figures 4-4

5. SUMMARY 5-1
  5.1 Conclusions 5-1
  5.2 Recommendations 5-2
  5.3 Closing Comments 5-2
  Section 5 Figures 5-3

REFERENCES R-1

ACKNOWLEDGEMENTS

The study reported herein was jointly funded by Conservatek Industries, Inc., of Conroe, TX, and the ATLSS Center. In addition, The TGB Partnership of Hillsborough, NC, an engineering consultant to Conservatek, contributed its knowledge and expertise to the study. This report describes the research and studies done from April 1993 through May 1994.

We acknowledge Steve Ducotey from Conservatek and Rob Ferry and Randy Kissell from The TGB Partnership for their cooperation, guidance, and time and effort in providing information crucial to the study.

At Lehigh, we express our thanks to our Project Coordinator, Dr. John E. Bower, for his support and encouragement. We are especially grateful to Mr. Peter Y. Bryan, for his assistance with the computer systems used in the study. The assistance of Mr. Richard Sopko and Mr. John Gera in the visual aspects of the report is also acknowledged. A final word of thanks goes out to graduate student Mr. Michael Hebor and post-doctorate research engineer Dr. Took Kwon (Mike) Sooi for their assistance in the research.

ABSTRACT

The first part of this study focuses on the techniques and mathematical models available to gain analytical knowledge pertaining to the performance of single layer aluminum latticed spherical domes.

After this State-of-the-Practice review, the second part of this study uses a computer-based ANSYS nonlinear finite element analysis in order to determine the snap-through instability of a particular spherical geodesic dome geometry. Comparisons between a cladded and bare-frame dome, and full and half surface snow load provided a better understanding of the critical response of these structures.

Through correlations with the finite element results, simplified continuum-based expressions used to determine dome design parameters were reevaluated, resulting in modified expressions which can be used for the determination of structural parameters of certain single layer latticed aluminum geodesic domes.

1. INTRODUCTION

1.1 BACKGROUND

Domes have given the engineer the opportunity to enclose vast areas without the use of intermediate supports which would detract from the overall usefulness of the enclosed space [20]. Developed by Buckminster Fuller in the early 1950's, the single layer geodesic dome is perhaps one of the most efficient structural configurations of all the dome types. With the advent of lightweight structural materials such as aluminum, the advantages of grid construction are found to be quite numerous. The geodesic configuration is based upon the principle of triangular shapes superimposed upon a spherical surface of revolution. The inherent stiffness of the triangle, coupled with the forementioned light-weight of aluminum alloys, results in a structure which does not require any main beams or girders. In addition, the use of a domic shape allows for a reduction in the overall depth of the structure, which translates into a reduction of the amount of material required for completion of the structure. The repetitious use of triangles in the geodesic dome concept is one of the main advantages of the application. Since the surface is composed of "nearly equilateral" triangles arranged in a cyclic fashion, fabrication of individual members is greatly simplified due to the overall geometric similarity of each and every member in the dome.

As mentioned previously, the use of a dome-like structure allows for a great reduction in the overall structural depth of the system. This reduction in depth has been the focus of many "questions" which have developed over the past few decades. Research needs to be continued in order to conclusively determine how shallow a dome can be designed without sacrificing the overall integrity of the structure. When dealing with stability of domes and domelike structures, the possibility of buckling on both a global and local level do exist. It is because of this stability situation that the need for further clarification of critical issues should be addressed. These and related issues form the foundation of the research on which this report is based.

1.2 OBJECTIVES

The research which was performed can be organized into three distinct studies. The first study incorporated a literature search in which the primary objective was to summarize the current state-of-the-practice for the design, construction, and performance of single layer aluminum latticed spherical domes. This investigation addressed the following issues:

1. Identification and critique of various continuous and discrete mathematical models to assess the critical limits of the structure.

2. Applicability of finite element analysis in order to investigate structural instability and predict related collapse loads and modes of failure.

3. Evaluation of the suitability of nonlinear solution techniques in order to determine critical response of the system which in itself may exhibit geometric and/or material nonlinearity.

The second study was associated with the finite element analysis of a specific single layer aluminum geodesic dome. The assumptions and other details corresponding to the actual model are presented in Section 3 of the report. The finite element analyses were performed using the **ANSYS** finite element package [4]. Due to the complex nature of the problem, a tremendous amount of data was generated corresponding to the overall performance of the dome from its service load to the critical load corresponding to collapse of the structural system. It is through these analyses that the understanding of the performance and limitations of the dome can be brought to light. The objective of the finite element analyses performed for this research project was to supplement the knowledge base which already exists on the subject of latticed domes. The results obtained from the finite element runs are definitely not meant to stand alone, nor should they be used as the "final say" when it comes to making conclusive decisions about overall performance of the structure.

The final phase of this research was mathematically based in that it incorporated many of the findings of the first two phases in order to "fine tune" the expression used to determine the Wright / Buchert critical pressure expression for elastic buckling of a spherical isotropic shell-like structure [6,8] where

$$P_{cr} = 1.55 \frac{AEr}{LR^2} \tag{1.1}$$

P_{cr} = Critical buckling pressure normal to the surface, (ksi)
A = Strut cross-sectional area, (in^2)
E = Modulus of elasticity of the material, (ksi)
r = Radius of gyration of the strut, (in)
L = Average length of strut, (in)
R = Radius of curvature of the dome, (in)

This expression is also given in the Guide to Stability Design Criteria for Metal Structures, 4th Edition [13]. Of the many researchers who have investigated the theory behind the equation, the main area of concern falls in the interpretation of the proper value of the buckling coefficient, **C**. From the expression above, it is seen that a value of 1.55 is used for the buckling coefficient, as suggested by both Douglas Wright and Kenneth Buchert [13]. Through the use of a computer-based finite element formulation, the critical behavior of a lattice dome with a triangular pattern can be observed and evaluated. From this, corresponding values for the critical buckling coefficient can be interpolated, and a modification of the equivalent shell theory expression can be considered.

1.3 SPECIFIC DETAILS

1.3.1 OVERVIEW OF THE DOME BEING STUDIED

Although the following research can be applied, in some way or another, to many different dome types, the primary focus of the study was a single dome type. The structure itself, as previously noted, is of a geodesic configuration which closely resembles patterns which are formed in nature [17]. The mathematical principles on which the geodesic dome is formed gives way to force distributions similar to those found on the atomic level. This, in turn, means that the geodesic configuration would give rise to structures which would be the strongest, have the highest strength-to-weight ratio, and be the most cost effective structures of its type [15]. It is quite obvious that the inherent advantages of the geodesic configuration tend toward the use of lightweight materials which would further improve its overall effectiveness in reality. Because of this, the use of aluminum is commonplace in the construction of these domes.

1.3.2 GEOMETRIC PROPERTIES

In all areas of the research which necessitate reference to a particular dome for analytical purposes, it has been decided through a cooperative agreement between ATLSS and Conservatek Industries, Inc. that the Conservatek Alumadome would serve as the benchmark structure for this study. The particular structure being scrutinized (Fig 1.1) has an overall diameter of 226.35 feet and rise of 40.36 feet, which gives it a rise-to-span ratio slightly under 20% (0.178 exactly). This dome is therefore classified as a shallow dome which leads to the likeliness of structural instability when subjected to extreme loading conditions [17]. The particular Alumadome has an overall surface area of 45,000 ft^2 and spans an area of approximately 40,000 ft^2. The dome itself is composed of 1,372 struts, 896 cladding panels, and 477 connector hubs, which together, give the structure a dead weight of 134,039 pounds, or 2.9 lb/ft^2 distributed uniformly over the entire surface.

Three different strut sizes are incorporated into the structure. Each strut in the dome has a web depth of 8 inches and the web thicknesses vary between 0.20, 0.25, and 2.25 inches, respectively. Differing flange widths and thicknesses are paired with the forementioned web sizes to form the three strut groups (group # designated by Conservatek) mentioned above:

Strut Group	Depth	Web Thickness	Flange Width	Flange Thickness
483	8"	0.20"	4.0"	0.25"
487	8"	0.25"	4.5"	0.30"
489	8"	2.25"	4.5"	0.30"

Group 483 forms the majority of the struts in the structure. These beams form the entire dome, with the exception of the bottom layer of diagonal (compression) members and the tension ring at the very bottom of the structure. The lower compression members are composed of strut group 487, while the tension ring is formed from struts of group 489. Altogether, the entire family of struts account for 58.4% of the overall weight of the dome (78,213 pounds).

The cladding panels which cloak the entire outer surface of the dome are 0.05 inch thick and account for 23.6% of the entire weight (31,645 pounds). Although the cladding accounts for almost ¼ of the weight of the dome, it does not contribute much to the overall integrity of the structure, as proven by the comparison of finite element results between cladded and uncladded models presented in Section 3 of the report. The cladding thickness contributes little resistance to bending, which leaves the cladding to act primarily through membrane action, which in itself does little good for the structure [28]. The cladding's main function is aesthetic in that it protects against vapor leakage and keeps out contaminants (industrial applications) from whatever the dome is covering. The effect of the cladding will be discussed more thoroughly in the section dealing with finite element analysis of the dome.

The 477 connector hubs used in this particular dome account for 3% of the overall weight (3,911 pounds). The hubs attach to all interconnecting beams through top and bottom flanges and are assumed, with much hesitancy, to exhibit full fixity within all finite element models. The degree of hub fixity is an ongoing (and valid) source of controversy within the realm of dome research, yet it falls outside the scope of this report. Dome joint fixity is a complex issue in itself, and the foundation of a completely independent research project can be formed upon its merit alone.

The batten bars (20,270 pounds) make up the remaining 15% of the overall structural weight. The function of these bars is to provide a sealing and clamping mechanism for the cladding onto the top flanges of the strut members. They are considered to be non-structural elements.

The final area of the dome which needs to be given attention is the support mechanism (Fig. 1.2). The structure is supported on a pinned and slotted mounting bracket through which movement is allowed in a horizontal (radial) direction. The dome is connected to the mounting bracket via 56 8" X 4" X 1/2" aluminum box beams (6 inches long) at each base support point. The option of a fixed support system is available for this dome configuration, but more critical results will be obtained by using the slotted support option. Thus, all finite element models will employ a slotted support condition.

1.3.3 MATERIAL PROPERTIES

All structural elements, excluding the cladding, are series 6061 aluminum alloy. This alloy has a yield stress of 40 ksi and a Young's modulus of 10,100 ksi. The cladding is series 3003 aluminum alloy possessing a yield stress of 25 ksi and an elastic modulus of 10,100 ksi. The strain hardening moduli of both series are extremely low (43 ksi and 21 ksi, respectively). As a result, after elements have yielded, they are considered failed due to the fact that they cannot carry any significant additional load and because they effectively have zero stiffness. Due to the performance characteristics of this material, a bilinear stress-strain curve is used to define the material within the finite element models in order to account for the possibility of nonlinear behavior induced by material nonlinearity.

1.3.4 LOADING CHARACTERISTICS

There are many types and/or combinations of loads which can be imposed upon the domed structure. Snow and wind loads are perhaps the most common, but they are not the only contributors. Seismic loading is an additional possibility which should be considered if the structure is located in a seismically active area. For the purpose of this research, dead load and snow load will be considered for the analyses. Wind load was considered, but not included because the rise-to-span ratio of the dome is less than 0.20. For these shallow-type domes, the positive pressure zone on the windward face disappears [17].

a) Dead Load

The dead load of the dome is based upon the accumulated weight of the beams, cladding, connector hubs, and batten bars. Although the dead load accounts for over 67 tons of downward force imparted upon the supports, it does not significantly affect the performance of the dome. This was proven through running several linear static analyses via the **ANSYS** finite element program. **ANSYS** results showed that there are slight increases in stress levels throughout the structure, but the slotted supports serve as stress relief mechanisms, therefore minimizing the effect of the self-weight.

b) Snow Load

The amount of snow load is highly variable, depending upon the area of the country under consideration. For this study, the location which will serve as the "trial area" is the New York, New Jersey, Pennsylvania (tri-state) area. Following recommendations given in ANSI A58.1-82 for minimum design loads, a snow load equal to 25.2 lb/ft^2 will serve as the design snow load for this study [2].

STRUCTURAL WEIGHTS:
Struts: 78,213 lbs
Cladding: 31,645 lbs
Batten Bars: 20,270 lbs
Connector Hubs: 3,911 lbs

Approximate Dome Weight: 134000 lbs
Dead Load: 0.021 psi (~3 psf)

Surface Area: 45,000 sq. ft
Horizontal Projection: 40,000 sq. ft

LOADING PARAMETERS
Snow Weight Over Total Projected Area: 1,004,200 lbs

Snow Load: 25.2 psf

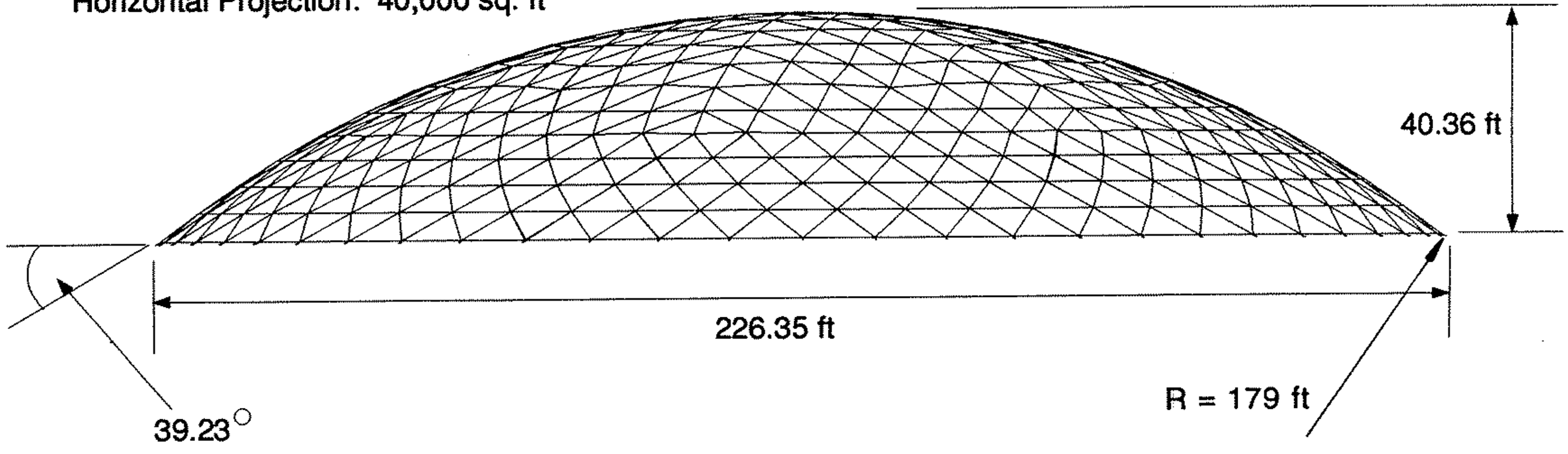

Figure 1.1: Dome Properties

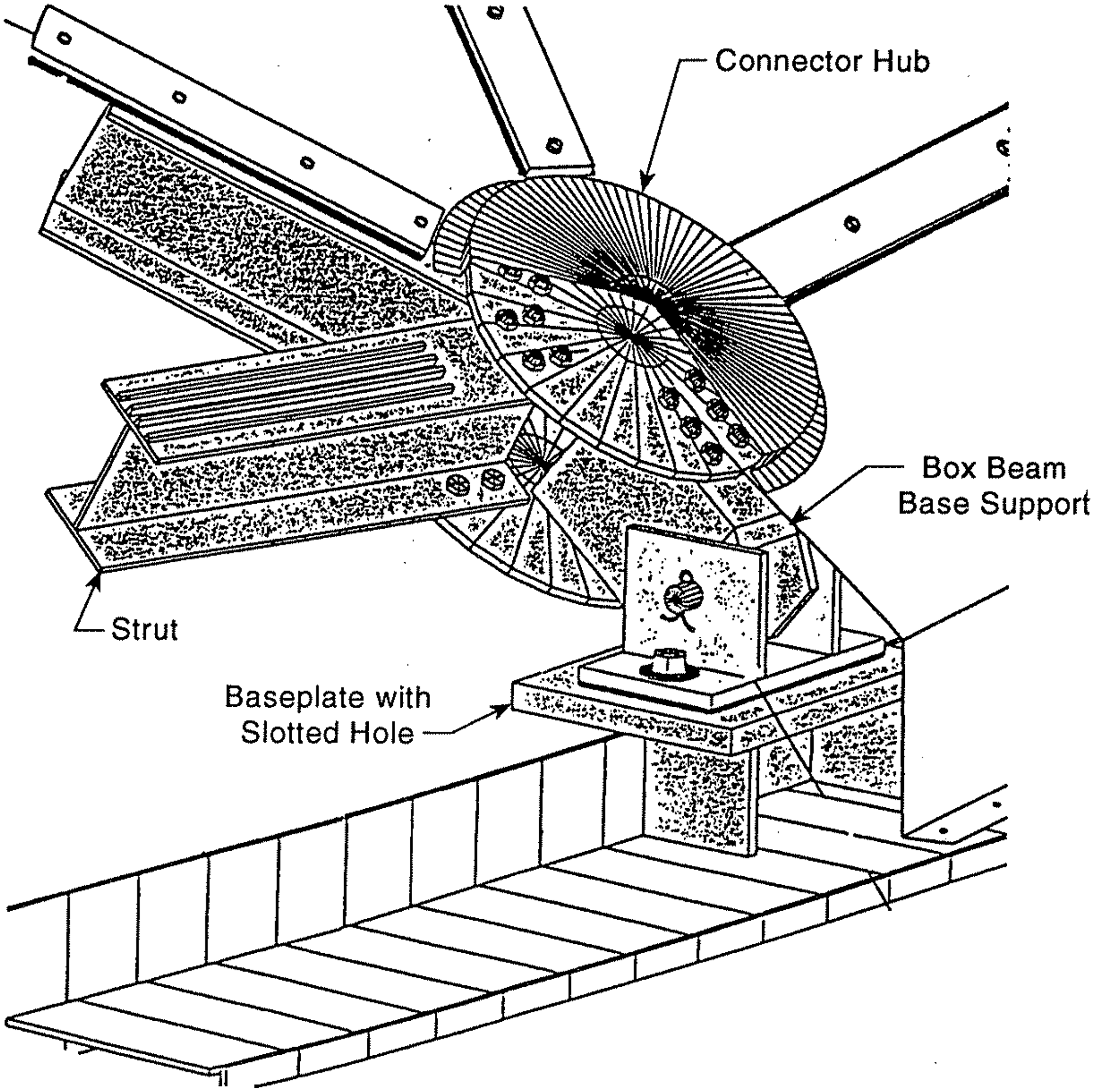

Figure 1.2: Support Detail

2. STATE-OF-THE-PRACTICE

2.1 FOCUS

Great strides have been made in the advancement of mathematical analysis procedures and computer solution techniques applicable to latticed structures. The focus of the problem which exists today is that the engineering advancements brought about by the development of complex domelike structures have brought about the need for equally complex design, analysis, and construction techniques. Numerous publications exist which cover these topics to a great extent [27]. The problem is that it is difficult for the design engineer to accumulate this knowledge on an overall basis because the information is so widespread. Bibliographies have been developed which serve to gather all pertinent information relative to the forementioned topics, yet the exercise of gathering the information and tediously searching through it still exists. In order to point the design engineer in the right direction, there must exist a convenient method by which one can reference a manageable amount of information, and at the same time, feel that a broad, yet accurate view of the procedure(s) has been obtained.

It is therefore the purpose of this section to summarize the current state-of-the-practice for the analysis, design, and construction of single layer aluminum latticed spherical domes. This particular phase of the study does not encompass detailed approaches to every known method nor does it serve as a design guide for the engineer to follow when designing these domes. Rather, it provides an overview of the more popular methods available today, so that a proper evaluation of a dome structure can be made.

As stated earlier, this particular state-of-the-practice report will address three important issues:

1. Mathematical model assessments
2. Finite element analysis applicability
3. Suitability of nonlinear solution techniques

Within the mid to late 1960's, structural engineers and researchers were trying to develop a continuum shell analogy expression applicable to reticulated structures. The Wright / Buchert critical pressure approximation presented in the last section was perhaps the most noteworthy effort of the sort. The search for more exact analytical expressions characterizing the behavior of reticulated structures was discontinued in the late 1960's and early 1970's due to the advent and availability of large digital computers and finite element software. At this point, it became most practical to model the components of the reticulated structures by finite elements. Thus, during the past two decades, there has been very little in the way of development, or improvement of the continuum shell analogy.

These issues (or shortcomings) are not unique to the dome problem, for they are paralleled in the development of almost any structure with a degree of complexity similar to that of a single layer geodesic dome. By focusing on these and related issues, the design engineer should come away with a better overall feel of what methods are available and best suited for the job at hand and also have an improved understanding of the critical buckling performance of these domes.

2.2 MATHEMATICAL MODEL ASSESSMENTS

2.2.1 BACKGROUND

The single layer geodesic dome, rightly classified as a spherical latticed structure, gives way to a special class of analytical solutions encompassing three-dimensional solution techniques which can accommodate a large number of structural elements and their corresponding stresses and displacements. Because the dome under consideration is a highly indeterminate structure, with the geometric complexity of the triangular configuration, a need for special analytical tools has arisen.

When analyzing large structures such as the single layer latticed spherical dome, the main area of concern which takes precedent is the identification and prediction of an accurate buckling load. Buckling of latticed domes falls into two categories: global buckling and buckling of a local nature [12, 28]. The difference between the two is that global buckling occurs when a relatively large area of the structure experiences an unstable condition, while the occurrence of local buckling stems from the failure of only one node as it snaps or deflects through. Local buckling takes precedent when only one node is affected, causing a localized reversal in adjacent member curvature. Since the domes being studied are exposed to a surface snow load, it was assumed the loading would lead to global buckling. Therefore, the concept of local buckling was not expanded upon, and the study concentrated on the global buckling phenomenon known as snap-through buckling [1].

2.2.2 CONTINUOUS MATHEMATICAL MODELS- GENERAL INSTABILITY

2.2.2A CONVENTIONAL SHELL THEORY

The concept of buckling of a latticed structure on a global level can be most closely compared to results obtained through buckling analysis using conventional shell theory. The overall quality of the solution is based on the absolute accuracy of the mathematical model which represents the true structure. When a latticed dome experiences a relatively large amount of distortion induced by a load applied normal to its surface, the structure experiences both membrane action and out-of-plane bending. By applying conventional shell theory, stability criteria are easily expressed through the use of shell buckling formulas. Most shell buckling formulas used in the context of dome analysis are based upon pressure loading, but since the domes being studied are shallow in nature, the pressure load acting normal to the surface closely represents the vertical orientation of the actual vertically oriented snow load. Thus the use of pressure expressions is satisfactory for the time being. The true problem with this application is that the use of a shell buckling formula is indicative of linear prebuckling behavior. Based upon finite element runs as seen in later sections of this study, load deflection observations of a geodesic dome prior to buckling shows that this prebuckling behavior is actually nonlinear to some extent. Thus, the critical buckling load as computed through conventional shell theory will actually be overestimated, resulting in a nonconservative design.

An additional point of interest is that shell behavior is sensitive to the effects of geometric imperfections and support conditions. Boundary conditions must be represented accurately in the mathematical model, otherwise considerable error will accumulate throughout the solution procedure. This is an important point, for many domes exist with their own specific boundary conditions. Take, for example, the dome which is being analyzed for this particular study. There are two different support configurations which exist for this dome, slotted and fixed. The critical response of the slotted structure will differ quite markedly from its fixed counterpart.

2.2.2B EQUIVALENT SHELL THEORY

In order to obtain a complete analysis of the latticed spherical dome, a more thorough breakdown of a dome into its basic structural components must take place. Thus, the next level of mathematical models pertain to the application of an "equivalent continuum" approach. Through this, the relationship between the latticed structure and the continuous shell structure is upheld mainly through the use the split rigidity method [28].

2.2.2C SPLIT RIGIDITY METHOD

The primary purpose of the split rigidity method is to provide a solution for determining the buckling pressure of a spherical shell-like structure through "discretization" of the shell into an equivalent set of effective membrane and bending parameters.

By the use of this method, an expression for the critical buckling pressure of an isotropic shell-like structure is obtained [7, 9]:

$$p_{crE}=CE(\frac{t_m}{R})^2(\frac{t_B}{t_m})^{3/2} \tag{2.1}$$

where

p_{crE} = critical pressure applied uniformly and normal to the shell
C = critical buckling coefficient
E = modulus of elasticity
R = spherical radius
t_m = effective membrane thickness
t_B = effective bending thickness

Numerous authors have derived this or similar expressions in order to study shell-like structures such as reticulated, orthotropic, sandwich, and stiffened shells. The main difference between expressions is found in a discrepancy of opinion in regarding the "correct value" [13] for the buckling coefficient, C, and arises through variations of derivations amongst the authors. For example, Buchert (1965) found that C = 0.366. Crawford and Schwartz (1965) used a differential-equation based derivation and determined that C = 1.16. Wright (1965) expanded upon the equation, and by applying additional continuous shell analogy, came upon the earlier relation (1.1),

$$P_{cr}=1.55\frac{AEr}{LR^2} \tag{2.2}$$

The use of the split rigidity concept has one main drawback. It is based upon the analysis of a "perfect" structure. An ideal geodesic dome is difficult to achieve, because fabrication tolerances will undoubtedly result in some accumulation of geometrical error upon construction of the surface. If this was to happen, the buckling equation stated above would be compromised. For example, if a deviation in the radius of curvature occurs at some area on the dome due to fabrication tolerances or problems encountered during assembly, an obvious change in the critical performance of the structure will materialize. Although equation 2.2 was developed taking into account a "delta factor" [6] for global imperfections, further investigation must be done in order to include a factor which addresses localized imperfections to a greater degree.

There are additional factors that must be considered when using shell analogy methods. Dome edge conditions must, once again, be considered. Poor edge conditions will result in buckling loads lower than those obtained through analytical means. Also, shell analogy is rooted in the fact that elastic action prevails during buckling.

Wright's expression of the critical buckling load serves as the basis for the reestablishment of a new set of critical buckling coefficients that can be applied to domes of a geodesic configuration similar to the one under consideration in this study.

As mentioned earlier, this phase of the study will appear in a forthcoming section.

2.2.3 DISCRETE MATHEMATICAL MODELS- GENERAL INSTABILITY

Discrete mathematical formulations for developing stability criteria of latticed structures are few. Whatever is available to the design engineer is based upon the formulation of a conventional stability analysis. Of these choices, two at the forefront of analysis methods are: (1) finite difference formulations and (2) matrix formulations [3].

2.2.3A FINITE DIFFERENCE ANALYSIS

When the use of partial differential equations with complicated boundary conditions is not feasible, the use of finite difference formulations would serve as a viable solution alternative. The basis of this method is the creation of a "grid" which completely defines the surface of the structure through the use of surface functions. The set of functions defines a set of finite difference equations which are used in calculations of surface displacements, forces, and/or other variables which describe the status of the structure under various loading conditions. The complexity of the difference equations is highly dependent upon the geometrical configuration, the coordinate system in which the system is defined, and the boundary conditions. Obviously, the three dimensional nature of the geodesic dome and its slotted supports only adds to the intricacy of the set of equations. Yet, the cyclic symmetry possessed by the dome allows for a more manageable manipulation of the solution technique. Although a two-dimensional example is the most recognizable form of the finite difference technique, three-dimensional grids which incorporate triangular and hexagonal patterns are also available. Therefore, the method lends itself usefully to the analysis of the triangulated latticed dome.

Due to the symmetric nature of the geodesic dome, the discrete method such as the finite difference method is an efficient means of solution. Since a large number of members and their affiliated difference equations are being dealt with simultaneously, analysis is facilitated by the use of a computer. A more thorough discussion of this method may be found in the text by Timoshenko and Goodier [29].

2.2.3B MATRIX FORMULATION

Matrix methods are perhaps the most fundamental methods of analyzing structures. They typify the term "discrete" because the structure must be broken down into an assemblage of individual members. Based upon this relatively simple description, it is quite easy to see why matrix formulation methods are ideal for latticed structures. Unlike a continuous shell structure, the latticed arrangement of a geodesic dome gives way to a structure which is already discretized, thus typifying the fundamental concept of a discrete mathematical method.

The stiffness method, or displacement method, allows for the analysis of structures with a latticed configuration such as the geodesic dome. The stiffness matrix is computed for each element and then constructed for the entire structure. Once the structural stiffness matrix is assembled, the resulting set of simultaneous equations can be solved for the unknown forces and displacements. For a dome of the size similar to or exceeding the one being considered in this study, the structural stiffness matrix has the potential to become unmanageable (>100 degrees-of-freedom). However, the cyclic symmetry exhibited in the geodesic dome gives the matrix certain repetitive characteristics. Since groups of data will be repeatable throughout the matrix, computer usage allows for convenient storage and processing of results in a manner which is both time efficient and accurate, depending upon the overall accuracy of the original mathematical model. Once again, it can not be stressed enough that the accuracy of the initial mathematical model is crucial for the correct interpretation of all solution data.

2.3 FINITE ELEMENT ANALYSIS APPLICABILITY

2.3.1 BACKGROUND

The finite element method of analysis is an extension of both the continuous shell theory and matrix approaches [5, 13]. The structure is represented as an assemblage of simple geometrical elements. These simplistic "shapes" are the "finite elements" which have their own established structural behaviors. The behavior of each different type of element, whether it is a beam, truss, shell, or any other structural form, is defined through a set of functions which describe a series of displacements unique to each element type. The assemblage of elements form a large-order system of linear algebraic equations. The solution to these equations result in a series of stresses, strains, and displacements of the system in response to the specified type and intensity of loading. The core of the finite element analysis routine is the choice of solution techniques used to solve the system of algebraic equations.

To solve for linear elastic stability, energy methods are used. The energy methods which are highlighted within finite element analysis techniques are based upon the principles of potential energy or virtual work.

A potential energy based formulation is developed in terms of strain energy. The strain energy, in turn, is expressed in terms of equivalent displacements. The resulting displacements expressions can be solved for and the results converted into a corresponding set of stresses and strains. The problem with potential energy methods is that only axial stresses are considered, which means that shear, torsion, and large deformation effects are not considered. If a large displacement solution is required of an energy method, then the concept of virtual work could be employed. There has not been much development within the area of virtual work relative to large displacement formulations, therefore this area will not be discussed any further.

Small displacement theory is valid when the need for prebuckling response of a system is desired. It will not suffice when systematic critical response is needed, such as the solution for buckling of a geodesic dome. When a loading state is needed to match or exceed the expected critical load of a system, one must resort to a large displacement analysis.

As far as small displacement theory is concerned, the most fundamental usage relative to stability analysis would be to determine the load level directly preceding any state of instability. The application of the bifurcation (eigenvalue) buckling approach is perhaps the most ideal small deflection approach for the purpose of performing a linear buckling analysis [5, 10].

2.3.2 BIFURCATION (EIGENVALUE) BUCKLING APPROACH

One of the ways a dome may lose its stability is via a sudden change of geometry which places the structure into an immediate state of unstable equilibrium. There is a point on the loading path where alternative states of equilibrium can exist. The three different modes of equilibrium which are physically possible are (1) stable equilibrium, (2) unstable equilibrium, and (3) neutral equilibrium. In order to understand the different stages of equilibrium, it is best to make reference to the example of the ball placed on a curved surface (Fig. 2.1). If a ball which is initially at rest is placed on a concave surface and a slight disturbing force is applied, the ball will eventually come to rest in its undisturbed location. This characteristic is indicative of stable equilibrium. On the other hand, if the ball is placed on a convex surface and disturbed slightly, the ball will eventually come to rest, but its resting place will never coincide with its original location. In this case, the ball is assumed to be in a phase of unstable equilibrium. Finally, if the ball is resting on a flat surface, the applied disturbance will move the ball to a new position. Once the force is removed, the ball will come to rest at that location. This action is representative of neutral equilibrium. With this concept of equilibrium in mind, the point at which a structure makes the transition from a state of either stable or neutral equilibrium to an unstable state of equilibrium is considered to be the point when stability is compromised, resulting in a loss of stiffness (structural failure). In terms of the method being considered, this stage is known as the point of bifurcation of equilibrium and the corresponding load is defined as the critical load.

Mathematically speaking, setting the determinant of the structural stiffness matrix equal to zero will result in a set of eigenvalues representative of the critical mode shapes of the system. The zero determinant indicates the loss of structural stiffness explained previously. This description is analogous to the linear algebra approach of determining the eigenvalues of a set of simultaneous equations. Hence, the approach is also known as the eigenvalue approach.

The main problem with this technique is that it is based on a classical elastic buckling analysis of a "perfect" structural system. Obviously, real-world structures are not ideal in that they exhibit varying degrees of geometric and or loading imperfections. Since eigenvalue analysis is based on the undeformed orientation of the structure, the results tend to be unconservative. Therefore, its use is not recommended for the design of actual structures.

2.3.3 NEWTON-RAPHSON TECHNIQUE

The need for a more accurate approach to predict the critical load response of a dome requires the implementation of a nonlinear solution technique. The nonlinear buckling analysis allows for the large displacement characteristics which are indicative of a large-scale structure experiencing stability problems. Since the structure is not maintaining its undeformed geometry throughout the loading phase, the mathematical expressions which define it must be updated to reflect the status of the structure. As for the dome, when it is being loaded in its nonlinear range, the overall structure is becoming softer (reduced stiffness). It is important to understand that a basic linear analysis would not predict the load displacement history of the curve because the classical linear elastic stress-strain relationship does not hold for nonlinear behavior. By assuming that the dome would respond in a truly linear elastic manner throughout its entire loading history would be a mistake.

Therefore, the use of a nonlinear analysis to predict the loading response of the geodesic dome is the proper approach. Looking at the different structural mechanisms within the dome gives reason why the structure is considered a nonlinear system. First, the slotted supports exemplify the idea of geometric nonlinearity. A change in configuration from a support that may or may not allow for radial movement depending upon its position in the slot necessitates a nonlinear solution technique. Material nonlinearity is found through the clothlike property of the cladding. Depending upon the deformation characteristics of the dome, the cladding can be either taut or slack. Since this cladding type does not maintain its original stiffness, the nonlinear analysis is once again supported.

The Newton-Raphson method is a nonlinear technique by which an iterative load displacement formulation is performed [4, 5, 17]. For example, if a load P_1 is applied to the structure, the corresponding displacement U_1 is subsequently found by forcing the solution to an equilibrium convergence point. This incremental load process is continued until the solution begins to diverge. At each load level, the overall equilibrium, as well as an updated stiffness matrix is computed. The difference between this technique and a standard linear analysis is mainly due to the idea that calculations are done on the deformed structure, rather than on the "zero load" structure. In essence, the Newton-Raphson method is nothing more than a series of small, incremental linear analyses pieced together to approximate a more realistic nonlinear behavior pattern of a structure (Fig 2.2).

As the structure's critical load is approached, convergence of the mathematical iterations slows. It is necessary to further discretize the load increments so that the proper value of critical load is found. Upon obtaining a critical value of load, the mathematical expressions will not allow for any further iterations. This is because the determinant of the structure's stiffness matrix equals zero, resulting in numerical instability of the solution. To avoid this problem, a switch should be made from an incremental load control approach to displacement control. Unfortunately, the Newton-Raphson method does not support the option of displacement control solution technique, as does the Riks-Wempner method, which will be discussed in the next section. When using the Newton-Raphson method, the critical load of the dome is indicated by a sudden increase in the magnitude of selected nodal displacements, with respect to previous values. The changeover to displacement control allows for the tracking of post-buckled behavior, such as the snap-through action of domes. This change in loading control parameters is depicted in Figure 2.3.

There also exists a Modified Newton-Raphson approach where the only difference from its former is that the stiffness matrix used in each iteration is not updated at each load step. This results in a savings of time used to reformulate the matrix, but an increased number of iterations are required to produce the same quality as a full Newton-Raphson approach.

2.3.4 RIKS-WEMPNER TECHNIQUE

The Newton-Raphson technique is relatively efficient in the early stages of a structural analysis. As the solution approaches the critical point, the method will have much difficulty finding a point of convergence, which would represent buckling of the dome. The impending singularity of the stiffness matrix requires an increased number of load steps and equilibrium iterations in order to achieve convergence. Eventually, the solution will diverge completely. At this point it is necessary to explore an alternative route in order to track the loading history in the region of, and beyond the critical region. The Riks-Wempner, or "constant arclength" method provides such an alternative to this problem [14, 19].

Whereas the Newton-Raphson formulation is primarily a load-controlled solution technique, the Riks-Wempner method allows for a displacement-controlled approach to defining the overall structural performance throughout the entire loading history, and not just within the critical region. The main difference between the Newton-Raphson and Riks method is that the Riks formulation employs a solution technique where the loading and displacement values for a particular step do not remain constant. An arc-length to the tangent stiffness matrix at a prescribed point on the load deflection curve is defined, and the iteration cycles follow a path designated by a "sphere" (Fig. 2.4) with its origin located at the prior load step and radius, r, where incremental load and displacement values have been previously determined.

This iterative technique has been proven very accurate, and has given good results for structural problems which necessitate the use of a method to establish a post-critical loading history. Finite element packages such as **ABAQUS** use this method with much success, due to its computational efficiency and reduced data storage requirements [14].

2.4 NONLINEAR SOLUTION FEASIBILITY

It is quite appropriate for large-scale structures to exhibit some form of "imperfection". Whether the imperfection is found to be material-based or geometrically related, the structure is absolutely not an idealized form. In order to properly address these shortcomings, nonlinear analysis is highly recommended. Nonlinear solution techniques are most efficient when used in tandem with computer packages. The three most prominent finite element packages which incorporate the nonlinear solution option are **ANSYS**, **ADINA**, and **ABAQUS**. Each individual package has its own pros and cons. **ANSYS** is probably the most user friendly program of the three, and it makes use of Newton-Raphson solution algorithm to solve for prebuckling behavior. **ABAQUS** takes over from where **ANSYS** leaves off by incorporating a displacement controlled algorithm, namely the Riks method, to interpret the postbuckling behavior of the structure. Although **ABAQUS** does a more thorough job of interpreting the load displacement history of a structure, the earlier version of the package itself is not as "graphical" as **ANSYS**, thus the user cannot get a visual perspective of the analysis. **ADINA** is probably the most in-depth nonlinear mathematically based package of all, yet the use of the program tends itself toward noninteractive (batch) usage. Preprocessing graphical options are relatively nonexistent within **ADINA**.

Obviously, the biggest is not always the best. If the design engineer is analyzing a shallow single-layer dome, a modest nonlinear approach should be used. A limit should be placed on the complexity of the package used, yet the software should allow for a high level of maneuverability amongst linear and nonlinear solution techniques. Since a shallow single-layer dome is prone to large displacement response, linear analysis may be used to "get a feel" for the overall response of the structure prior to its critical state, but not for an accurate prediction of the critical load itself. If a linear solution technique such as a bifurcation algorithm is used to predict critical response of a highly nonlinear system such as a shallow dome, the results will be nonconservative (Fig. 2.5). A nonlinear analysis will provide the design engineer with a more conservative and much safer design criteria.

2.5 LINEAR VS NONLINEAR FINITE ELEMENT ANALYSIS

Due to the computational demands imposed by the nonlinear analyses of multi degree-of-freedom structures, it is not feasible to use nonlinear finite element analysis as a "preliminary design tool". Nonlinear analysis solution methods vary from package to package. Therefore, the analysis of an identical structure by different nonlinear computational approaches will probably result in solutions which can differ by rather large percentages. However, linear elastic theory will yield exact results, regardless of the solution technique used. As a result, linear elastic finite element analysis is considered to be a good approach to check the structural design. In conjunction with a postprocessor, the safety margins of each member can be checked. These design checks are absurd if they are to be done manually. However, as the Load and Resistance Factor Design (LRFD) method for design becomes predominant within the aluminum industry, the efficient use of a postprocessor will enable critiques of multiple load cases to become realistic for both linear and nonlinear analyses.

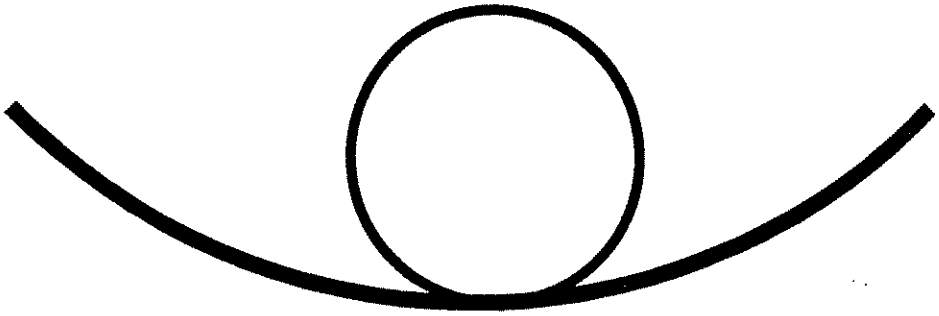

1. STABLE EQUILIBRIUM

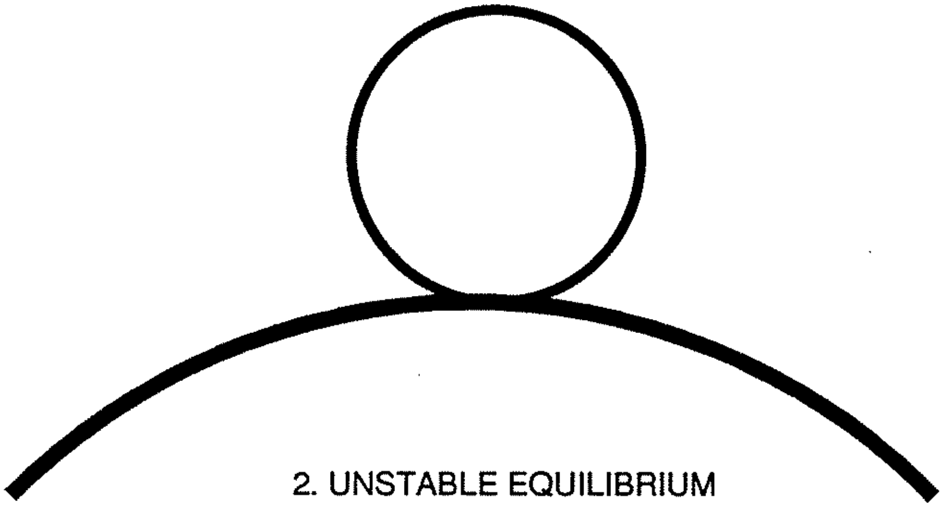

2. UNSTABLE EQUILIBRIUM

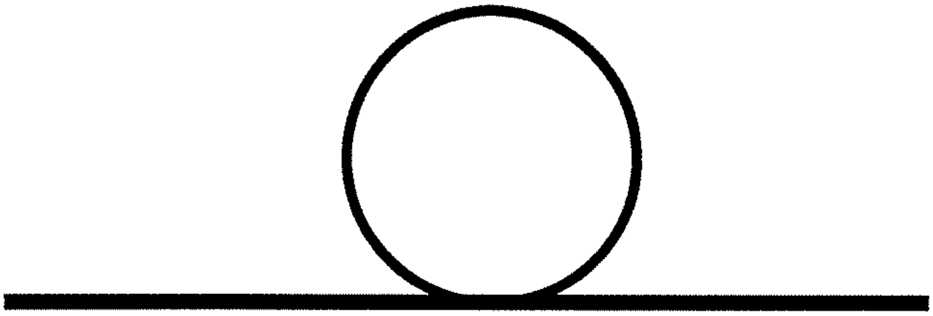

3. NEUTRAL EQUILIBRIUM

Figure 2.1: Three Modes of Equilibrium

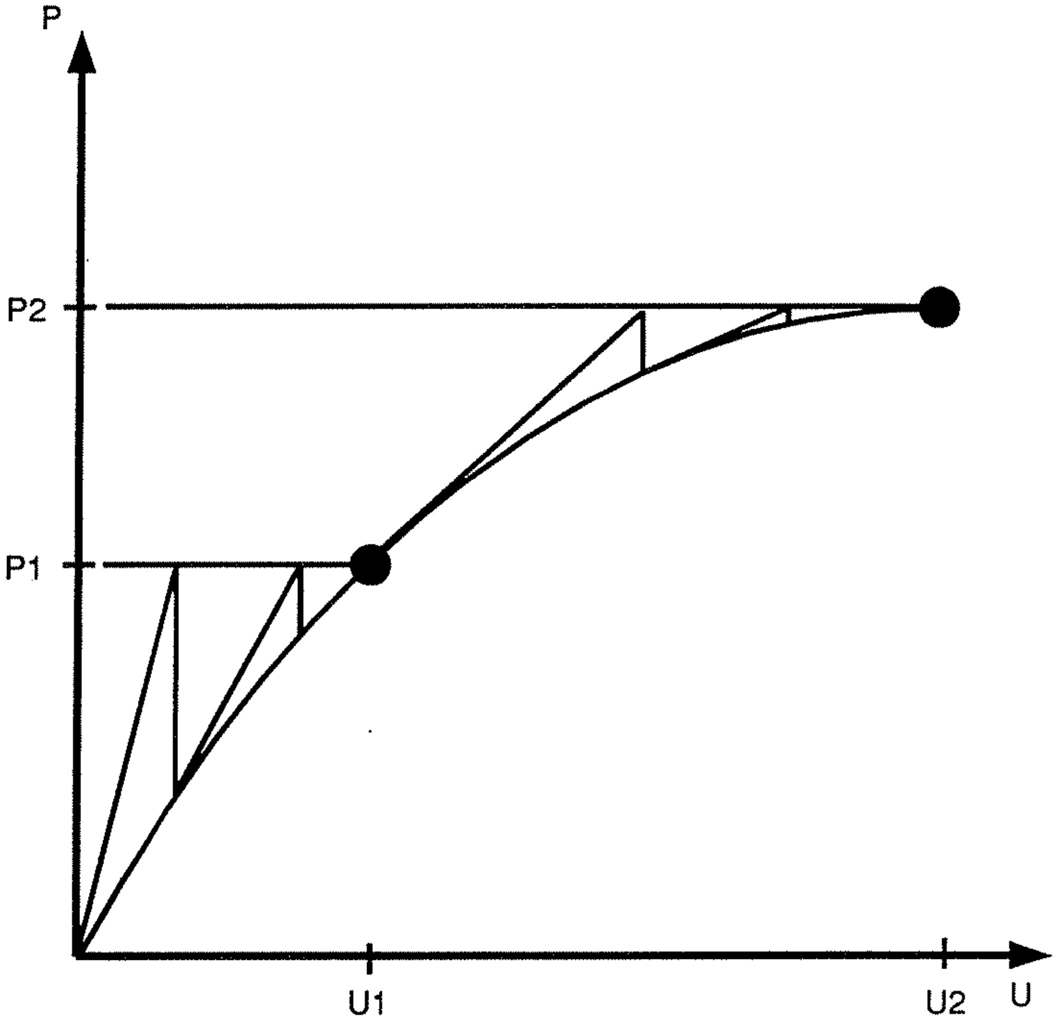

Figure 2.2: Newton-Raphson Iterative Solution

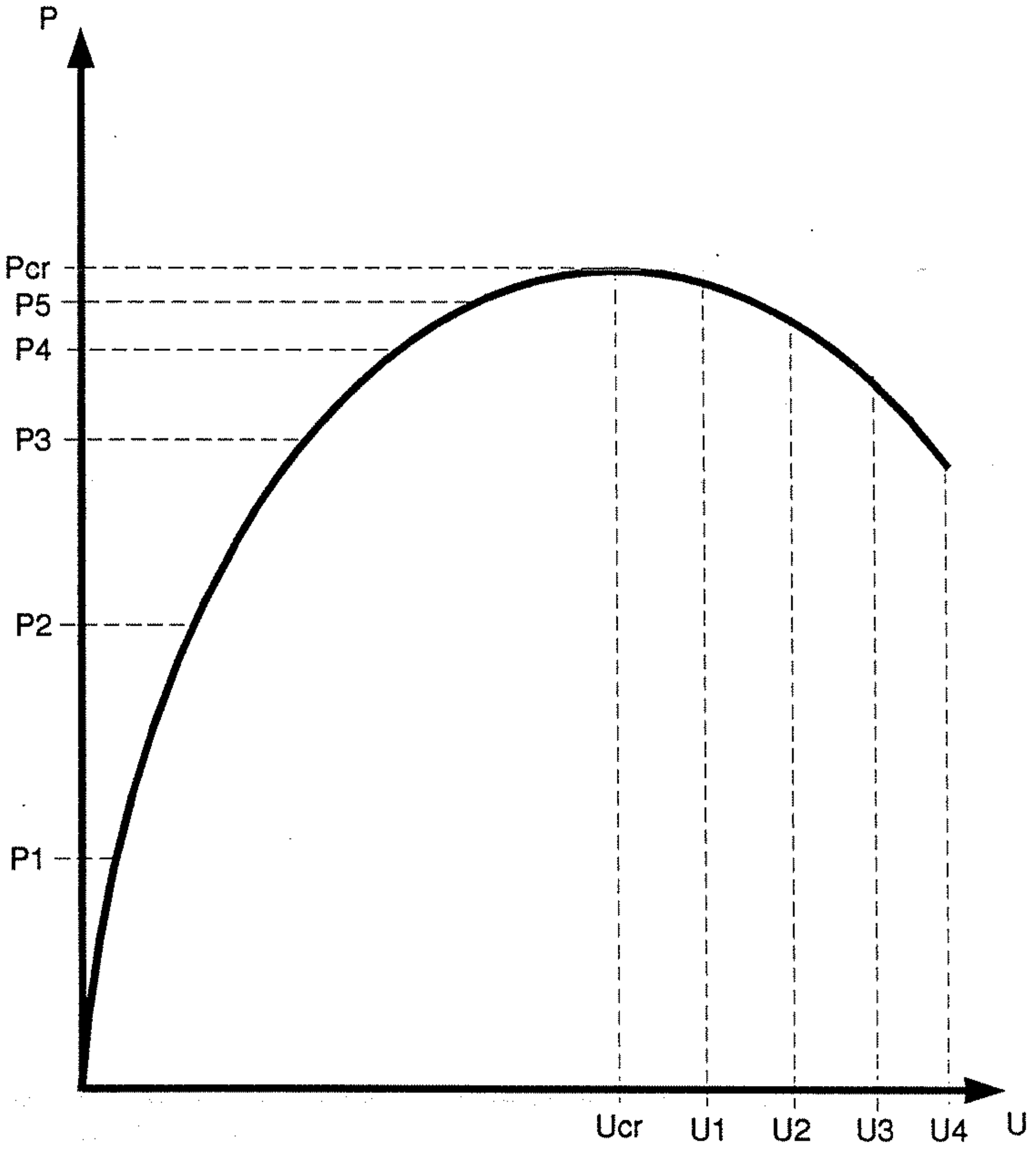

Figure 2.3: Transition From Load Control to Displacement Control

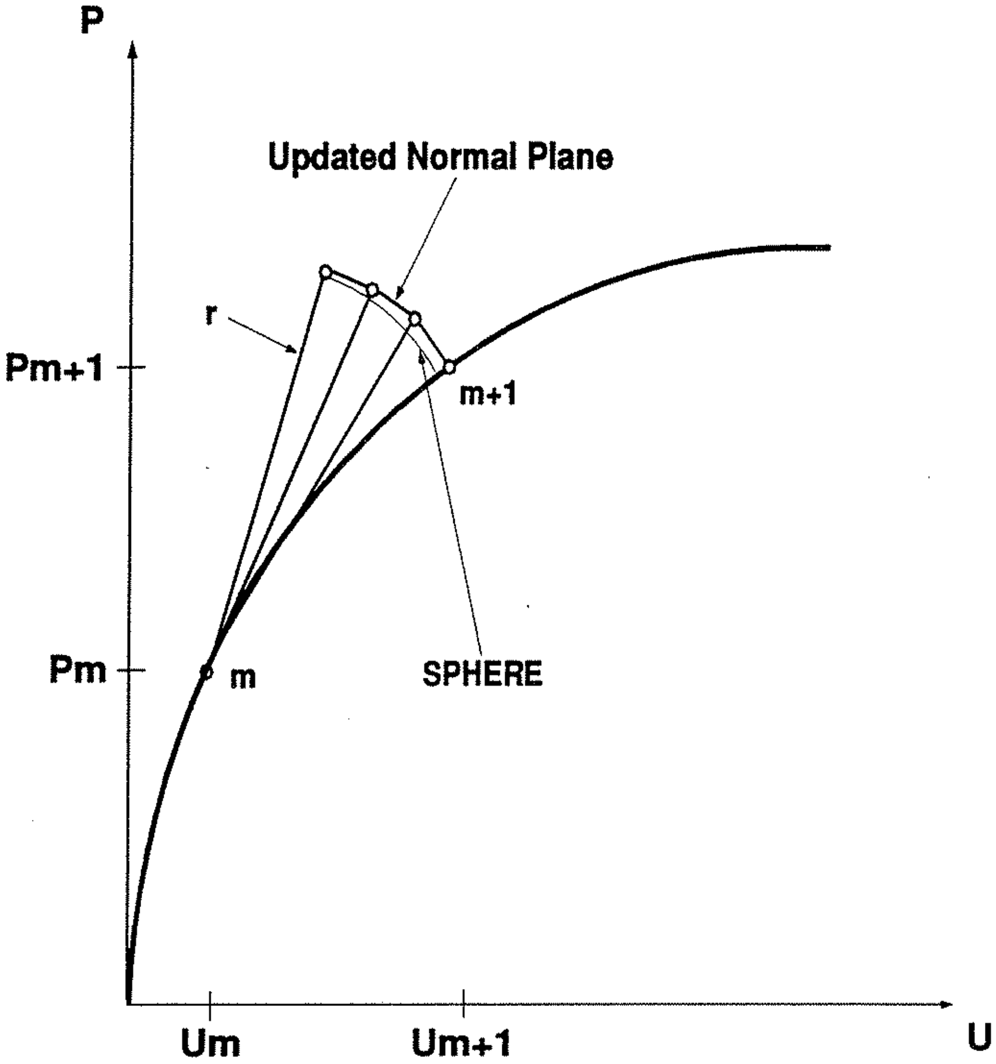

Figure 2.4: Riks - Wempner Formulation

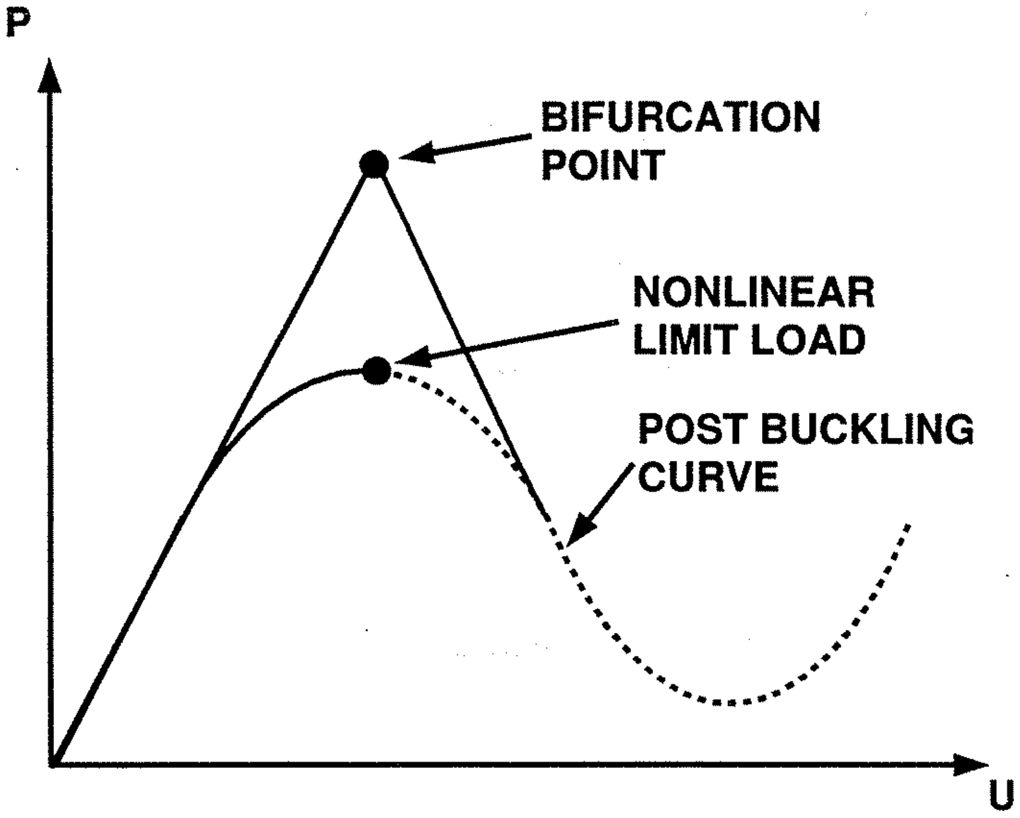

Figure 2.5: Linear vs Nonlinear Analysis

3. FINITE ELEMENT ANALYSIS CASE STUDY

3.1 BACKGROUND

There are many different facets of the design to consider in the analysis of an aluminum geodesic dome. Consider two of the many factors which need to be accounted for when creating an accurate dome model. Proper boundary conditions will undoubtedly influence the outcome of the solution, just as will the decision about what types of elements should be used to model the structure. For this particular case study, the **ANSYS** (versions 4.4A and 5.0A) finite element analysis program was used to perform the needed analyses. **ANSYS**, introduced by John Swanson and Swanson Analysis Systems, Incorporated (1970), is a general-purpose finite element program which can be used in all disciplines of engineering. Its superior graphical capabilities, coupled with the ability to perform nonlinear buckling analyses made it a prime candidate for the geodesic dome analysis. The only drawback to the program, which was previously mentioned, is that the nonlinear solution technique being used does not allow for any post-buckling analysis. Since the dome is assumed to be considered failed at its peak load, this information is not necessary for this phase of the research. The important information corresponds to the critical loading region for which the solution is valid.

3.2 ORIENTATION

In order to properly interpret the forthcoming solution results, it is necessary to "orient" the reader with the terminology and graphical displays:

a) Terminology

1) Spar- Beam element used within the framework of the dome.
2) Cladding- Thin sheeting which covers the dome.
3) Bare Frame- A dome without cladding in place.
4) Slotted Support- Mounting fixture at base of dome allowing radial expansion.
5) Hub- Joint used to join members at a common point.
6) Time Step- Increment of time which corresponds to a load substep.
7) Full Snow Load- Loading applied over the entire dome surface.
8) Half Snow Load- Loading applied to 1/2 of the dome surface.

b) Graphical Displays

In order to clarify the orientation of the visual displays associated with this case study, the following orientation has been imposed. All plots of the dome, whether they are plan, elevation, or isometric views, are placed in a landscape-type configuration and will have the east face of the dome to the right of the page and west face to the left. The south face of the dome will face the reader in elevation views, be at the bottom of the page in plan views, and face the reader for isometric views (Fig. 3.0). For the two loading cases, the full snow load is applied over the entire dome, and the half snow load is applied to the east face of the dome (Fig. 3.1).

There are a limited number of terms which are associated with the explanation of results that should be explained. With reference to Figure 3.2, they are:

a) *Tension Ring*- The lowest horizontal ring in the dome.
b) *Seam / Meridian Members*- The "spokes" which separate the dome into segments.
c) *Transition Segment / Layer*- Members located directly below spokes (segment) and continue around the circumference of the dome (layer).
d) *Interslice Region*- Members located between the meridian members.
e) *North-South Meridian Line*- The line which essentially divides the dome into eastern and western segments.

3.3 MODELING INFORMATION

3.3.1 NODES

Preliminary information on nodal coordinates was obtained through Conservatek. These coordinates represented a 1/14 segment of the dome which were mirrored about an outer edge of nodes in order to produce a symmetric "pie slice" of accurate nodal locations. The slice represented 1/7 of the hub locations. By rotating the slice through seven increments of 51.43°, the full spherical pattern of the geodesic dome was generated (Fig. 3.3).

3.3.2 SPARS

In order to "install" the spars, the original 1/14 segment of nodes was used, and a user-interactive technique of picking nodes with a mouse aided in the generation of the spars associated with the segment. Then, by using symmetry modelling techniques, similar to those used to generate the nodes, the complete spar assemblage was formulated (Fig. 3.3). The proper spatial orientation of the spars was maintained through the use of a third node. The plane formed by the third node and the nodes defining the end of the spar lies parallel to the web of the spar. Therefore, if the center of the sphere which defines the spherical shape of the dome is designated as the third node for every spar, the web of each spar will orient itself in line with the center of the sphere.

3.3.3 CLADDING

When it was necessary to place cladding on the dome, the technique used for spar generation was applied to shell elements, rather than to beam elements (Fig. 3.4). Three predetermined nodal locations defined each section of triangular cladding on the model.

3.3.4 BASE SUPPORT

The support mechanism was modeled using a combination of beam elements and gap elements (Fig. 3.5). The base of the dome is connected to the support mechanism through a box beam section which is rigidly connected to the dome and pin-connected to the mounting bracket (Fig. 1.2). The mounting bracket has the capability to move radially due to a slotted hole in the baseplate. The slot is simulated through the use of a gap element attached to the end of the box beam. The gap element is given an initial "open" status of 3 inches, which allows the dome to slide radially outward at its supports for 3 inches. After 3 inches of axial movement, the gap element exhibits an extremely high stiffness, which essentially means that the dome is bearing upon the end of the slot. At this point, the support continues to perform as a pinned mechanism.

3.3.5 SPAR LATERAL CONSTRAINT

Due to the moment restraint condition which exists between beam elements, the connector hubs are assumed to exhibit full fixity. Additionally, the in-plane rotation of the hubs are restrained, thus restricting lateral deformation (weak axis bending) of all beam elements and inhibiting lateral local buckling via the restraint of in-plane nodal rotation. Since the cladding cannot be modeled as being attached to the spar flanges at intermediate locations, the prevention of in-plane nodal rotation is a substitute method to simulate the effect that the cladding would have in limiting minor axis bending of the spars.

3.3.6 MODEL OPTIMIZATION

Due to the symmetric nature of the structure and the repetitive manner in which the dome model was created, there existed many coincident nodes and elements at overlap regions between adjacent pie slices. In order to resolve this problem, all coincident nodes and elements were merged into single entities. Once merging was completed, all remaining nodes and elements were compressed and reordered to save data storage space, and ultimately reduce the maximum wavefront size (and computation time) at the start of a solution routine.

3.3.7 GEOMETRIC/MATERIAL INFORMATION

In order to anticipate the need for elements which exhibit both geometric and material nonlinearity, a decision was made to incorporate elements into the model which allowed for this expected behavior.

The beam element which most closely meets this criterion is an elastic-plastic three-dimensional beam element with tension-compression, bending, and torsional capabilities. By having a user-defined cross section, the characteristic "I" shape of the section was able to be modeled. This beam type has large-deflection capabilities, suitable for nonlinear analyses.

The cladding is simulated through the use of a thin shell element. This element type is well suited to model nonlinear and thin shell-like structures. Its large-deflection capability is important when performing the necessary nonlinear buckling analysis.

As far as material properties are concerned, both beam and shell elements exhibit material nonlinearity capabilities. Therefore, material behavior of both element types was defined through the input of a particular stress-strain curve and other specifications obtained from the Aluminum Construction Manual [26]. The beam elements, which consist of series 6061 aluminum alloy, are modeled with a bilinear stress-strain curve having a yield point of 40 ksi and a strain hardening modulus of 43 ksi. The cladding is composed of series 3003 aluminum alloy and modeled with a bilinear stress-strain curve defined by a yield point of 25 ksi and a strain hardening modulus of 21 ksi. For both element types, the model incorporated values of 0.098 lb/in^3 for density, 13.1E-6 in/in/°F for a coefficient of thermal expansion, a shear modulus of 3,800 ksi, and an elastic modulus of 10,100 ksi.

3.4 LOADING INFORMATION

As mentioned in section 1.3.2, the low rise-to-span ratio of the dome classifies the structure as a shallow dome. For such a dome in the northeast, the region representative of the snow load chosen for the analysis, there is not a typical positive wind loading condition that significantly increases the cumulative effect of dead load plus snow load. There can be a significant negative (or suction) wind loading condition, but it decreases the cumulative effect. Therefore, wind loading was omitted in the analyses.

The snow load was simulated by applying a gravitational force upon the structure. The equivalent service snow load magnitude was calculated by applying a magnification factor, MF, to the acceleration constant to result in an equivalent downward force of 25.2 lb/ft^2. The magnification factor is given by Eq. 3.1, with the snow load on the surface of the dome equal to 1,004,200 lbs:

$$MF = \frac{DEAD\ LOAD + SNOW\ LOAD}{DEAD\ LOAD} \tag{3.1}$$

The magnification factor for this particular loading configuration is approximately 8.5, which means that 8.5g is representative of the service snow load of 25.2 lb/ft^2. This relationship is acceptable only when a weight density (lb/in^3) is input into the model.

3.5 SOLUTION EVALUATION INFORMATION

For this case study, a Newton-Raphson nonlinear solution technique was used [4]. Since the weight density/unity gravitational acceleration constant relationship was used for this solution procedure, loading was simplified. A preliminary "guess" of the buckling load is made, and that guess is used for the applied gravitational load. If the buckling load is underestimated, the solution will continue to converge. Thus, an iterative technique is employed to "zero in" on a close estimate of the critical load. Ultimately, a semi-exact guess will be made, and the solution will diverge. This divergence represents the critical state of the dome. Once an accurate prediction is made for the critical load, subsequent solution runs for additional load cases will proceed in an efficient manner. An automatic time stepping (load incrementation) option is used to let the program determine how many time steps to use within each load step. The number of time steps is automatically increased or decreased, depending on the ease at which the solution is converging. If the solution is converging easily, the size of the time step will be automatically increased for the following load step. On the other hand, if the solution is having difficulty converging, as it does as buckling approaches, then the subsequent time steps will be reduced, resulting in improved convergence parameters. If the equilibrium iterations fail to converge, (i.e. the difference between the restoring forces and applied loads is not within a specified tolerance limit), the current time step is divided and the analysis for the reduced time step is performed until convergence is achieved. This procedure continues until the full load has been applies and equilibrium has been satisfied. The TIME option of **ANSYS** specifies time at the end of a load step. Since this a rate-independent analysis, TIME is used merely as a tracking parameter. With this in mind, a convenient one-to-one correspondence between time and gravitational acceleration is made so that output results at a certain load level can be traced with respect to its corresponding solution time. In other words, one time unit equals a unit increment of additional load (Time History Postprocessing = Load History Postprocessing).

3.6 LOAD CASES

Four independent configurations were analyzed for this study:

Run Case 1: DSNLB

This configuration incorporates the nonlinear buckling analysis for a bare frame dome subjected to full snow load.

Run Case 2: DSNLCB

This analysis is identical to case 1, but the dome is cladded.

Run Case 3: DHSNLB

This case run is a nonlinear buckling analysis for a bare frame dome subjected to half snow load.

Run Case 4: DHSNLCB

This case is identical to case 3, but is for a cladded dome.

All four runs incorporate domes resting on the slotted supports. Fixed support configurations were not analyzed.

3.7 FINITE ELEMENT MODEL (FEM) RESULTS

3.7.1 DSNLB RESULTS (full snow / bare frame)

a) Service Load

The first phase of the analysis was used to ascertain service load results for a nonlinear static analysis. The load at which the dome was analyzed for this case was 1,055,800 lbs (26.5 psf), evenly distributed amongst all supports. This was slightly less than the snow load and dead load sum, due to the nodal distribution of load resulting in the analysis.

Nodal deflections ranged from 1.41 to 2.83 inches. The crown of the dome deflected downward 2.2 inches while the slot movement was found to be 1.41 inches in the radial direction. As shown in Figures 3.6 and 3.7, the maximum nodal deflections occurred on the meridian seams in the area directly above the transition region. Large displacements also occurred in the upper quadrant of the domes. Smaller nodal displacements in the 1 to 2 inch range were found in the lower interslice region of the dome. The radial slot displacements were within 0.02 inch of each other, indicative of symmetric loading of a cyclically symmetric structure.

Nodal rotations were examined in order to check the degree of in-plane bending. Existence of in-plane bending of the dome would mean that lateral (weak axis) bending of the struts was occurring. In reality, this lateral deflection is prevented by the cladding. Computed in-plane rotational values were negligible, which means that the crude method of simulating the cladding through restricting nodal surface rotation is valid. As for out-of-plane rotations, the largest movement was observed at the tension ring nodes (2.005°).

Axial stresses are important in that they indicate the path through which the forces "flow" through the structure and into the supports. A maximum tensile axial stress of 9,055 psi was encountered within the tension ring at the bottom of the structure. Compressive axial stress distribution (Figs. 3.8 and 3.9) indicates that the compressive stresses range from the maximum, found in the top rings of the dome (~ 4,100 psi) to a minimum within the ring above the tension ring (~ 100 psi). Intermediate values of compressive axial stresses dominated at the meridian seams and the lower diagonals (~ 4,000 psi), and gradually decreased through the transition members and interslice members (2,500psi ~ 3,500 psi) and finally through the diagonals emanating from the meridian seams (< 2,500 psi). It appears that the forces followed the meridian direction into the lower compressive diagonal members.

In order to foresee the shape into which the dome will eventually buckle, it was important to examine the major axis bending moments and transverse shear loads of all beam elements. The largest member bending moments (although relatively small) were found in the lower region of the dome. The members framing into the tension ring experienced the highest bending moments and shearing forces, while the lowest moments and shears were located in the transition layer and regions toward the top.

The result of the forementioned nodal deflections, axial stresses and other performance properties of the structure was the deflected shape of the dome due to service load conditions. It appeared that the bottom layer of the structure exhibited a compromised state of stability, and the consequence of such a weakness resulted in a folding, or curling of the dome at its base (Fig. 3.10).

b) Critical Load

The uncladded dome was loaded past its service load level and a numerical instability corresponding to global buckling was achieved. The load at which this occurred was 49.1 psf, which equates to a total snow load of nearly 2,000,000 lbs.

Nodal deflections ranged between 2.58 and 6.18 inches. The top of the geodesic dome was found to have deflected down 4.62 inches, while the base of the dome slid radially outward 2.98 inches. The 3 inch slotted support plate had no effect upon the analysis, since the members framing into the support never beared upon the edge of the slot, even up to the point of collapse. As seen in Figures 3.11 & 3.12, maximum nodal deflections were observed on the meridian seams (5.7" ~ 6.1"), while the smallest movement was located in the tension ring nodes. The slot deflection values were within 0.03 inch of each other about the entire circumference of the dome, indicating that the dome still maintained a symmetric geometry upon buckling.

Nodal rotation indicated nearly 5° of out-of-plane rotation had taken place within all tension ring nodes, and the remainder of the structure had experienced virtually no rotation. The "softening" of the base of the dome, discussed briefly in the last section, has apparently been the governing factor in the propagation of failure of the structure. Before the discussion of the failure mode proceeds further, member performance characteristics must be examined.

Axial stresses are important in determining the mode of failure of this geodesic dome. Yielding of members was critical in the failure analysis, because if this was to occur, the member essentially becomes ineffective, thus providing for a "weak link" in the lattice from which a more localized failure can propagate. The maximum axial stress for the entire structure was tensile (19,100 psi), and was found in the base tension ring. Observing the difference in axial stresses amongst all tensile ring members, a variation of 100 psi was found within those members. Essentially, the stresses are the same, thus reinforcing the concept of symmetrical performance of the dome, in terms of its loading and deformation. Compressive stresses (Figs. 3.13 & 3.14) were found to be greatest in the third horizontal ring from the bottom of the dome (~ 8,700 psi). The 8,000psi ~ 8,500psi compressive stress range was found throughout the second set of lower diagonals and the upper third of the dome. The meridian members and the immediate surrounding members experienced compressive stresses approaching 7,500 psi. The base diagonal members, diagonal members extending from below the seams, and transition segment members had compressive stresses ranging from 5,000 to ~ 7,000 psi. Compressive stresses of 3,000 psi and smaller were found in the horizontal ring immediately above the tension ring. Just as in the service load case, the stresses seem to have followed a path through the meridian members into the lower horizontal compression ring. The main difference between the two cases is that there was a larger overall accumulation of stresses at the seams in the critical load case, whereas in the service load condition, the dome possessed larger relative compressive stresses within the interior of each pie slice.

Much greater values of beam bending moments and end shears with respect to the remainder of the dome indicate that the source of instability emanated from the base region of the dome. A tremendous amount of bending and shearing was transmitted through the hubs connecting the tension members, mounting beam elements, and lower diagonals. Much lower values were distributed throughout the transition elements and members in the top half of the dome.

The result of increasing the applied load to a level of 49.1 psf was impending collapse of the upper ⅔ of the dome upon its base. The transition segment of the dome acted as a restraint mechanism for the upper section of the dome, and allowed for the forces to be transmitted into the lower region of the dome where the buckling action commenced (Fig. 3.15).

3.7.2 DSNLCB RESULTS (full snow / cladded)

a) Service Load

Nodal deflections for the cladded dome at the same service load (26.5 psf) ranged from 1.15 to 2.10 inches when exposed to the same service loading conditions as the DSNLB case. The crown of the dome deflected downward 2.01 inches, and all the slotted supports moved outward a distance between 1.31 - 1.32 inches, once again reinforcing the symmetric distortion displayed throughout the dome. Just as in the bare frame case, Figures 3.16 and 3.17 show the maximum relative nodal displacements occurred at the nodes directly below the transition layer of the dome, and the top ⅓ of the dome underwent similarly large displacements.

Nodal rotation distributions were similar to the bare frame dome, with the larger out-of-plane rotations occurring at the tension ring nodes (1.8°), and with minimal rotations in the transition region (0.001°).

The largest axial tensile stresses, 8470 psi, in the cladded model occurred in the tension ring. The members with the largest compressive stresses (Figs. 3.18 and 3.19) were the spars located in the ring two levels above the tension ring (1,678 psi), while the smallest compressive stresses were in the ring directly above the tension ring. Intermediate compression members were the seams and interslice regions (~ 1,000 psi), seam diagonals and transition rings (500 psi ~ 1,000 psi). Minimal compression was found in the lower diagonals. Comparisons of the bare frame and cladded models indicate quite similar distribution of stresses. A majority of the stresses flow through the seams directly into the lower segments of the structure. The interslice regions were seemingly moderately stressed at service load levels.

Once again, the point of instability stemmed from the lower sections of the dome. The lower diagonals experienced the greatest bending moments and shearing forces, and their corresponding connector hubs were subjected to large moments and shearing forces. The lowest bending moments and shearing forces were centered at the midheight of the dome.

It appears that the addition of the cladding did not change the overall performance of the dome during loading within its service range. Nor did it markedly change the stress distribution pattern from that of the bare frame case. The biggest difference between the bare frame and cladded models appears in the difference in axial stresses. The cladding acts in a manner of in-plane restraint in that it relieved both the spar tensile and compressive stresses by capturing in-plane stresses via membrane action. The maximum skin stresses (~ 7,150 psi) displayed in Figure 3.20 appeared to be concentrated within the lowest two rings of the dome. These stresses were quite localized and quickly attenuated in the higher areas of the dome.

The resulting displaced shape is similar to the bare frame model, resembling the form of a "sombrero hat" (Fig. 3.21).

b) Critical Load

The cladded dome was loaded beyond its service level until the numerical instability indicative of buckling occurred. The critical load for this particular case was 17.23g, which equates to a snow load of 54.5 psf. The resulting nodal deflections ranged from 2.62 to 5.06 inches. Crown deflection was 4.63 inches and the slot movement was radially symmetric at 2.99 inches. The nodal displacement contour plot of Figure 3.22 highlights the maximum displacements within the layer below the transition region. The top ⅔ of the dome also experienced relatively large displacements of approximately 4.5 to 4.7 inches. Aside from the slot measurements, the region with the smallest displacement was apparently the transition layer (4.2 inches).

Nodal rotations indicated that the larger rotations (4.4°) took place at the lower connector hubs, while the smaller rotational values were reflected in the out-of-plane movement of the nodes associated with the seams above the transition region (0.004°).

Axial stresses in the spars (Figs 3.23 - 3.24) were maximum tension in the base ring (19,230 psi) and maximum compression in the third ring from the base and the diagonals directly below it. Compressive stresses were most prevalent in the seams of the dome and the interslice regions (~ 3,000 psi). The compression in areas closer to base of the dome are gradually reduced, with stresses reaching negligible values in the lower diagonals and the transition region (~ 2,000 psi).

Beam bending moments and end shears are dominant within the layers below the transition regions and minimal within the transition region and higher areas of the dome.

Skin stresses (Fig. 3.25) were greatest in the lowest layer of the dome (16,230 psi), yet they were quite below the yield stress of the material. The associated bending moments are worth taking note of, because they also show that the larger values occurred in the lower layer of the cladding, indicating that this dome configuration is susceptible to an instability near the base.

The slot displacement of 2.99 inches mentioned earlier still does not reach the outer limit of the hole, thus the edge conditions remain the same throughout both bare frame and cladded cases. The full snow load of 54.5 psf precipitates failure in the mode depicted in Fig. 3.26, wherein the critical deflected shape is symmetric in nature and has buckled in upon itself.

3.7.3 DHSNLB RESULTS (half snow / bare frame)

This case and the following case are identical to the previous two cases with exception to loading patterns. The half snow load cases, as mentioned earlier, were analyzed with respect to snow load existing on the eastern half of the dome surface. By altering the loading patterns, various interesting comparisons can be made among all load cases.

a) Service Load

For the service load on the bare-frame aluminum geodesic dome subjected to half snow load, a snow weight of 512,250 pounds (25.7 psf) was applied on half the surface. This loading condition resulted in a deformation pattern representative of that seen in Figure 3.27.

Nodal deflections ranged from a minimum of 0.111 inch at the base of the dome to a maximum of 2.90 inches toward the crown of the dome. Out-of plane deflections remained below 0.4 inch on the unloaded side of the dome, while larger displacements were observed on the loaded portion of the dome surface. The perimeter of the loaded surface exhibited deflections which fell within the 1.4 to 1.8 inch range. The lower regions within the slices displaced approximately 2 inches, and the seam regions leading into the upper areas of the loaded dome surface displaced 2 to 2.9 inches. Since the loading was not symmetric over the entire surface, the corresponding slot displacements also varied. The maximum slot displacement of 1.28 inches occurred at the eastern slot. The north and south slotted supports each experienced radial movements of 0.6 inch, while the western slotted support had a minimal outward radial translation of 0.121 inch.

Nodal rotation values at the service load ranged from a minimum of 0.002° at the transition layer nodes to 2° at the tensile ring nodes. It is also worth noting that relatively large rotational values with respect to the remainder of the structure were also found around the perimeter of the loaded surface. This observation is indicative of the early formation of a "dimple" or snap-through area which encompassed the loaded surface of the dome.

Axial stresses in the tension ring were maximum at the eastern edge of the ring (8,122 psi) and attenuated to a minimum tension value of approximately 1,600 psi at the western ring segment, shown clearly in Figure 3.28. In addition, Figure 3.29

provides a reasonable interpretation of the axial stress distribution within the dome spars. Highest compressive stresses were found in the transition diagonals near the north and south ends and in the upper ring segments of the eastern face of the dome (6,000 psi ~ 7,000 psi). Seams, interslice regions, and lower rings and diagonals within the loaded portion of the dome experienced compressive axial stresses in the 2,000 psi to 5,000 psi range. Negligible stresses (< 1,000 psi) were observed amongst the diagonals emanating from the loaded seams, the lower segment of the unloaded face, and seam diagonals on the western face. The upper segment of the unloaded surface experienced tensile stresses within the range of 1,000 to 3,000 psi, and larger tensile stresses were found within the tension ring.

With reference to the edges defining the loaded surface, it was found that the largest bending moments and shearing forces were located in this area, while minimal moments and shears were located within the edges defining the unloaded "patch" of the dome.

This particular loading resulted in a nonuniform distribution of vertical support reactions. The maximum vertical nodal load transmitted through the supports was 17,700 pounds at the eastern support, while the minimum load of 1,368 pounds was placed upon the western support. The anticipated instability stemming from the boundary of the loaded surface is shown quite clearly through the deformed shape displayed in Figure 3.30.

b) Critical Load

The bare-frame dome subjected to half snow load experienced instability at a load corresponding to 56.5 psf, which equated to a snow load of approximately 1.1 million pounds on the eastern face of the dome.

Nodal deflections ranged between 0.23 and 6.65 inches. The top of the dome deflected downward 1.49 inches, and 0.43 inch in the westward direction. The easternmost point of the base support slid outward 2.99 inches, and the minimum radial movement, located at the west support point was 0.25 inch. The 3 inch slotted support plate had no effect upon the outcome of the buckling analysis, since every slot remained open up until collapse occurred. As seen in Figures 3.31 and 3.32, nodal deflections greater than 0.8 inch were to be found on the loaded surface of the dome. Maximum nodal deflections ranging from 5.8 to 6.6 inches occurred toward the top of the dome and down the seams into the transition segments within the loaded surface. Moderate displacements, those less than 5 inches, occurred within the interslice regions and gradually diminished toward the loading boundary.

Nodal rotation indicated that out-of-plane rotations approaching 5° occurred in the proximity of the tension ring nodes and the edge of the loading patch running up the North-South meridian of the dome. As mentioned in the previous section, the dimpling effect was within the loaded segment of the dome. Although the entire surface had not become unstable, snap-through of the loaded surface of the dome had occurred. This is touched upon further toward the end of this section.

Maximum axial tensile stresses ranging from 10,000 psi to 18,878 psi occurred in the base tension ring, with the lower stresses on the unloaded segment and the higher stresses on the loaded side of the dome (Fig. 3.33). Compressive stresses of 13,000 psi to 16,000 psi were located in the transition segments near the North and South ends of the dome. A majority of the compressive axial stresses fell within the 2,000 to 13,000 psi range, in members on the loaded side of the dome, excluding the base ring and the outer seam diagonals. Negligible compression was exhibited by the lower and midheight diagonals and seams on the unloaded face, and by a limited number of interslice diagonals found within the loaded patch. Small tensile axial stresses of 1000 to 4000 psi were found in the rings located in the bottom half of the unloaded surface and also in a limited number of diagonal elements emanating from the seams in the midsection of the loaded surface of the dome. The largest tensile stresses, excluding those found in the tension ring, were located within the North-South oriented members of the unloaded face.

The larger spar bending moments, just as in the service load state, were concentrated at the borders which define the loading patch, with gradually diminishing values progressing into the unloaded section of the dome.

The result of increasing the applied load to a critical level of 56.5 psf was the dimpling or snap-through of the loaded surface of the dome. The unloaded portion of the dome acted as a support mechanism in that it provided structural support for the remainder of the dome due to its added stiffness. Since the dome was essentially supported upon itself, a higher critical load was able to be achieved. The inherent weakness at the base of the dome which contributed to the "softening" discussed in earlier sections was still an obvious factor in the buckled shape, as seen in Figure 3.34.

3.7.4 DHSNLCB RESULTS (full snow / cladded)

a) Service Load

The nodal deflections for this particular load case of a fully cladded dome subjected to the same half snow load (25.7 psf) on its eastern face ranged from 0.08 to 1.82 inches. The crown of the dome deflected down 0.68 inch and westward 0.07 inch. As seen in Figure 3.35, larger dome displacements in the 1.6 to 1.8 inch range were concentrated in the transition layer of the loaded portion of the dome. The 1.8 inch displacement values were centered about the easternmost point of the transition layer (lower part), and gradually diminished toward the unloaded locations which began at the North and South ends of the dome. The slotted supports moved radially outward and decreased in magnitude from 1.14 to 0.08 inch progressing from the east point to west point of the supports. The resulting deflected shape is seen in Figure 3.36.

Large relative values of nodal rotations (1.6°) were found on the lower eastern segment of the dome, particularly below the transition layer. This observation was consistent with previous nodal rotation observations in that the dimple mentioned in the last section was in the process of forming, and will govern the mode of buckling in the cladded case. The cladding did not prevent the dimple from forming, although it did lessen the nodal rotations about the remainder of the loaded perimeter due to increased in-plane stiffness.

Axial stress distribution in this cladded model gave way to large tensile stresses between 5,000 and 7,284 psi in the loaded section of the tension ring. The unloaded segment of the ring experienced stresses of 2,000 to 5,000 psi. The members exposed to the largest compressive stresses (Figs. 3.37 and 3.38) were the lower diagonals in the north and south regions of the dome which led into the loaded area of the dome (2,500 psi ~ 3,260 psi). Moderate values of compression were found in the upper ring segments of the loaded portion of the dome (2,000 psi ~ 2,500 psi) while minimal compressive stresses were located in the lower portion of the loaded side of the dome and in the lower to midheight diagonals of the unloaded side of the dome. By observing the "flow" of compressive stresses, it was quite clear that the compressive distribution follows an east-west orientation, in which compression was minimal on the east face and gradually increased toward the eastern edge of the surface. Tensile axial stresses increased from the North and South upper diagonals (≤ 1,000 psi) leading into the rings on the unloaded side (1,000 psi ~ 2,000 psi). Larger values of tension (2,000 psi ~ 5,000 psi) were located in the lower North and South diagonals leading into the lower ring segments of the unloaded portion of the dome.

As in the previous load case, the maximum bending moments and shearing forces occurred near the boundary defining the loaded patch. The minimum bending moments and shearing forces were within the unloaded segment of the dome.

The skin stresses for this case indicated a highly stressed lower loaded portion of the dome (Fig. 3.39). Tensile stresses in this area ranged from 6,135 psi at the east lower level to 2,000 to 5,000 psi at the North and South base portions of the dome. Skin tension fell below 2,000 psi along the North-South meridian line and virtually disappeared toward the west edge transition layer.

The load transfer into the supports produced a nonuniform distribution of support reactions. The maximum vertical load transmitted through the supports was 17,064 pounds at the eastern support, with a minimum load of 1,112 pounds at the western support.

b) Critical Load

The dome was loaded beyond the service load until numerical divergence of the solution occurred. The point at which this took place signified the critical state of the structure, indicative of buckling. In this case, the buckled shape was similar to the dimpled shape of the bare-frame subjected to its critical value of half snow load. The critical load corresponding to this buckled shape was 63.0 psf, the highest load of all load cases.

The loading at the critical level induced nodal deflections (Fig. 3.40) which ranged from 0.17 inch on the unloaded side, to 5.07 inches at the center of the transition segment on the loaded side of the dome. The displacement of the loaded segment of the transition layer gradually reduced to 4.2 inches toward the North and South edges of the layer. The remainder of the loaded patch experienced displacements between 3 and 4.2 inches. Moving west along the surface of the dome, a range of 1.6 to 1.8 inches was representative of the displacements from the crown area to the lower locations of the unloaded half of the dome. Slot movement was limited to 2.99 inches of outward radial displacement at the east support to 0.19 inch at the west support. Thus, with a slot allowing a radial expansion of 3 inches, slot bearing was not a factor in any of the studied load cases.

Nodal rotations that are relatively large (4.6°) define the path which represented the border surrounding the loading patch. These large values of rotation defined the edge of the dimple which characterized the snap-through failure mode affecting the loaded portion of the dome.

In this load case maximum axial tensile stresses ranging from 4,000 to 19,036 psi occurred in the base tension ring, with the lower stress values favoring the unloaded segment of the ring and the higher stresses on the loaded side of the dome (Figs. 3.41 and 3.42). Compressive stresses from 6,000 to 8,839 psi occurred in the transition segments near the North and South ends of the dome. The majority of compressive axial stresses ranged from 2,000 to 5,000 psi and were within the midheight rings of the loaded portion of the dome. Lower stresses were concentrated within the upper diagonals near the North-South meridian line and also within the lower diagonals on the loaded side of the dome. Negligible axial compressive stresses less than 1,000 psi were within the lower diagonal members of the unloaded dome segment. Tensile axial stresses of 1,000 to 4,000 psi were located in the lower unloaded ring elements and in the North-South oriented members of the unloaded face. Axial stresses greater than 4,000 psi were reserved for the tension ring members.

Beam bending moments and end shearing forces were largest within the layers below the loaded segment of the transition layer and around the remainder of the perimeter defining the boundary of the loaded surface, which tends to explain the dimpled shape of the snap-through region of the dome.

The high critical loading of 63.0 psf before the forementioned snap-through instability was benefitted by the cladding. It provided additional in-plane restraint, coupled with the inherent support of the unloaded half of the dome, and allowed for additional load to be applied to the structure. The higher applied load was reflected through the higher skin stresses at the critical load. Skin tension (Fig. 3.43) exceeded 16,000 psi at the lower eastern layer of the dome and dissipated toward the north and south layers of the dome. Minimal tension (1,000 psi ~ 2,000 psi) was observed along the North-South meridian line with negligible values toward the western side of the dome.

The deformed shape of the cladded dome (Fig. 3.44) was quite similar to the critically deformed shape of the bare frame in the previous case.

3.8 COMPARISON OF RUNS

Of the four cases analyzed, the bare-frame dome subjected to full snow loading (DSNLB) buckled under the smallest load, 49.1 psf. Figure 3.45 shows the increase of critical load value for the four load cases. The cladded dome under full snow load (DSNLCB) withstood a critical load 10.9% higher than its bare-frame counterpart, while the bare-frame (DHSNLB) and cladded domes (DHSNLCB) subjected to half snow loading withstood critical loads 15.1% and 28.3% higher, respectively, than that of the bare-frame full-snow-load case.

Maximum deflection values of the different dome scenarios at the service load are shown in Figure 3.46. Although each dome experienced virtually the same load per square foot at the service load, the bare-frame dome under full snow load had a maximum deflection 34.7% greater than the cladded run. With half snow load, the bare-frame dome had a maximum nodal deflection 53.8% greater than the cladded case.

At critical load (Figure 3.47), the maximum deflection of the bare-frame dome under full snow load was 22.1% larger than the cladded dome. The bare-frame dome subjected to half snow load buckled at a load 11.5% smaller than its cladded counterpart, yet its maximum deflection was 31.1% larger than the cladded dome.

Clearly, cladding provided for an additional measure of stability in the dome. The skin acted as a "bracing system" which constrained the dome, and in turn, lessened deflections. Therefore, the decreasing trend in service load deflections seems reasonable. Since the cladded dome was increasingly restrained, higher critical loads can be achieved. Even though the cladding restraint results in lesser values of maximum nodal deflection at critical load, the percentage difference between service load and critical load was also reduced.

Maximum tensile axial stresses under idealized service loading conditions (Figure 3.48) showed that the addition of cladding decreased the maximum stresses by 6.4% and 10.3%, respectively, in the full and half snow load cases. At the critical load (Figure 3.49), there was only a 1% difference in stress amongst all analyzed load cases, showing the insensitivity to change in maximum tensile stress regardless of loading configuration or structural configuration (cladded or uncladded).

Due to the increased overall in-plane stiffness of domes with cladding, the cladded structure experienced a 59% decrease in the maximum compressive axial stress under fully symmetric service snow load (Figure 3.50); with half snow load, a 54% decrease in maximum axial compressive stresses occurred. At the critical load, there was a reduction in compressive axial stresses of 45% for both load cases (Figure 3.51). The elevated values of compressive stresses in the half snow load cases were due to the pinching effect at the north and south base regions of the dome. Unlike the tensile axial stress characteristics, compressive stresses in the dome were sensitive to changes in geometry (i.e. the addition of cladding).

In the two cases that incorporated cladding, the dome exhibited a 127% increase in the maximum skin stress between service and critical loads under fully symmetric loading (Figure 3.52), whereas the half snow load resulted in a 161% increase in maximum skin stress from service load to critical load.

With all differences in deflection and stress levels taken into account, the most noticeable observation from all four load cases is that the allowable stress levels (axial stresses) of all structural elements in every case are not exceeded, even at the critical limit load. This observation conclusively showed that the dome is conservatively designed and that greater efficiency in the overall design is possible.

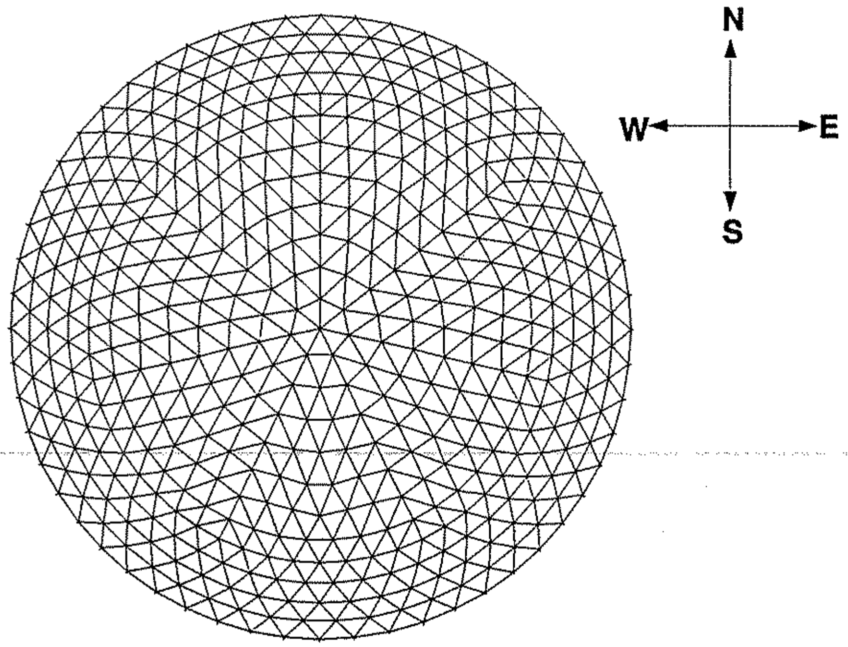

PLAN VIEW

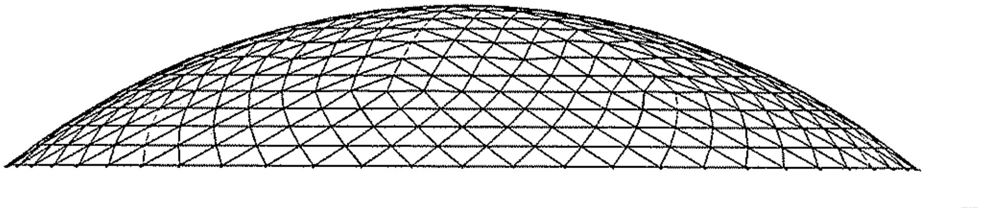

ELEVATION VIEW

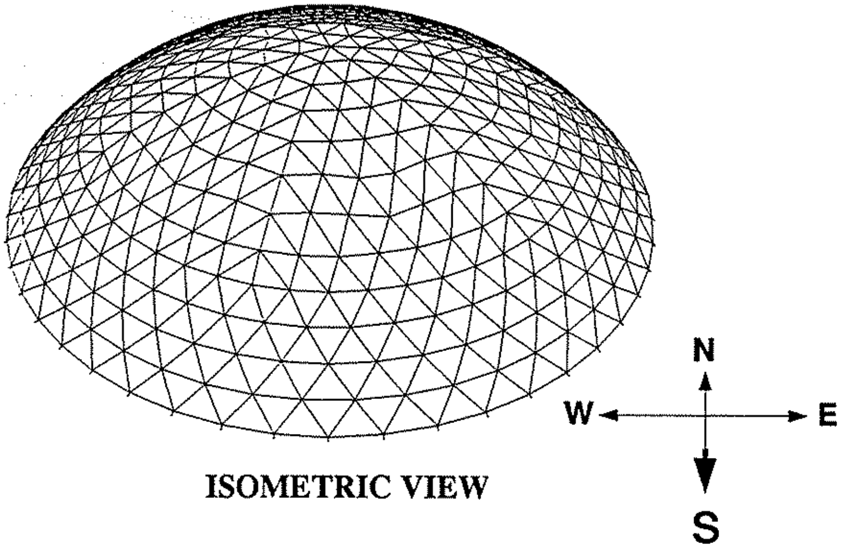

ISOMETRIC VIEW

Figure 3.0: Graphical Orientation

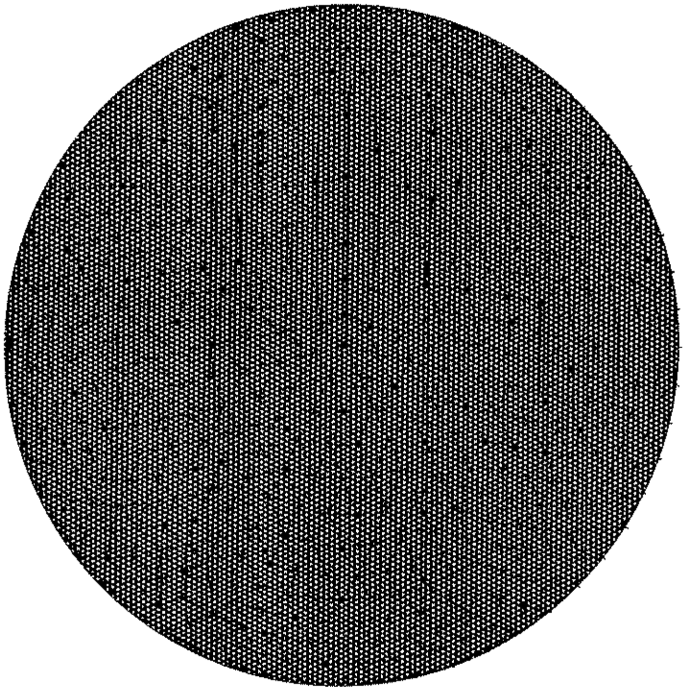

Full Snow Load

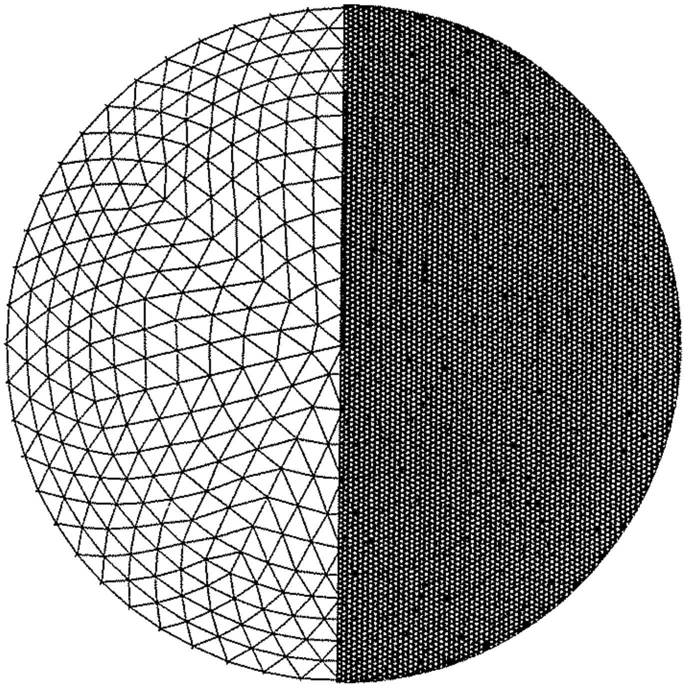

Half Snow Load

Figure 3.1: Loading Configurations

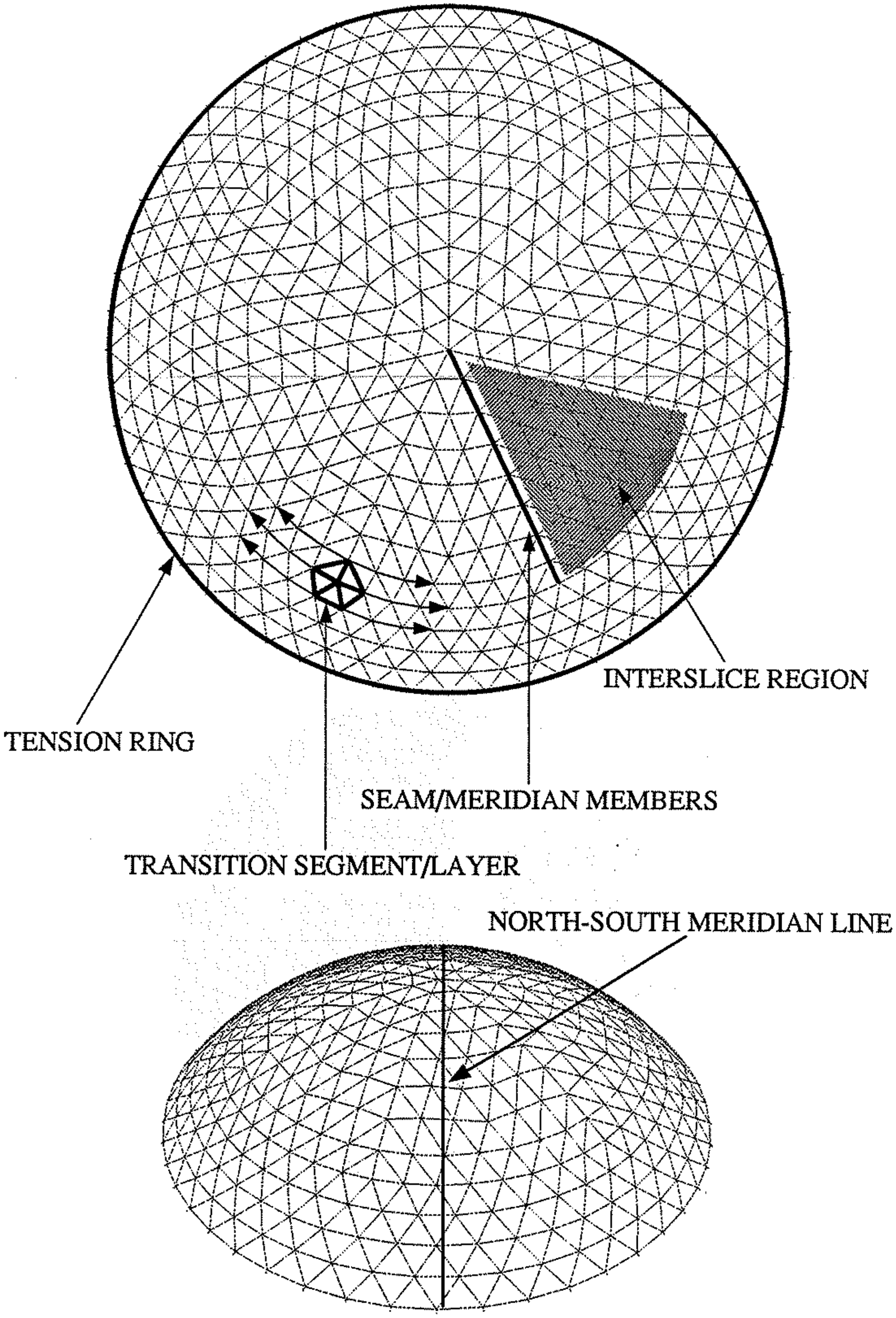

Figure 3.2: Graphical Definitions

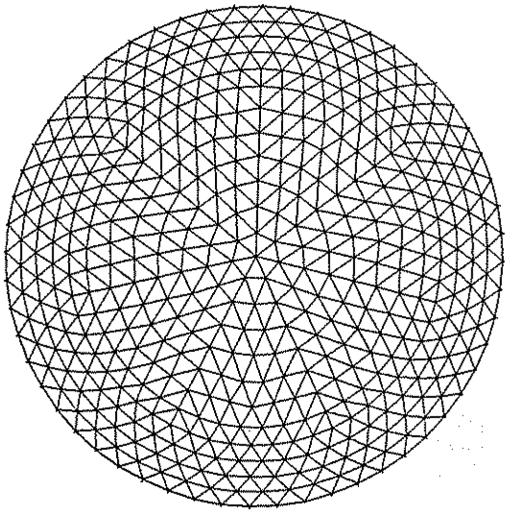

Figure 3.3: Node and Strut Assemblage

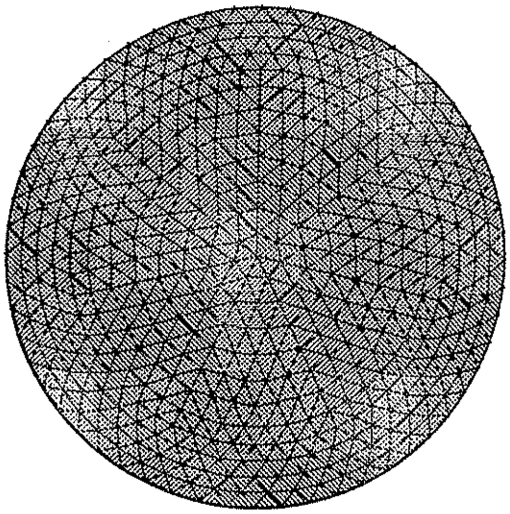

Figure 3.4: Cladded Model

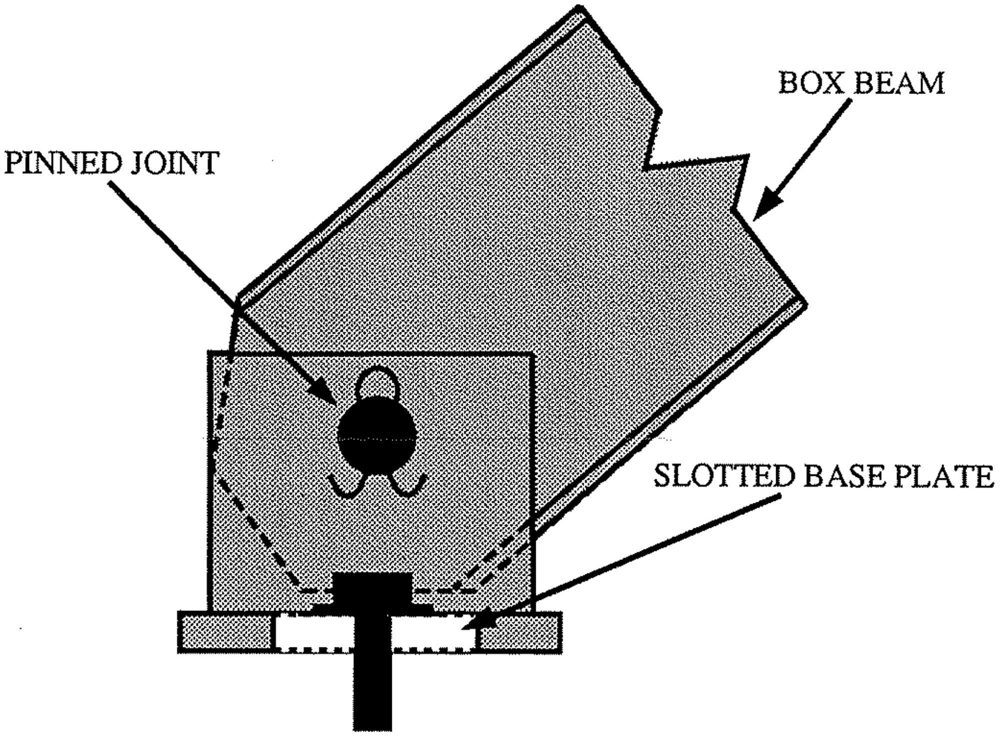

Actual Support Mechanism

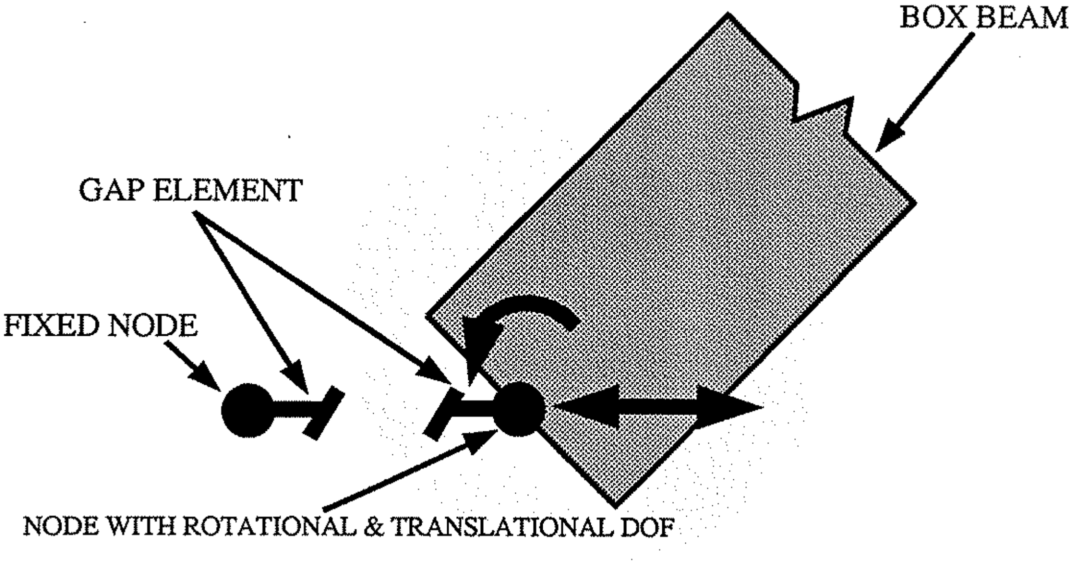

Finite Element Model Support Mechanism

Figure 3.5: Geodesic Dome Pinned/Slotted Support Mechanism

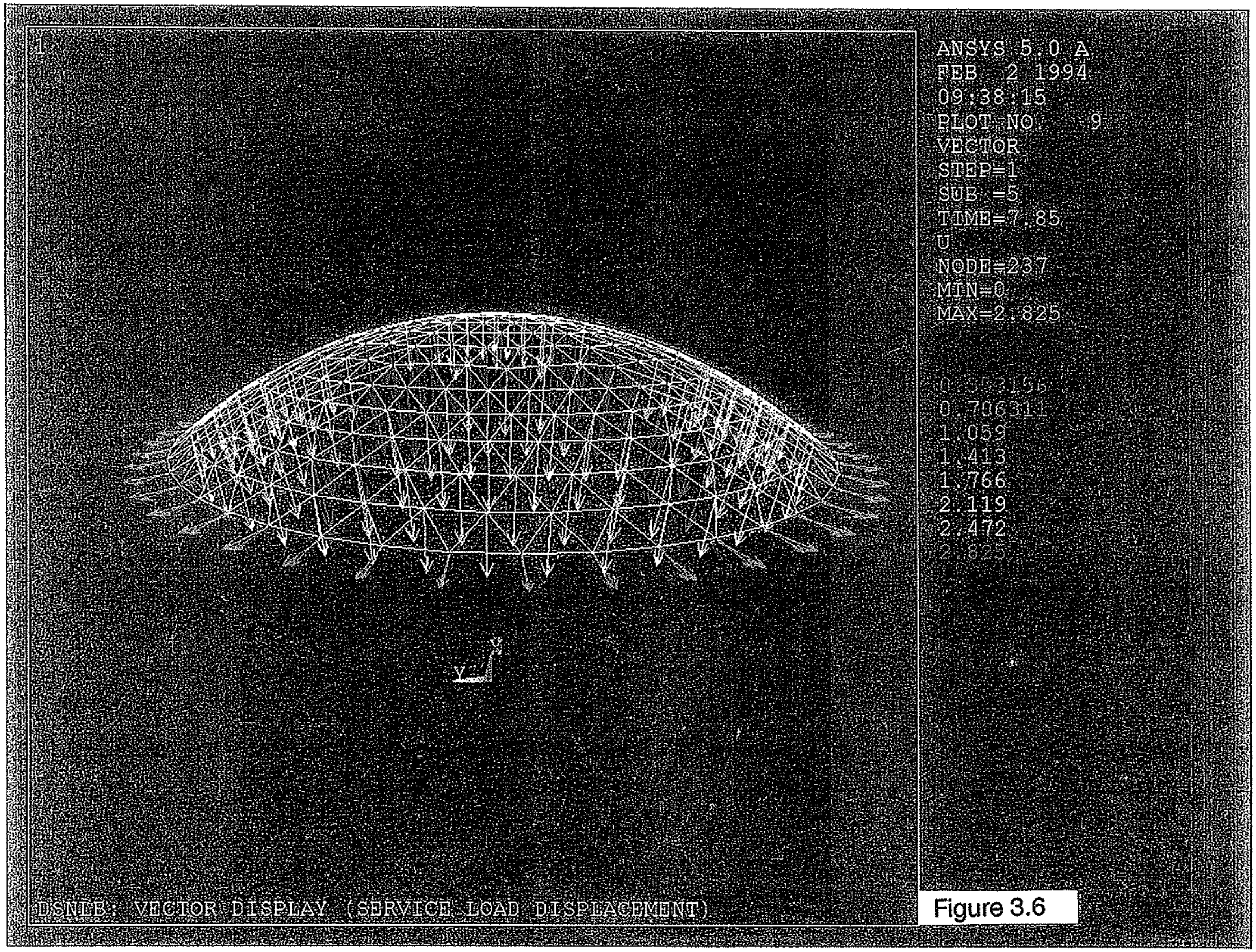
1
ANSYS 5.0 A
FEB 2 1994
09:38:15
PLOT NO. 9
VECTOR
STEP=1
SUB =5
TIME=7.85
U
NODE=237
MIN=0
MAX=2.825
0.353156
0.706311
1.059
1.413
1.766
2.119
2.472
2.825
Y
X
DSNLB: VECTOR DISPLAY (SERVICE LOAD DISPLACEMENT)

Figure 3.6

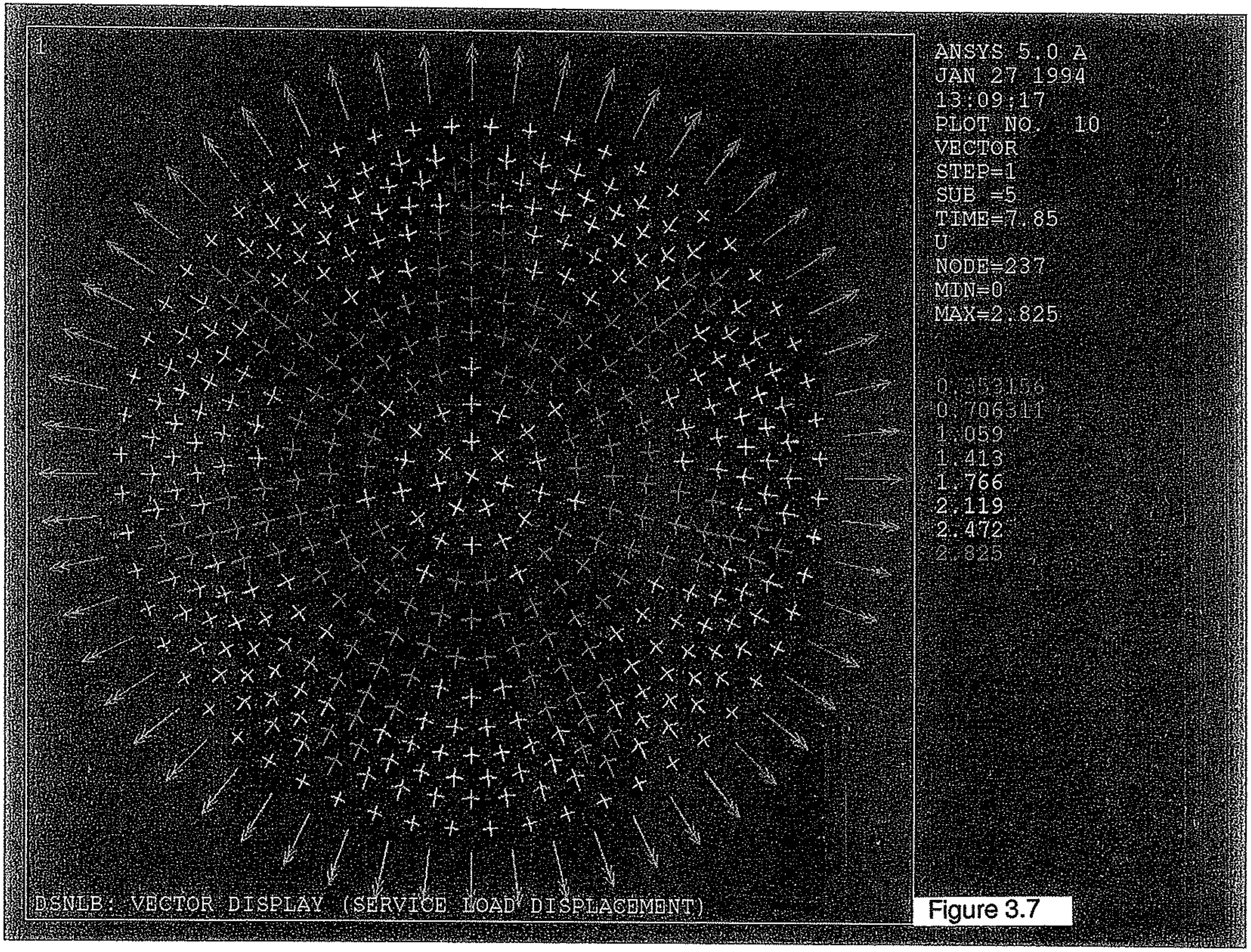
1
ANSYS 5.0 A
JAN 27 1994
13:09:17
PLOT NO. 10
VECTOR
STEP=1
SUB =5
TIME=7.85
U
NODE=237
MIN=0
MAX=2.825
0.353156
0.706311
1.059
1.413
1.766
2.119
2.472
2.825
DSNLB: VECTOR DISPLAY (SERVICE LOAD DISPLACEMENT)

Figure 3.7

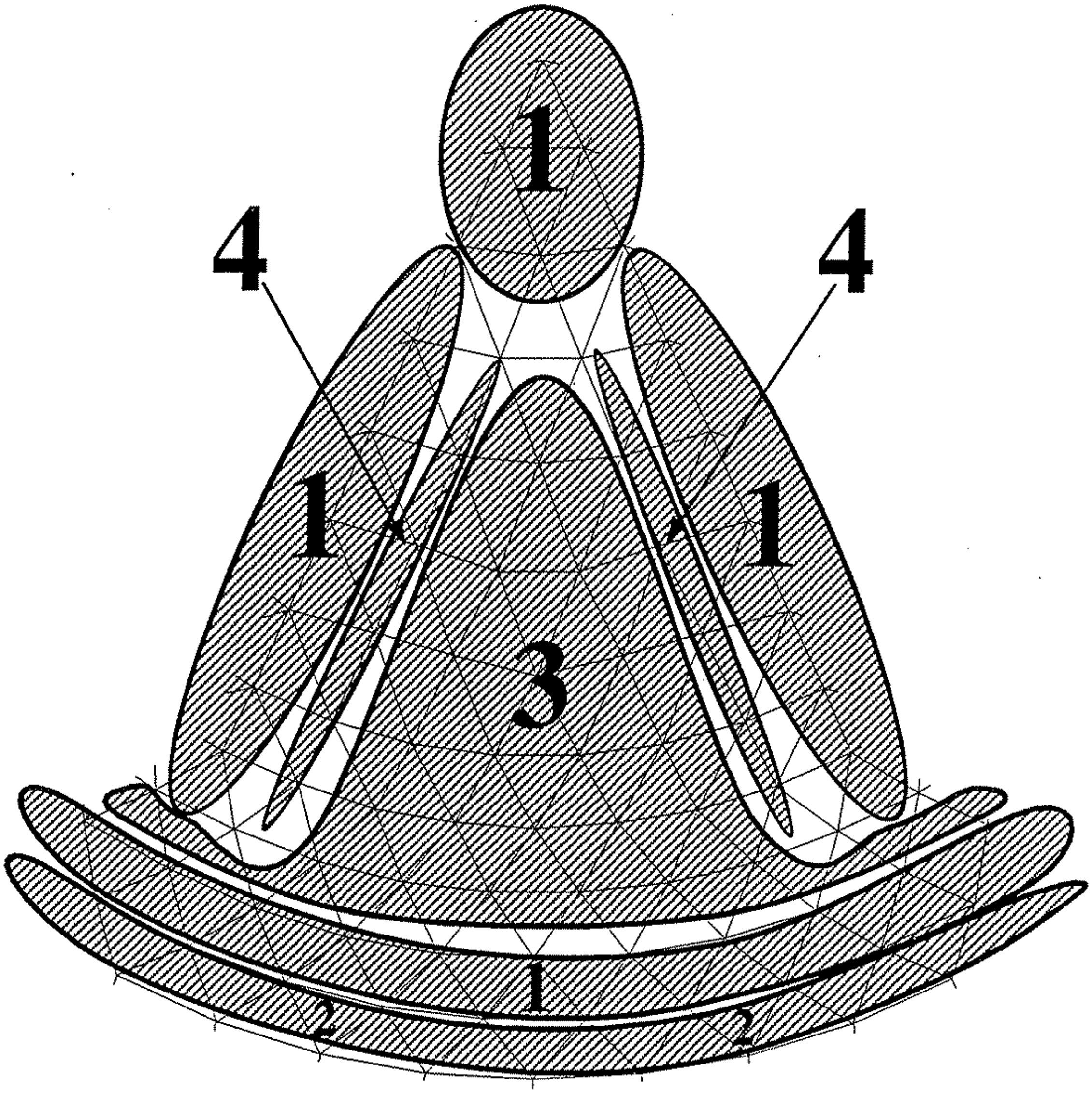

Max Comp **(1) Top rings, seams, second set lower diagonals**

↕ **(2) Lower Diagonals**

(3) Transition members / Interslice members

(4) Diagonals Emanating from seams

Min Comp **Second bottom ring**

Figure 3.8: DSNLB Compressive Axial Stress Distribution (Service Load)

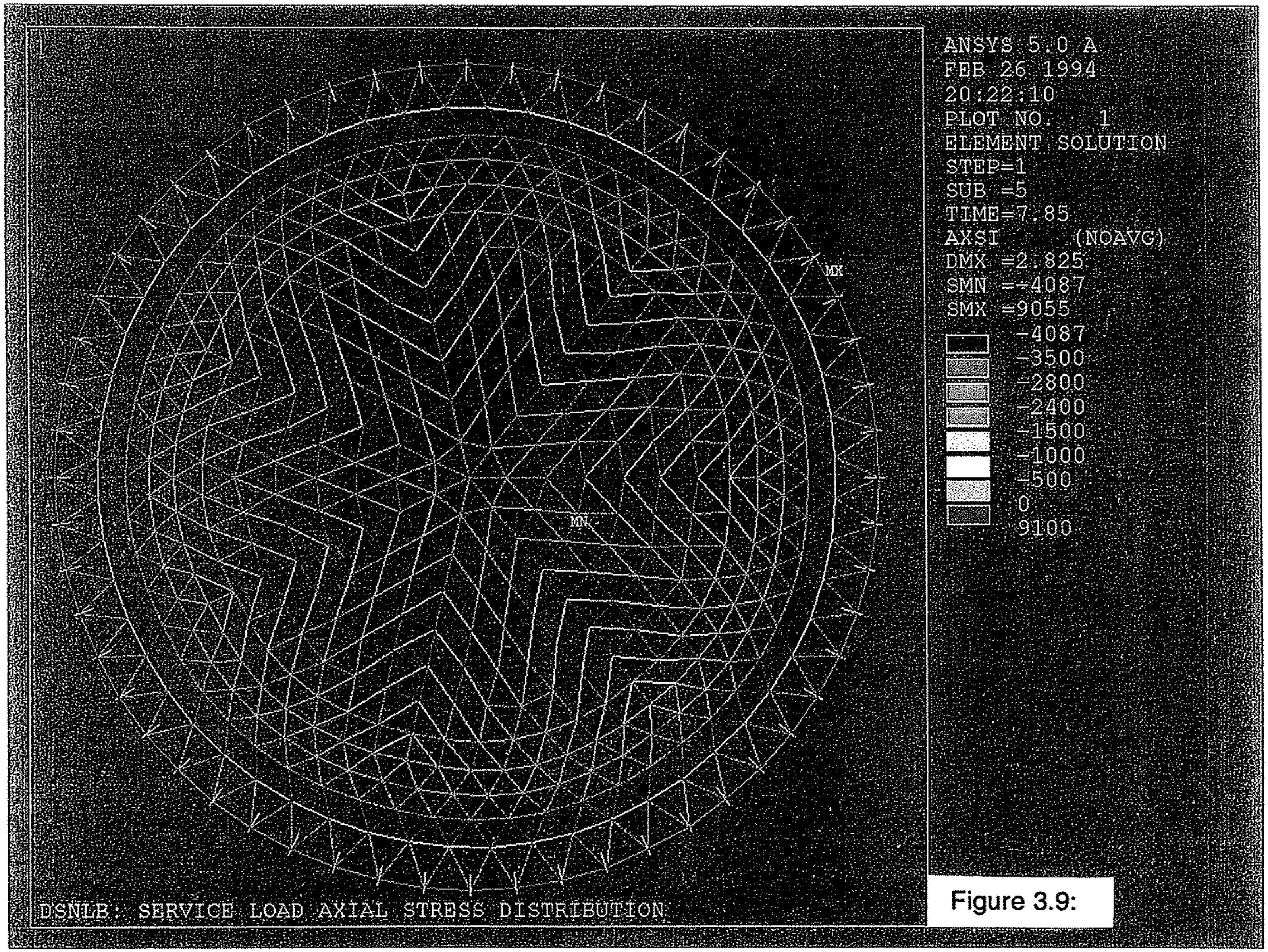
ANSYS 5.0 A
FEB 26 1994
20:22:10
PLOT NO. 1
ELEMENT SOLUTION
STEP=1
SUB =5
TIME=7.85
AXSI (NOAVG)
DMX =2.825
SMN =-4087
SMX =9055
-4087
-3500
-2800
-2400
-1500
-1000
-500
0
9100
MX
MN
DSNLB: SERVICE LOAD AXIAL STRESS DISTRIBUTION

Figure 3.9:

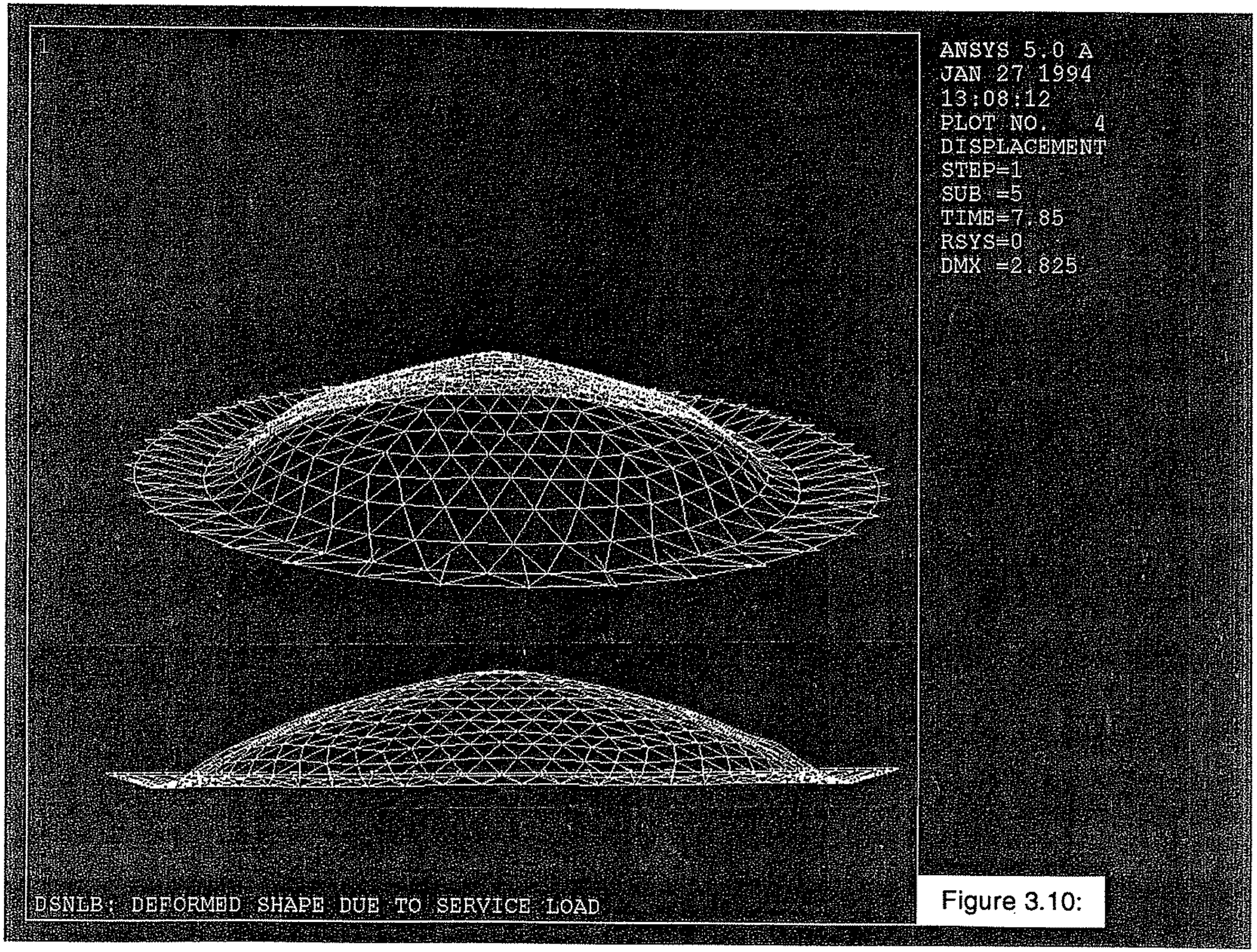
1
ANSYS 5.0 A
JAN 27 1994
13:08:12
PLOT NO. 4
DISPLACEMENT
STEP=1
SUB =5
TIME=7.85
RSYS=0
DMX =2.825
DSNLB: DEFORMED SHAPE DUE TO SERVICE LOAD

Figure 3.10:

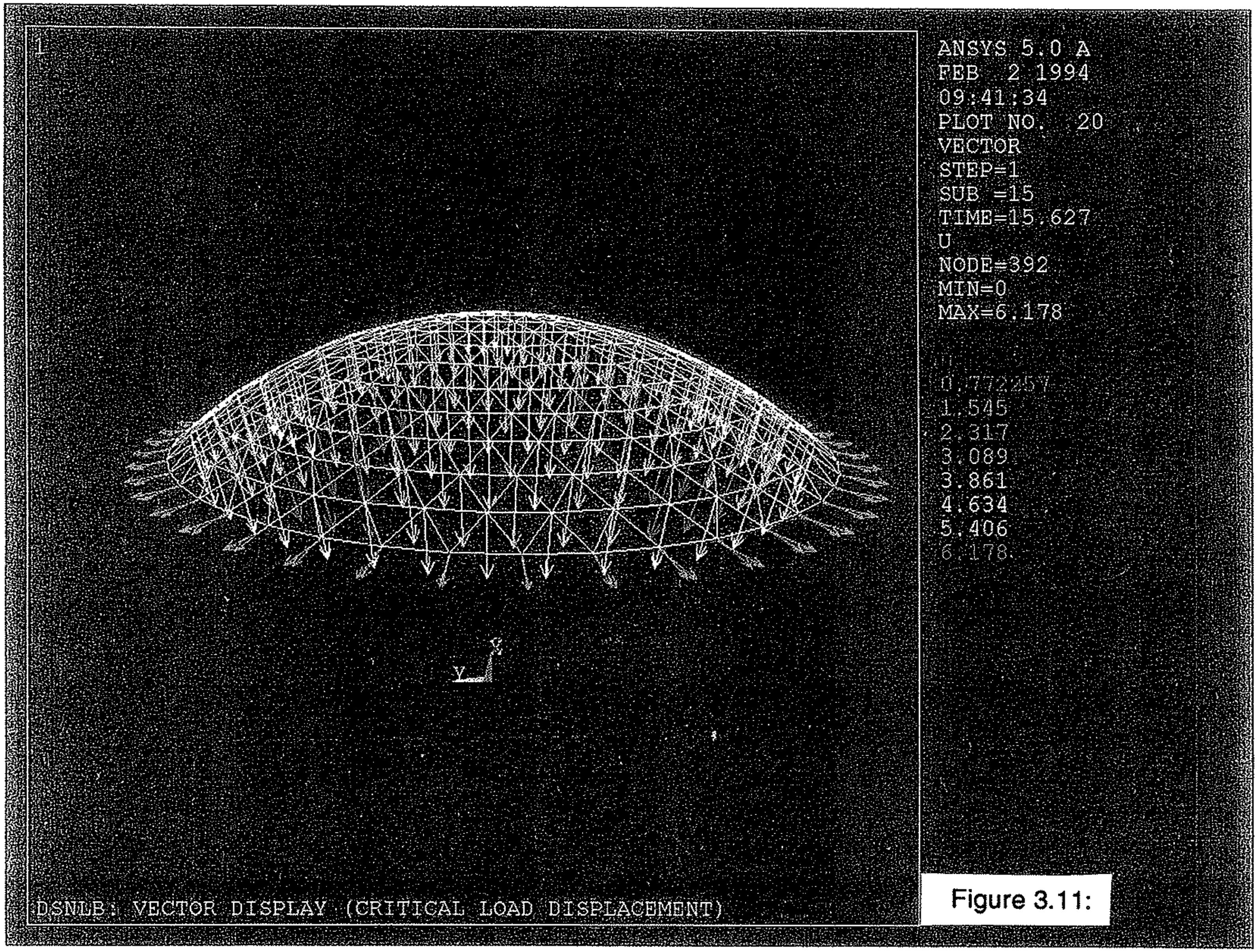
1
ANSYS 5.0 A
FEB 2 1994
09:41:34
PLOT NO. 20
VECTOR
STEP=1
SUB =15
TIME=15.627
U
NODE=392
MIN=0
MAX=6.178
0
0.772257
1.545
2.317
3.089
3.861
4.634
5.406
6.178
Y
Z
X
DSNLB: VECTOR DISPLAY (CRITICAL LOAD DISPLACEMENT)

Figure 3.11:

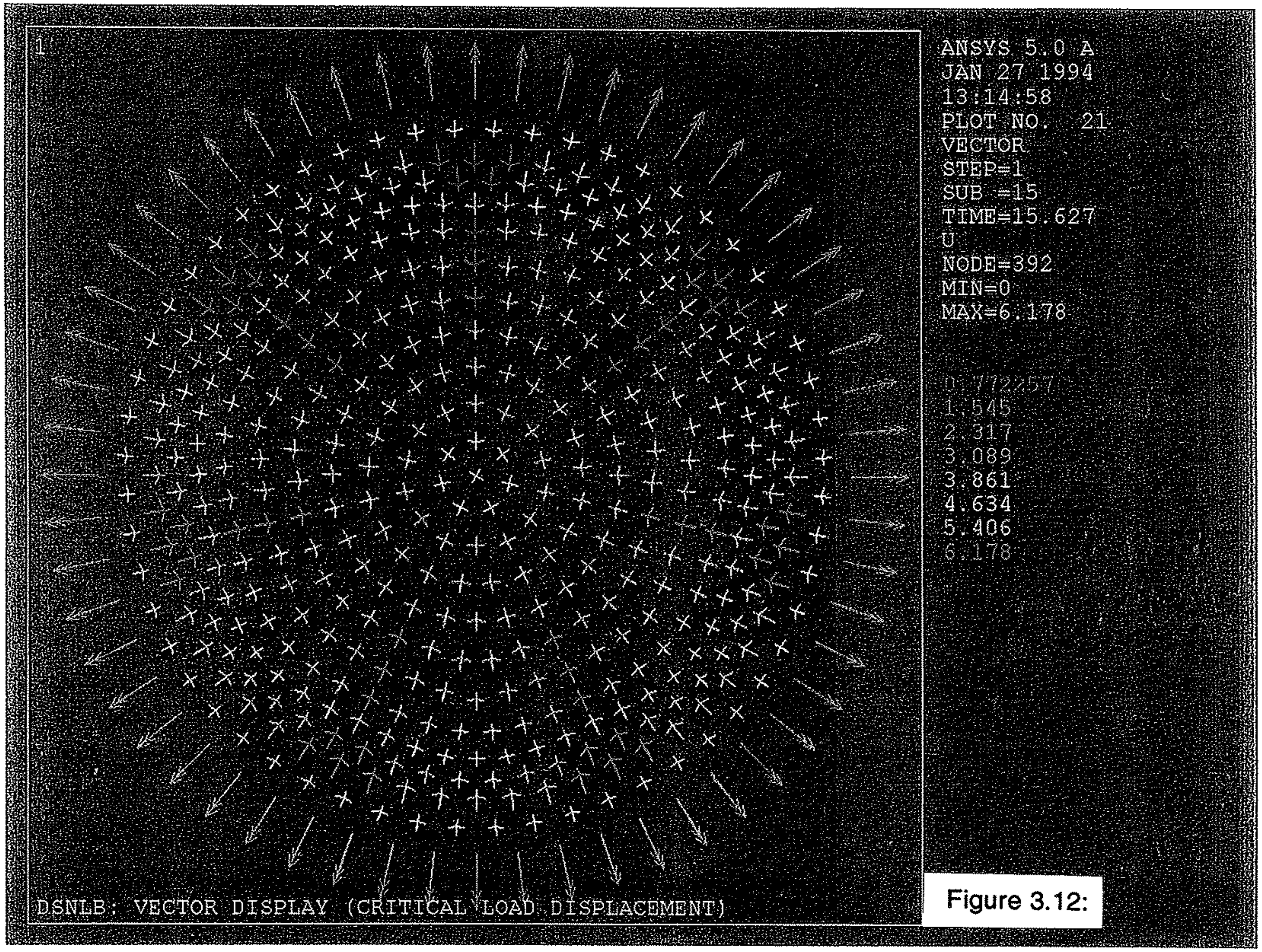
1
ANSYS 5.0 A
JAN 27 1994
13:14:58
PLOT NO. 21
VECTOR
STEP=1
SUB =15
TIME=15.627
U
NODE=392
MIN=0
MAX=6.178
0.772257
1.545
2.317
3.089
3.861
4.634
5.406
6.178
DSNLB: VECTOR DISPLAY (CRITICAL LOAD DISPLACEMENT)

Figure 3.12:

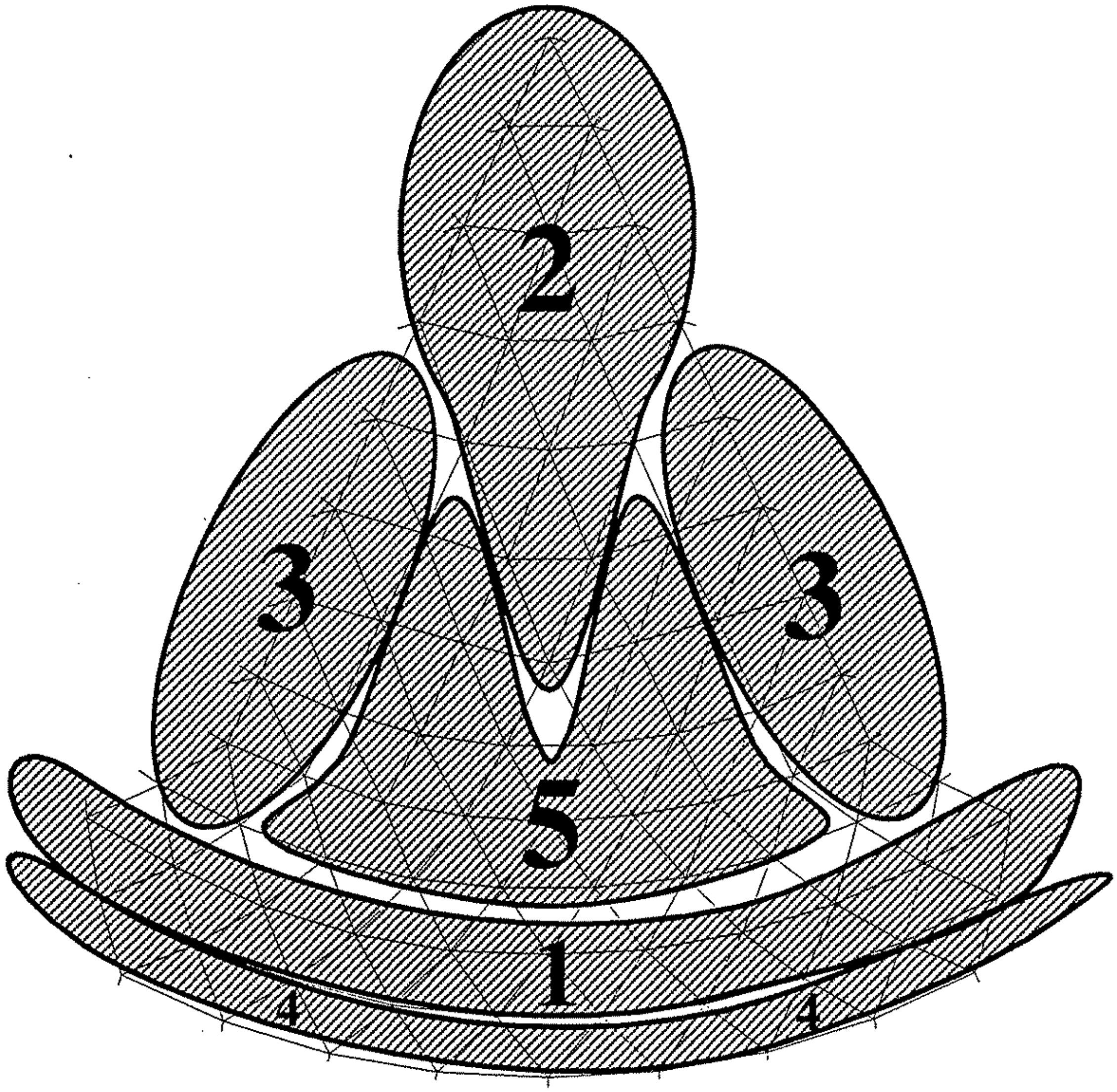

Max Comp (1) Third bottom ring, second set lower diagonals
(2) Upper rings
(3) Seams & Proximity
(4) Lower diagonals
(5) Diagonals emanating from seams & transition members
Min Comp Second bottom ring

Figure 3.13: DSNLB Compressive Axial Stress Distribution (Critical Load)

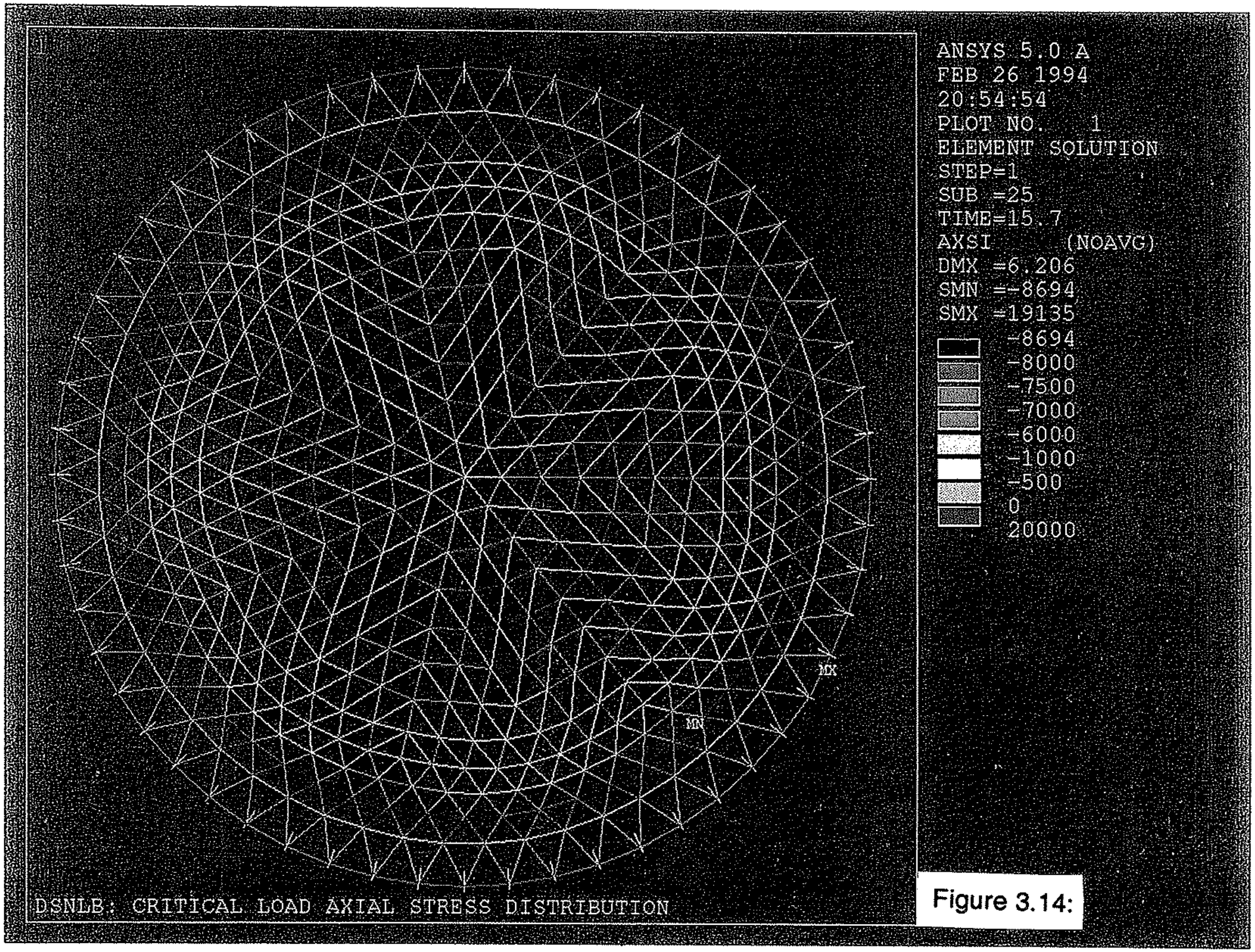

DSNLB: CRITICAL LOAD AXIAL STRESS DISTRIBUTION

Figure 3.14:

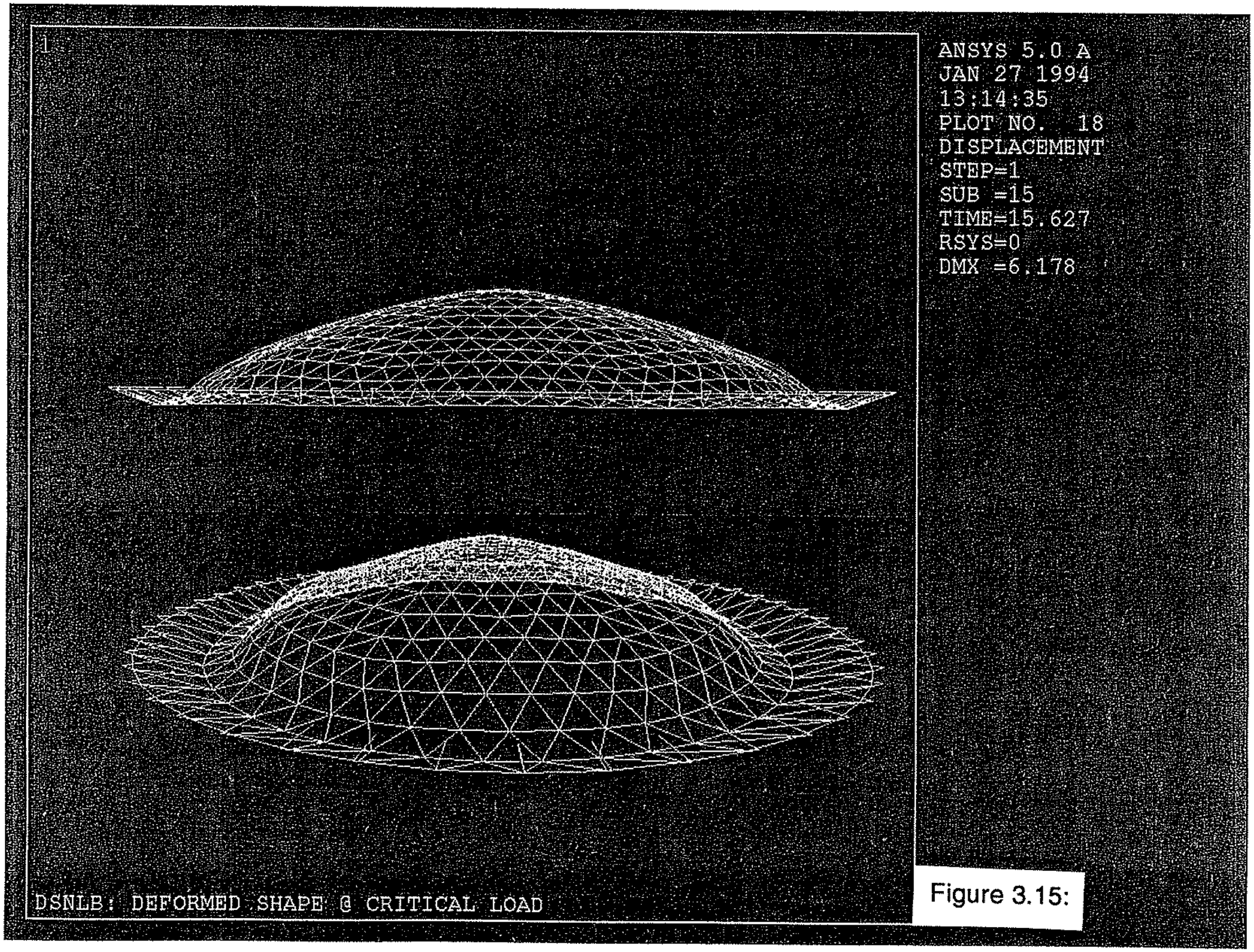
1
ANSYS 5.0 A
JAN 27 1994
13:14:35
PLOT NO. 18
DISPLACEMENT
STEP=1
SUB =15
TIME=15.627
RSYS=0
DMX =6.178
DSNLB: DEFORMED SHAPE @ CRITICAL LOAD

Figure 3.15:

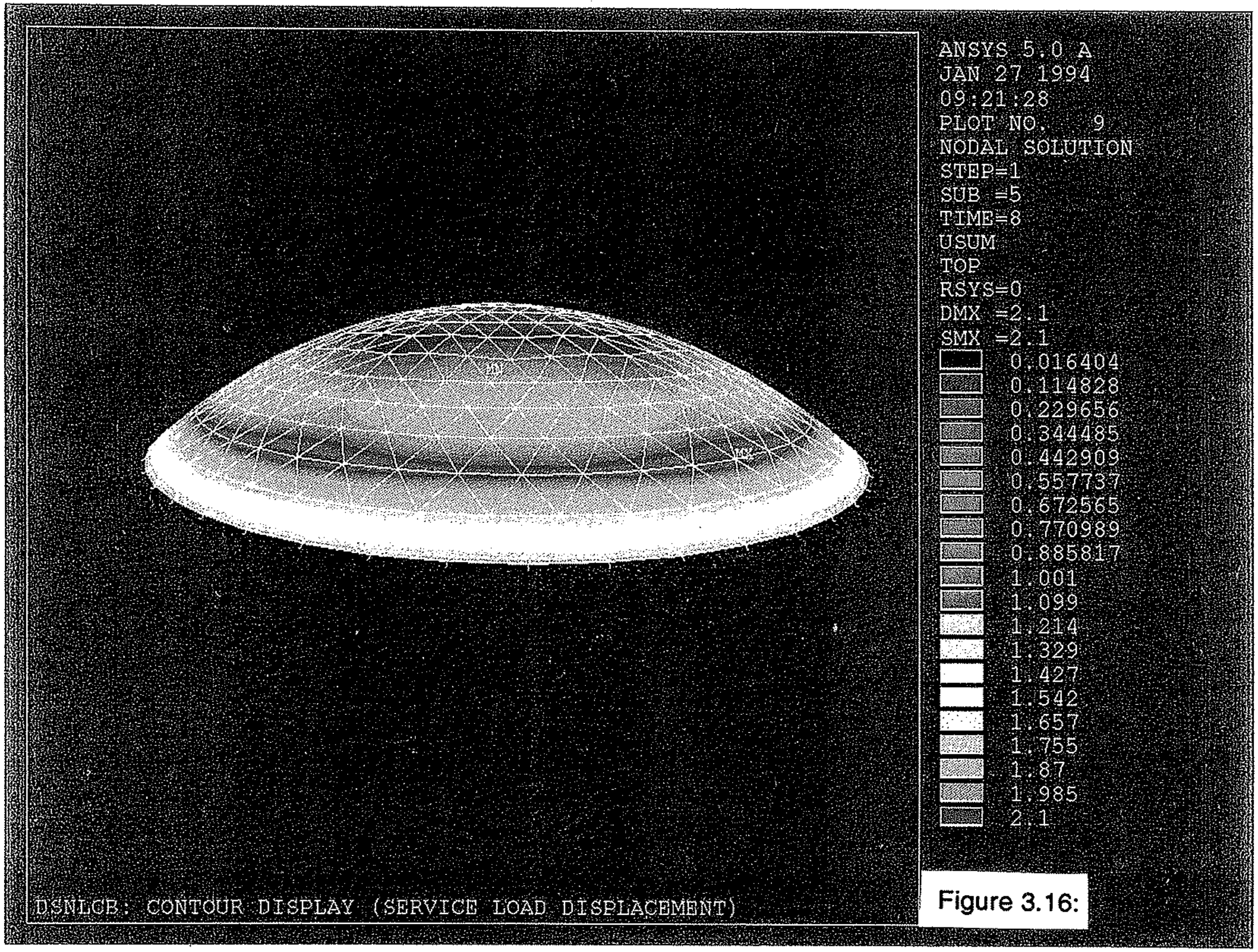
ANSYS 5.0 A
JAN 27 1994
09:21:28
PLOT NO. 9
NODAL SOLUTION
STEP=1
SUB =5
TIME=8
USUM
TOP
RSYS=0
DMX =2.1
SMX =2.1
0.016404
0.114828
0.229656
0.344485
0.442909
0.557737
0.672565
0.770989
0.885817
1.001
1.099
1.214
1.329
1.427
1.542
1.657
1.755
1.87
1.985
2.1
DSNLCB: CONTOUR DISPLAY (SERVICE LOAD DISPLACEMENT)

Figure 3.16:

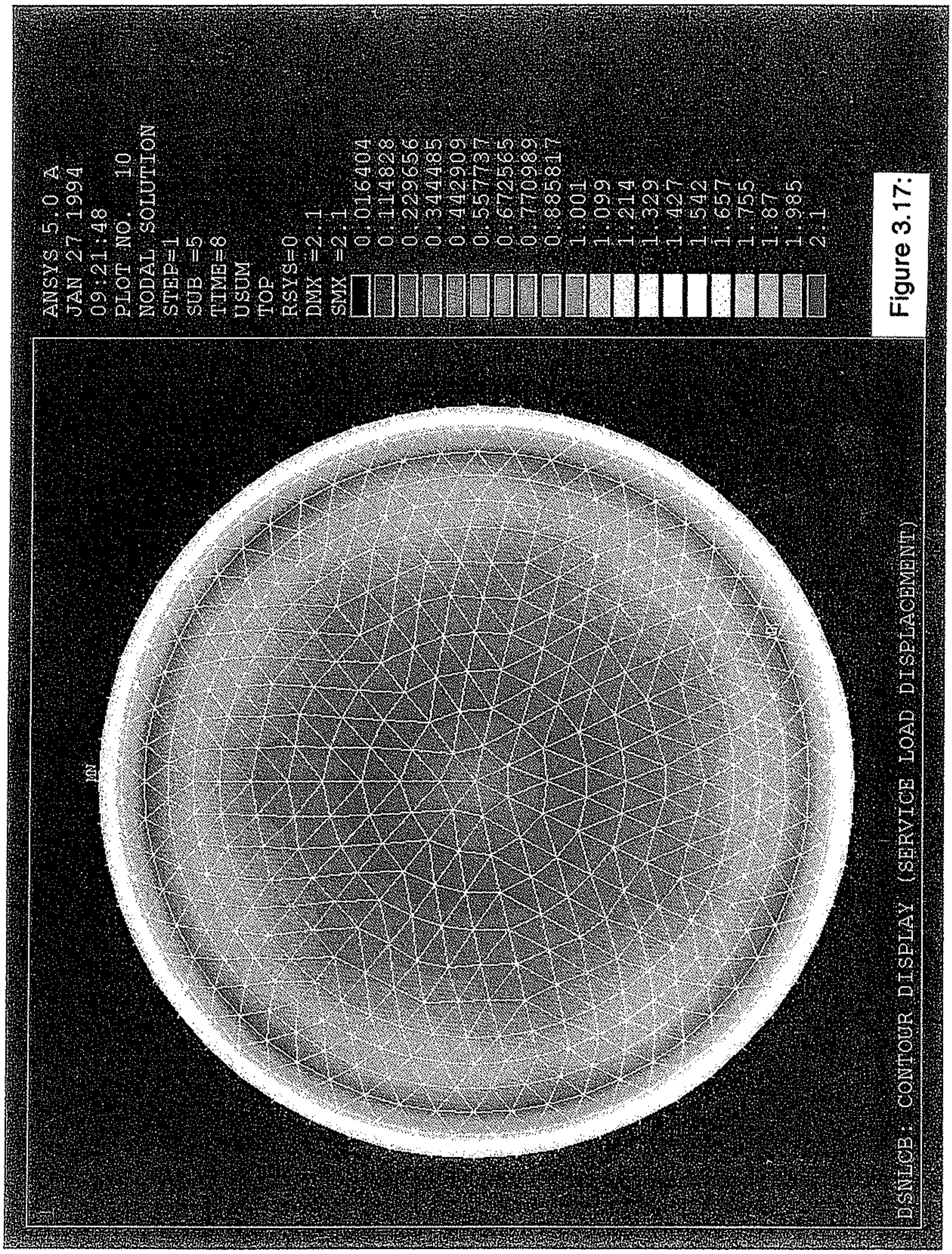
ANSYS 5.0 A
JAN 27 1994
09:21:48
PLOT NO. 10
NODAL SOLUTION
STEP=1
SUB =5
TIME=8
USUM
TOP
RSYS=0
DMX =2.1
SMX =2.1
0.016404
0.114828
0.229656
0.344485
0.442909
0.557737
0.672565
0.770989
0.885817
1.001
1.099
1.214
1.329
1.427
1.542
1.657
1.755
1.87
1.985
2.1
MN
MX
DSNLCB: CONTOUR DISPLAY (SERVICE LOAD DISPLACEMENT)

Figure 3.17:

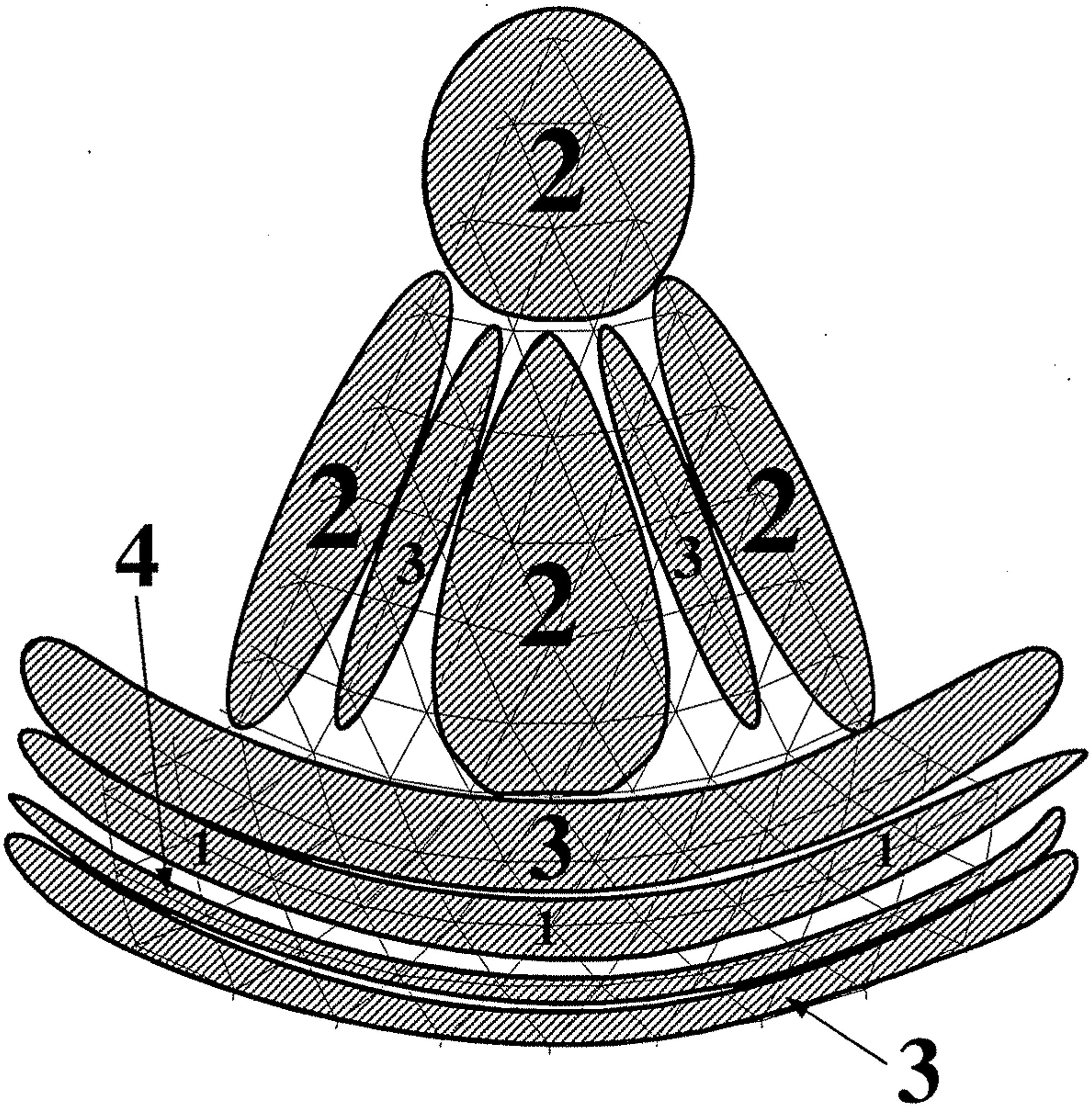

Max Comp **(1) Third bottom ring**
↕ **(2) Seams & interslice regions**
(3) Seam diagonals, Transition rings, & Lower diagonals
Min Comp **(4) Second bottom ring**

Figure 3.18: DSNLCB Compressive Axial Stress Distribution (Service Load)

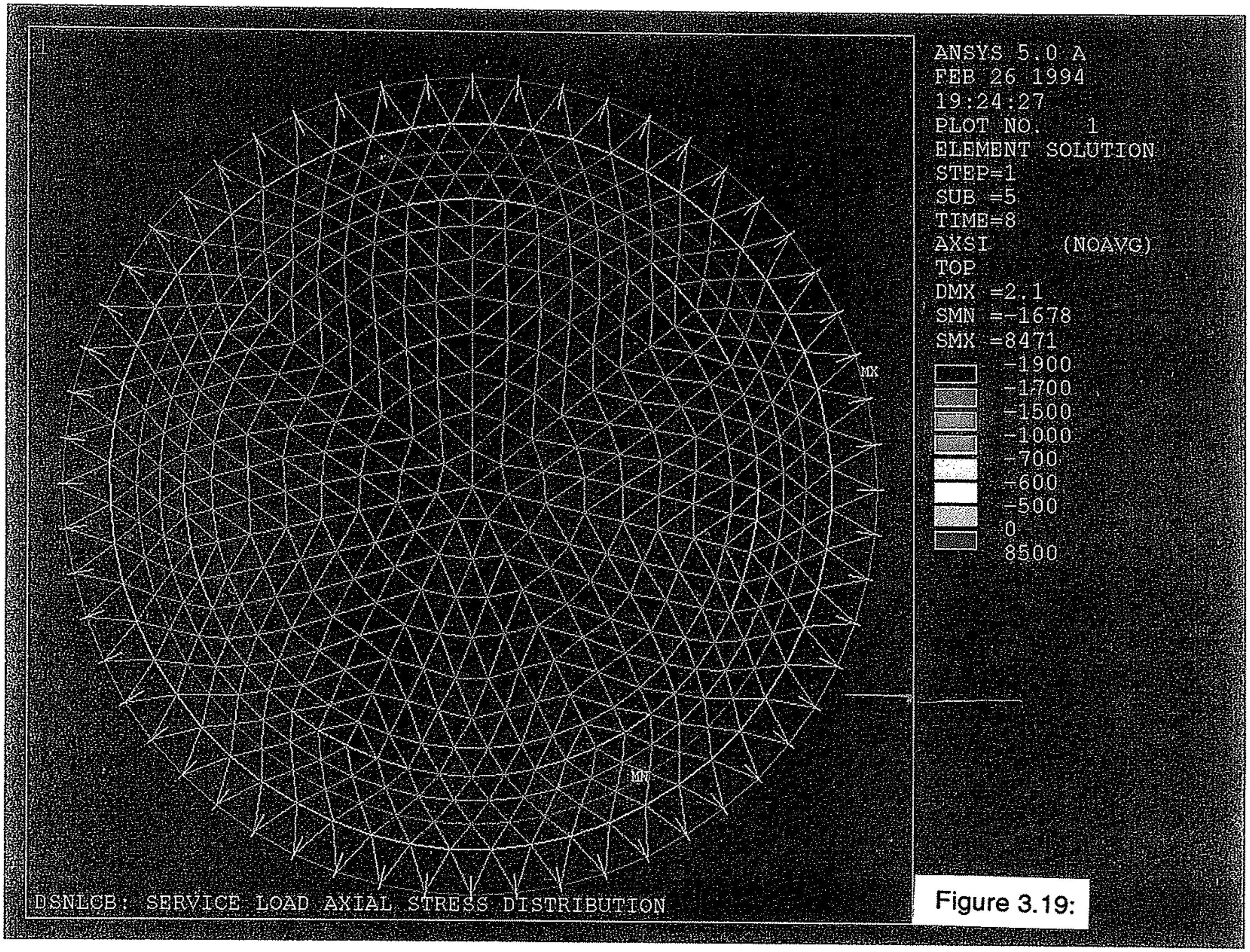
ANSYS 5.0 A
FEB 26 1994
19:24:27
PLOT NO. 1
ELEMENT SOLUTION
STEP=1
SUB =5
TIME=8
AXSI (NOAVG)
TOP
DMX =2.1
SMN =-1678
SMX =8471
-1900
-1700
-1500
-1000
-700
-600
-500
0
8500
MX
MN
DSNLCB: SERVICE LOAD AXIAL STRESS DISTRIBUTION

Figure 3.19:

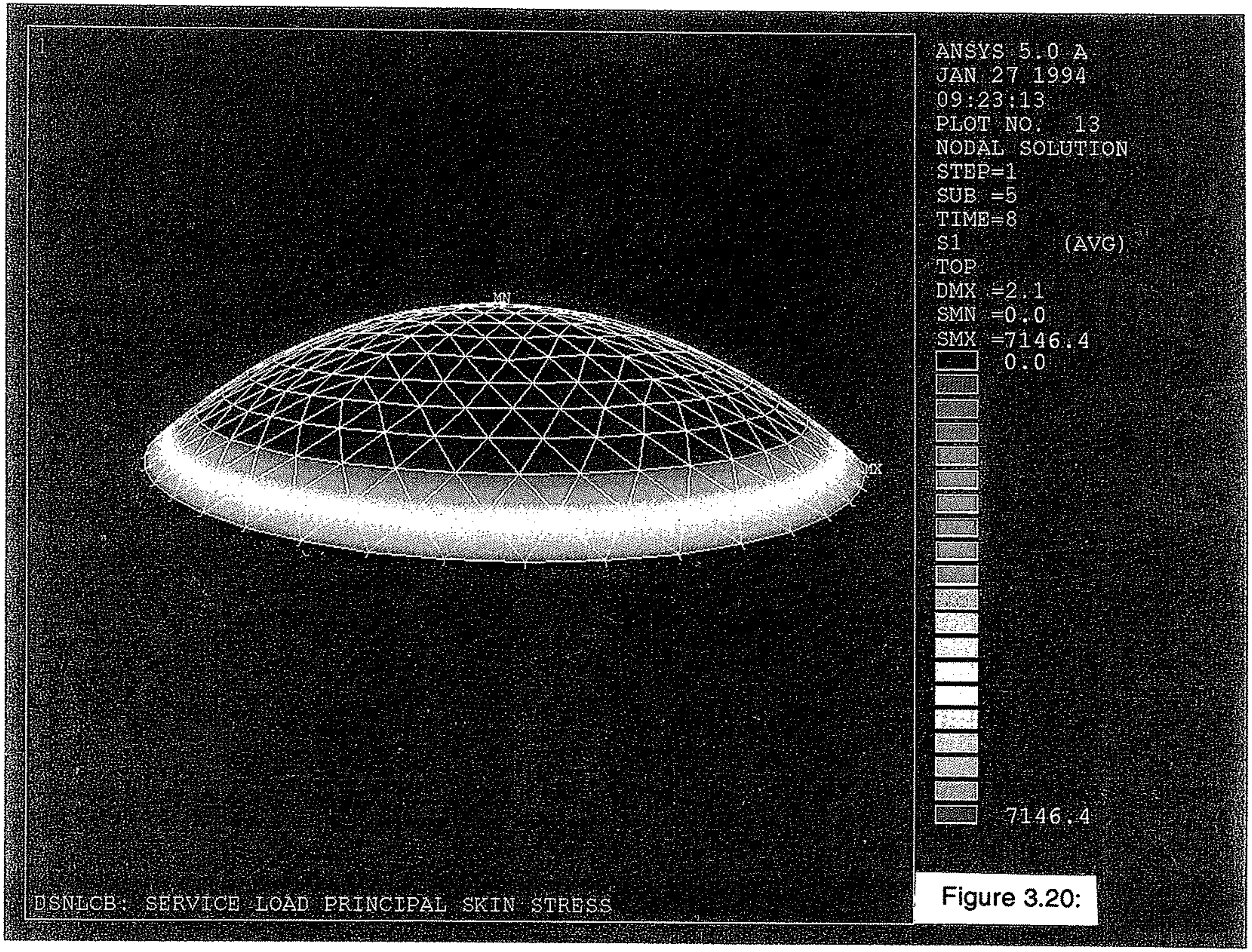
1
MN
MX
ANSYS 5.0 A
JAN 27 1994
09:23:13
PLOT NO. 13
NODAL SOLUTION
STEP=1
SUB =5
TIME=8
S1 (AVG)
TOP
DMX =2.1
SMN =0.0
SMX =7146.4
0.0
7146.4
DSNLCB: SERVICE LOAD PRINCIPAL SKIN STRESS

Figure 3.20:

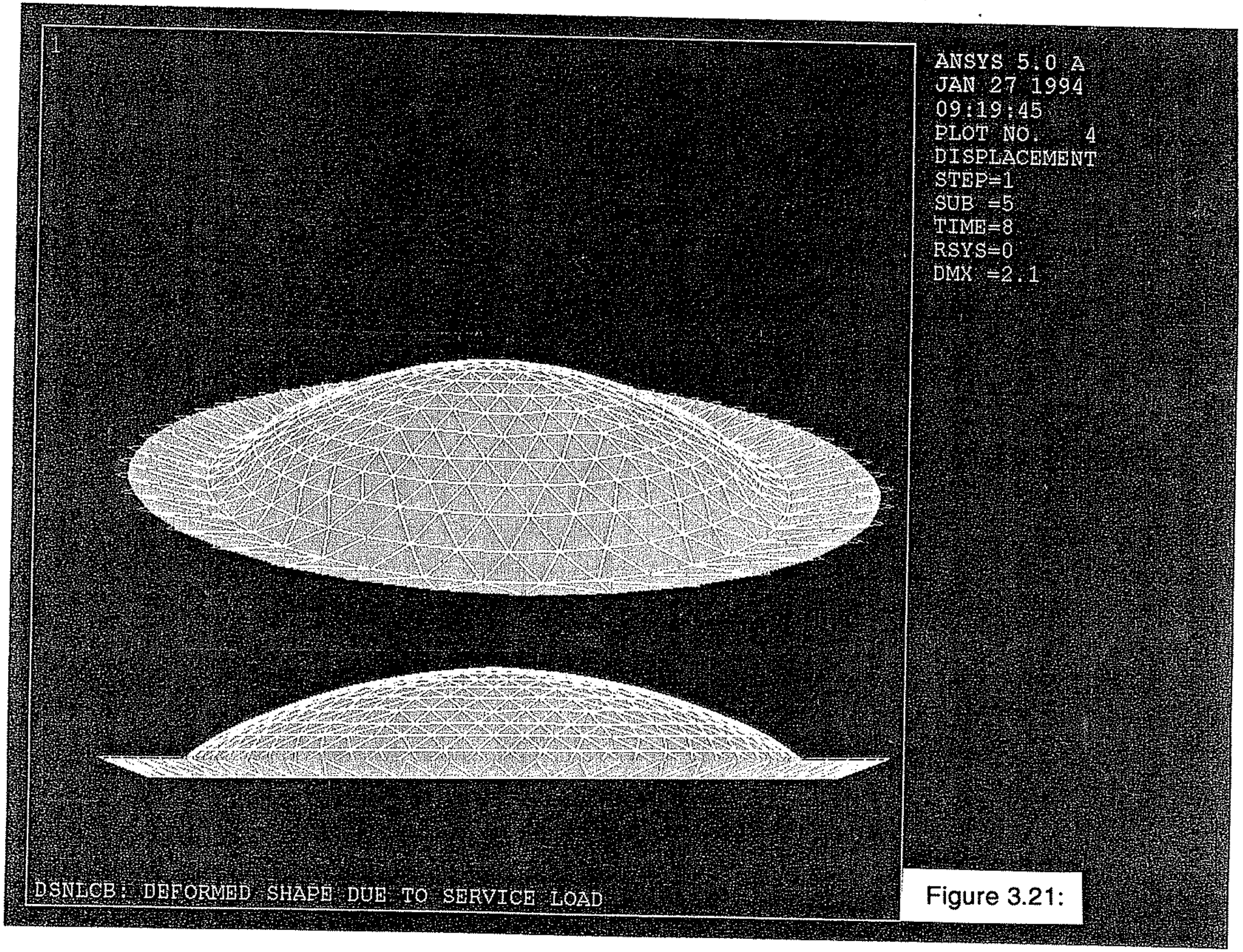
1
ANSYS 5.0 A
JAN 27 1994
09:19:45
PLOT NO. 4
DISPLACEMENT
STEP=1
SUB =5
TIME=8
RSYS=0
DMX =2.1
DSNLCB: DEFORMED SHAPE DUE TO SERVICE LOAD

Figure 3.21:

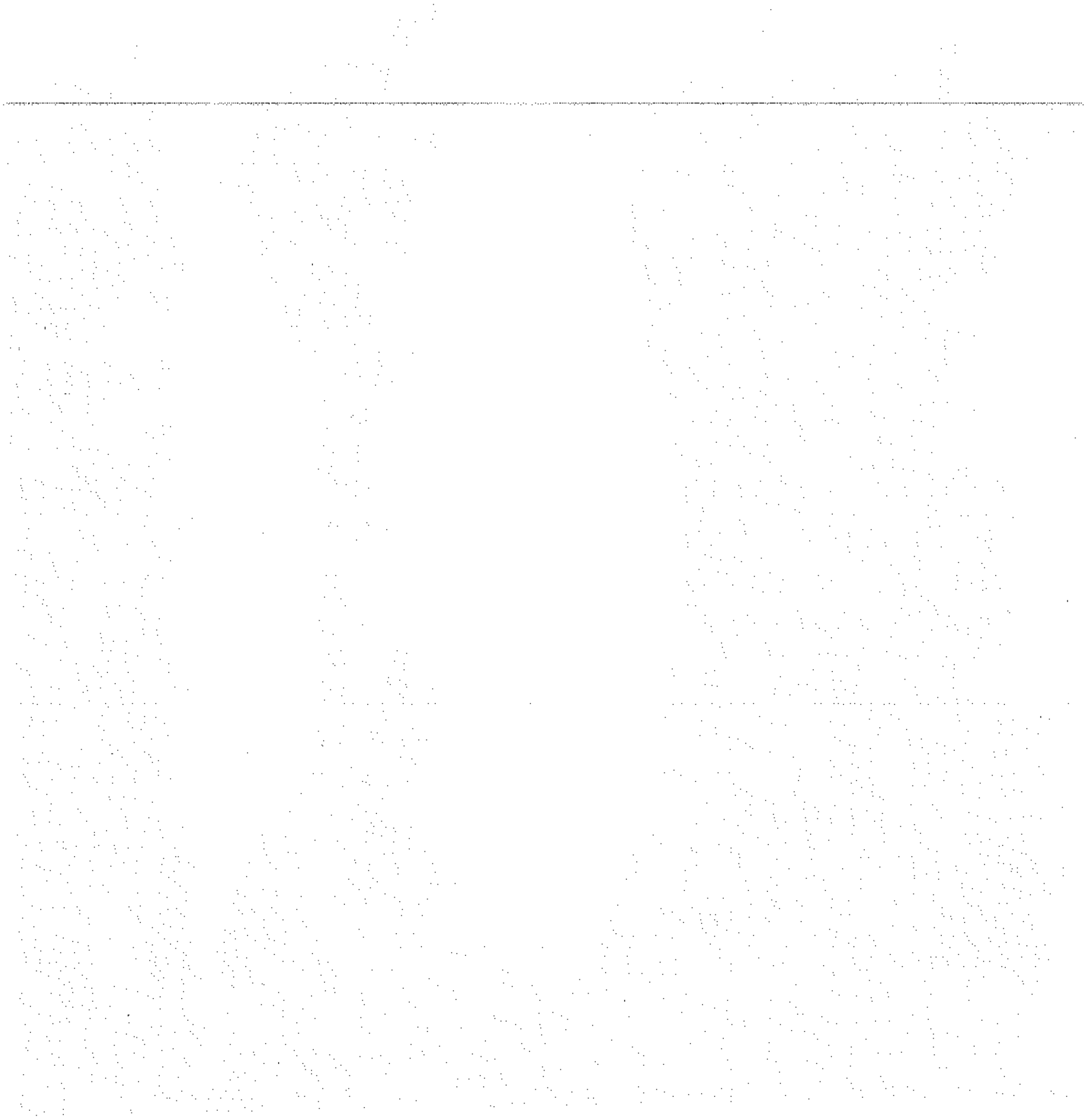

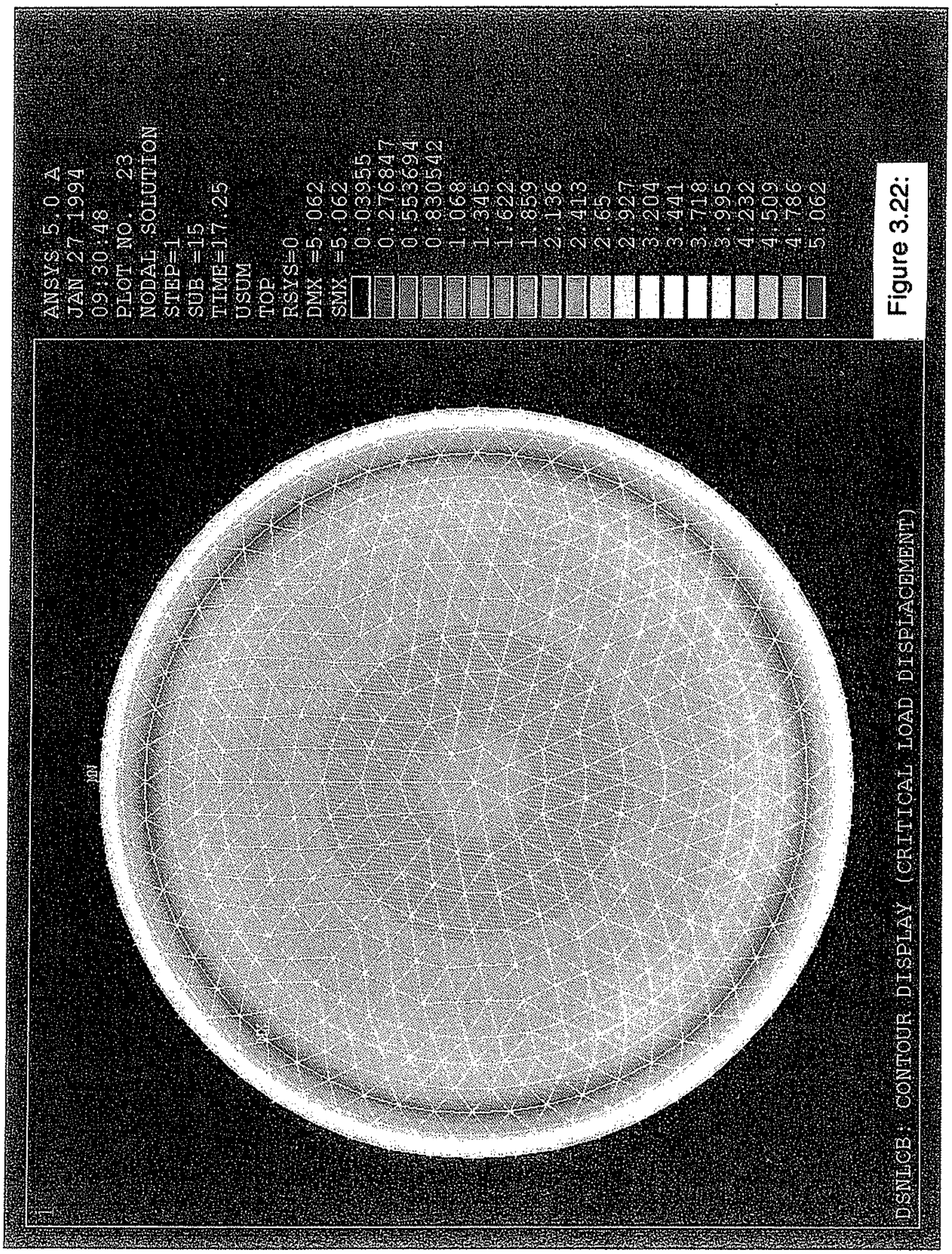
ANSYS 5.0 A
JAN 27 1994
09:30:48
PLOT NO. 23
NODAL SOLUTION
STEP=1
SUB =15
TIME=17.25
USUM
TOP
RSYS=0
DMX =5.062
SMX =5.062
0.03955
0.276847
0.553694
0.830542
1.068
1.345
1.622
1.859
2.136
2.413
2.65
2.927
3.204
3.441
3.718
3.995
4.232
4.509
4.786
5.062
DSNLCB: CONTOUR DISPLAY (CRITICAL LOAD DISPLACEMENT)

Figure 3.22:

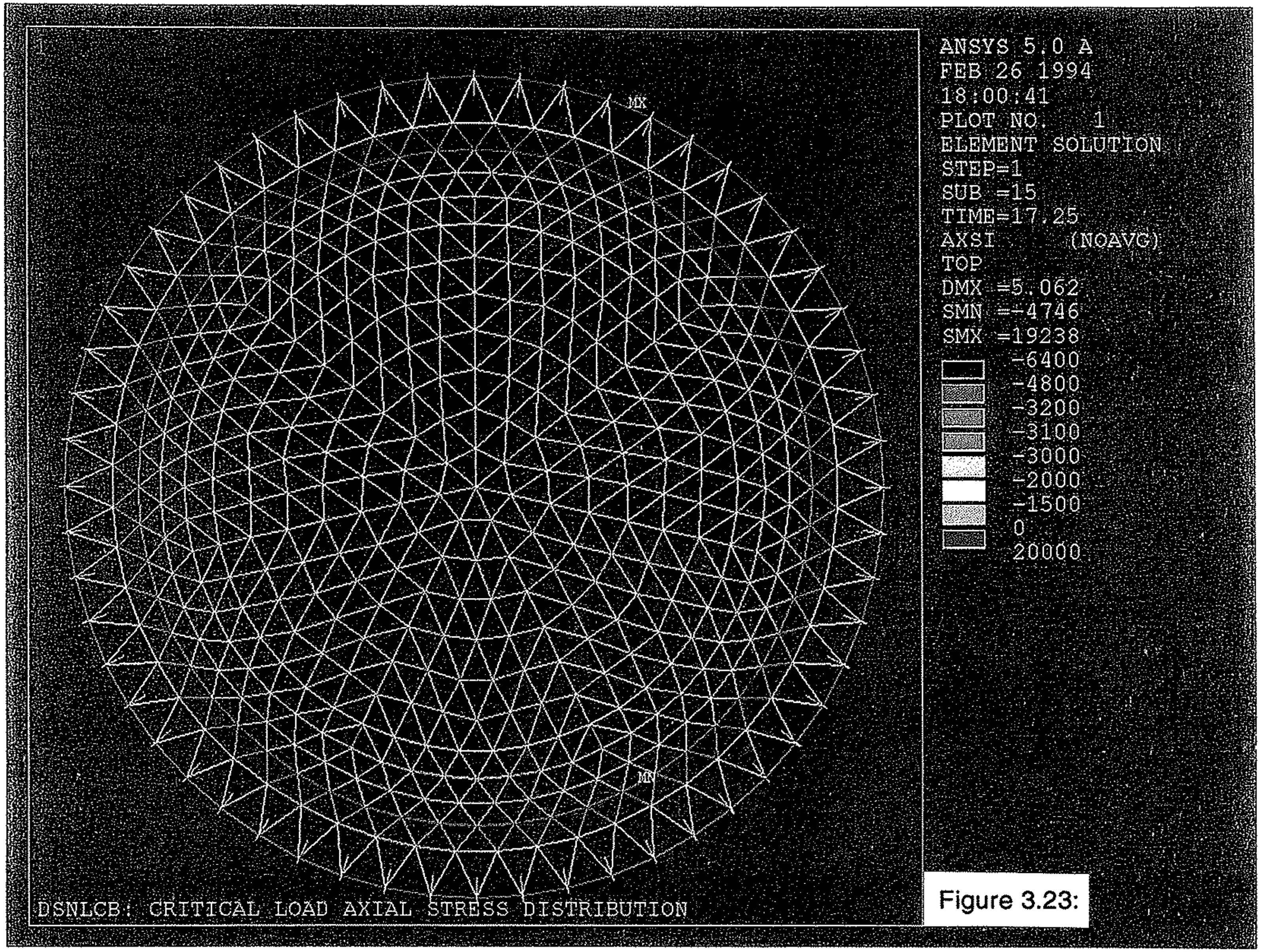
ANSYS 5.0 A
FEB 26 1994
18:00:41
PLOT NO. 1
ELEMENT SOLUTION
STEP=1
SUB =15
TIME=17.25
AXSI (NOAVG)
TOP
DMX =5.062
SMN =-4746
SMX =19238
-6400
-4800
-3200
-3100
-3000
-2000
-1500
0
20000
MX
MN
1
DSNLCB: CRITICAL LOAD AXIAL STRESS DISTRIBUTION

Figure 3.23:

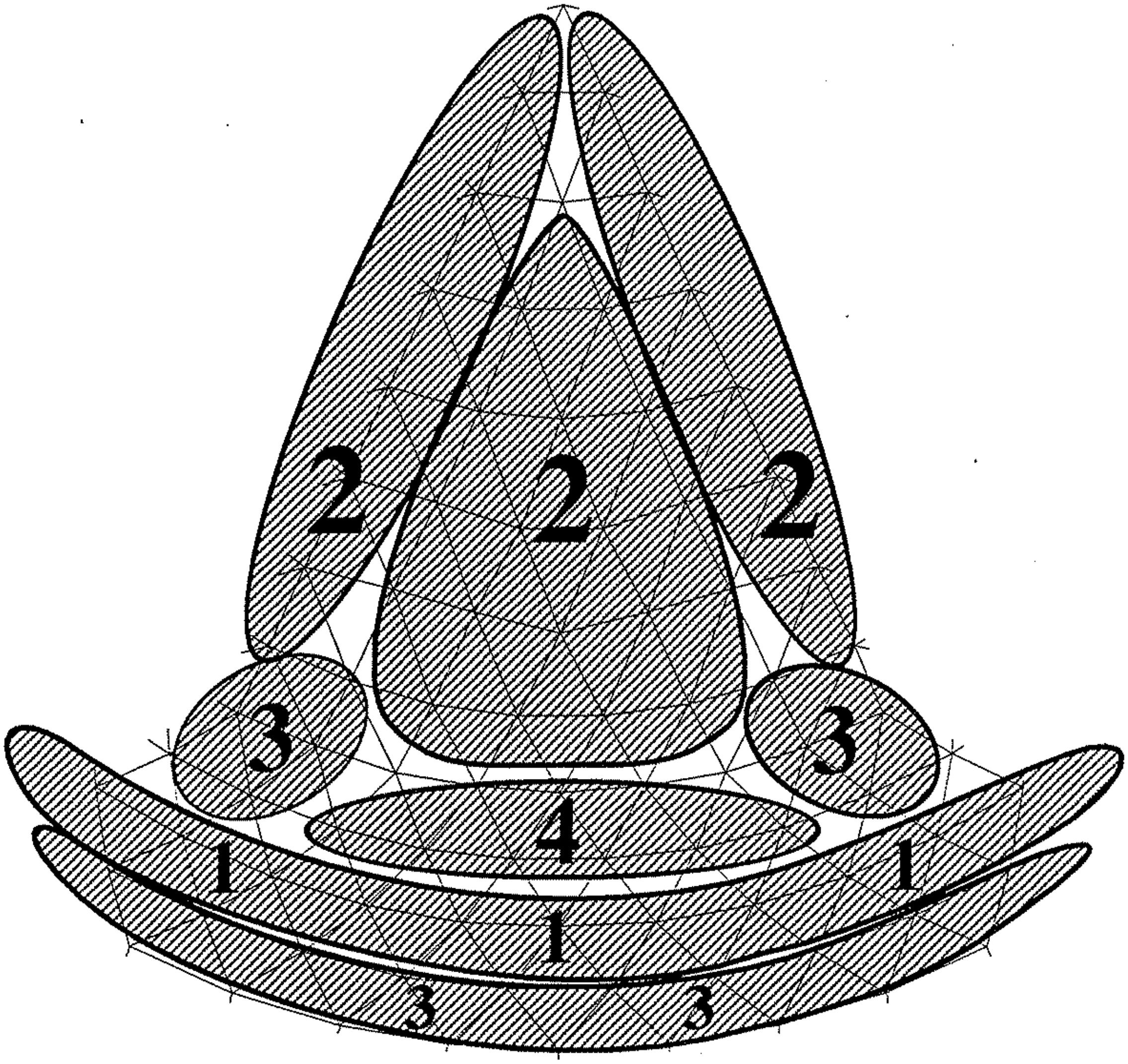

Max Comp (1) Third bottom ring & adjacent lower diagonals

↕ **(2) Seams & interslice regions**

(3) Lower seam diagonals, Second bottom ring, & Lower diagonals

Min Comp (4) Transition ring

Figure 3.24: DSNLCB Compressive Axial Stress Distribution (Critical Load)

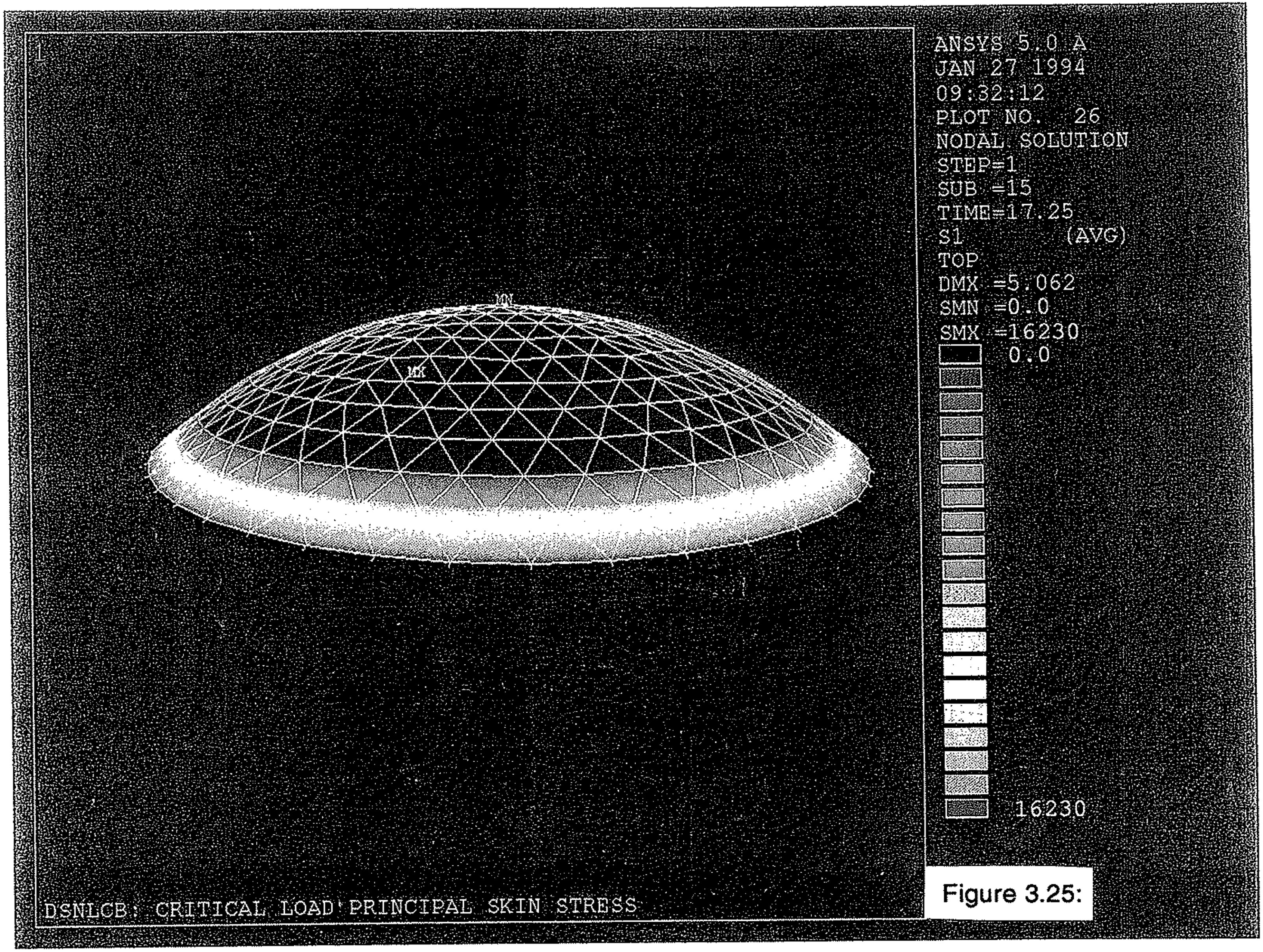
1
ANSYS 5.0 A
JAN 27 1994
09:32:12
PLOT NO. 26
NODAL SOLUTION
STEP=1
SUB =15
TIME=17.25
S1 (AVG)
TOP
DMX =5.062
SMN =0.0
SMX =16230
0.0
16230
MN
MX
DSNLCB: CRITICAL LOAD PRINCIPAL SKIN STRESS

Figure 3.25:

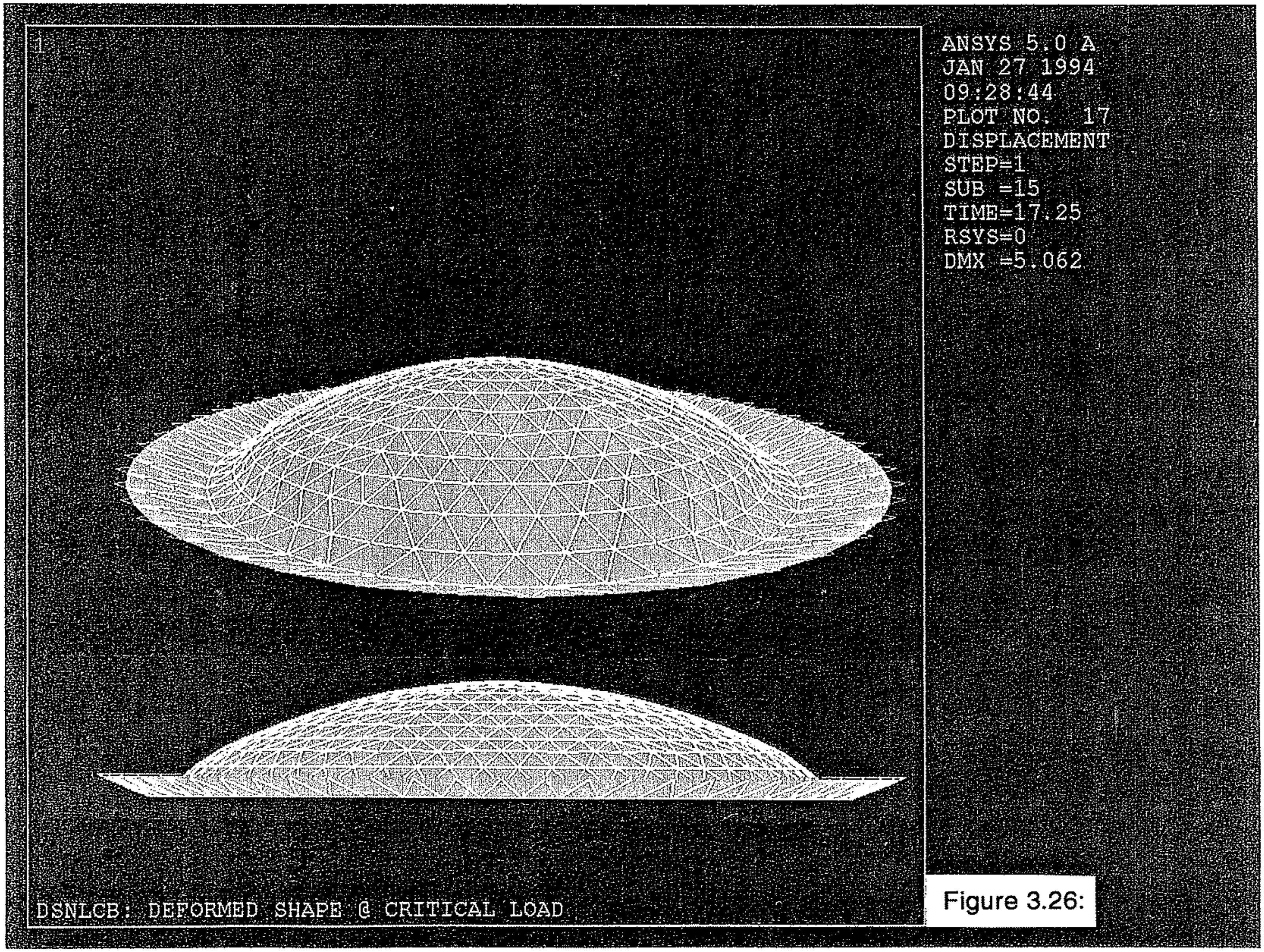
1
ANSYS 5.0 A
JAN 27 1994
09:28:44
PLOT NO. 17
DISPLACEMENT
STEP=1
SUB =15
TIME=17.25
RSYS=0
DMX =5.062
DSNLCB: DEFORMED SHAPE @ CRITICAL LOAD

Figure 3.26:

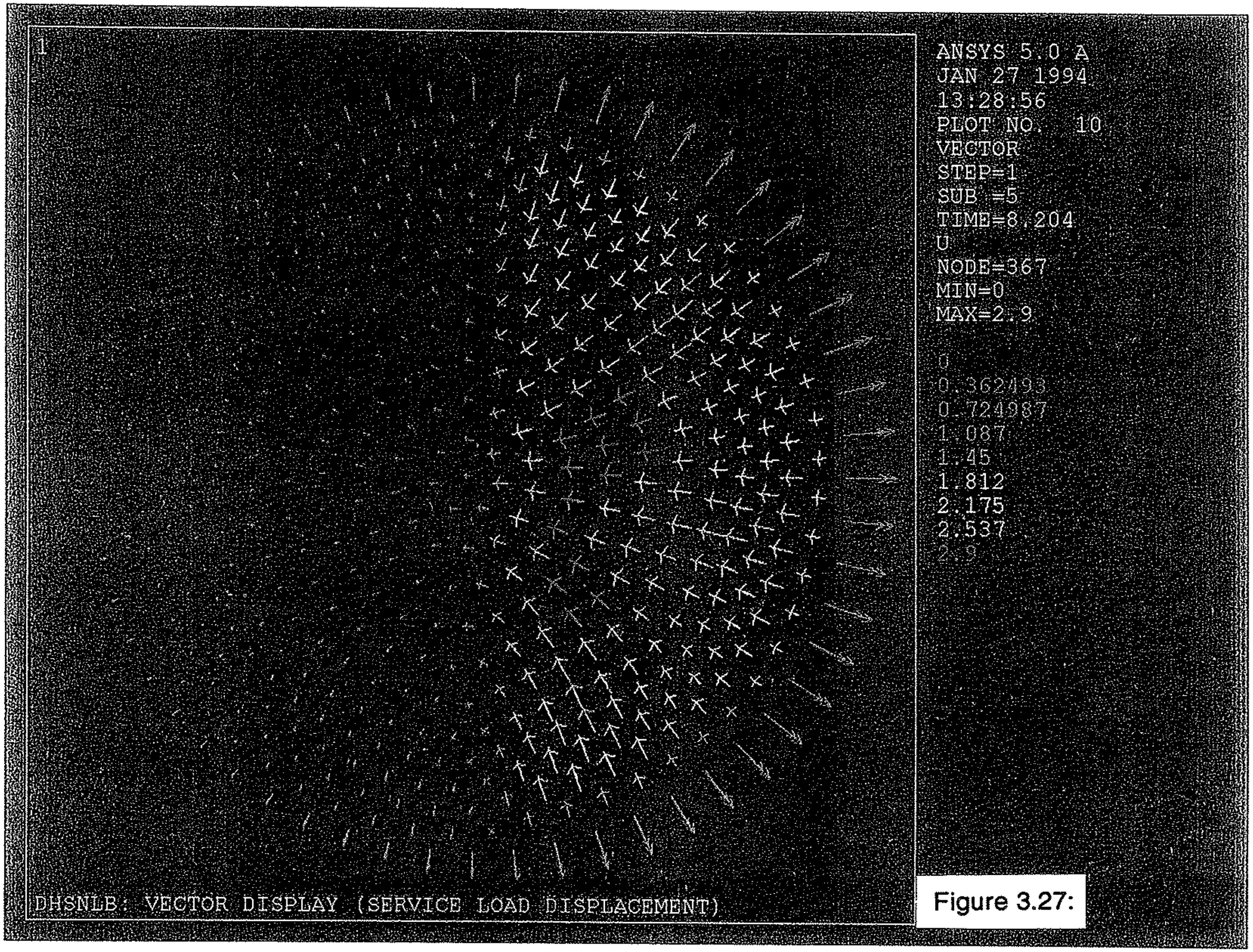
1
ANSYS 5.0 A
JAN 27 1994
13:28:56
PLOT NO. 10
VECTOR
STEP=1
SUB =5
TIME=8.204
U
NODE=367
MIN=0
MAX=2.9
0
0.362493
0.724987
1.087
1.45
1.812
2.175
2.537
2.9
DHSNLB: VECTOR DISPLAY (SERVICE LOAD DISPLACEMENT)

Figure 3.27:

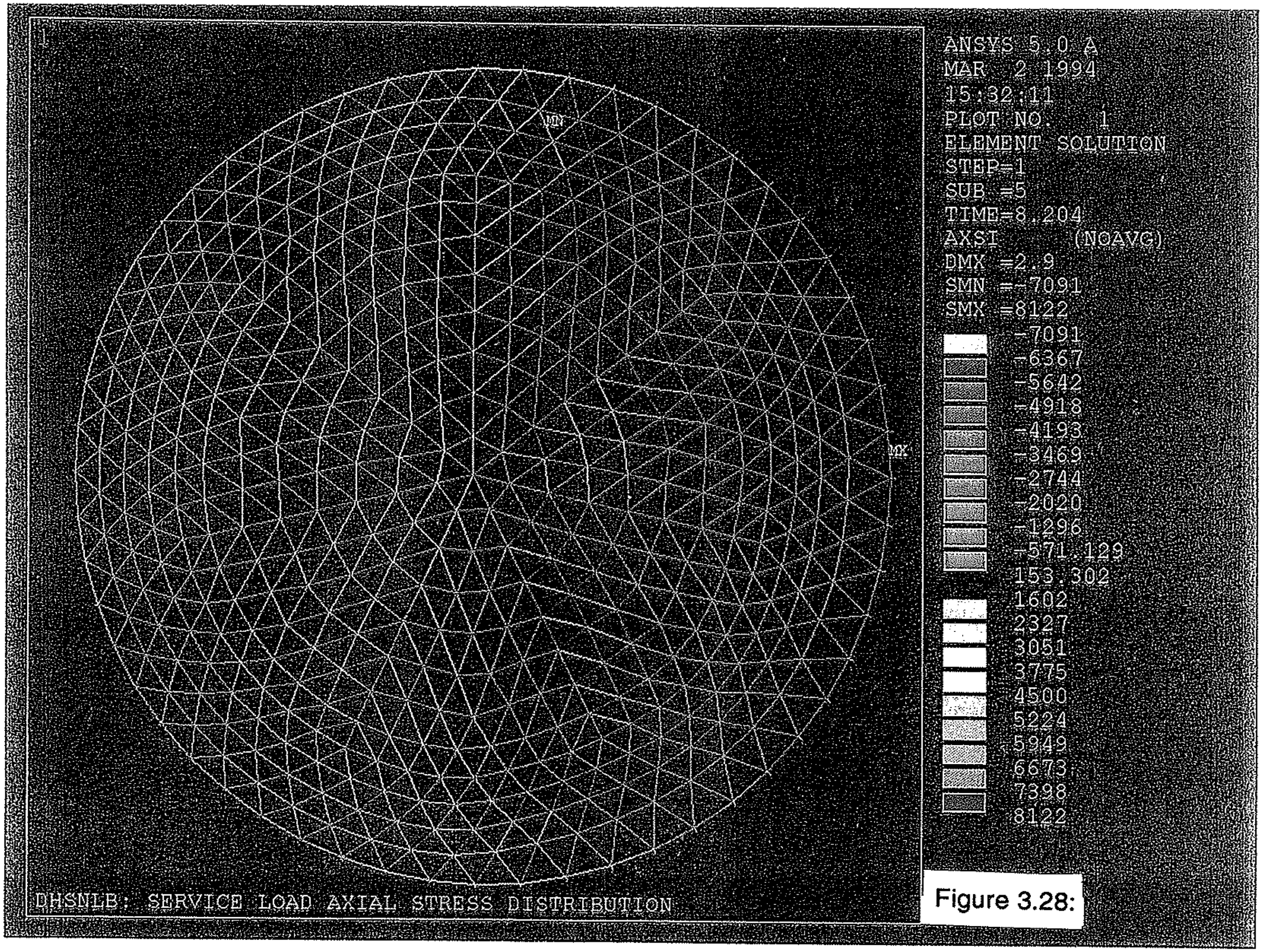
ANSYS 5.0 A
MAR 2 1994
15:32:11
PLOT NO. 1
ELEMENT SOLUTION
STEP=1
SUB =5
TIME=8.204
AXSI (NOAVG)
DMX =2.9
SMN =-7091
SMX =8122
-7091
-6367
-5642
-4918
-4193
-3469
-2744
-2020
-1296
-571.129
153.302
1602
2327
3051
3775
4500
5224
5949
6673
7398
8122
MN
MX
1
DHSNLB: SERVICE LOAD AXIAL STRESS DISTRIBUTION

Figure 3.28:

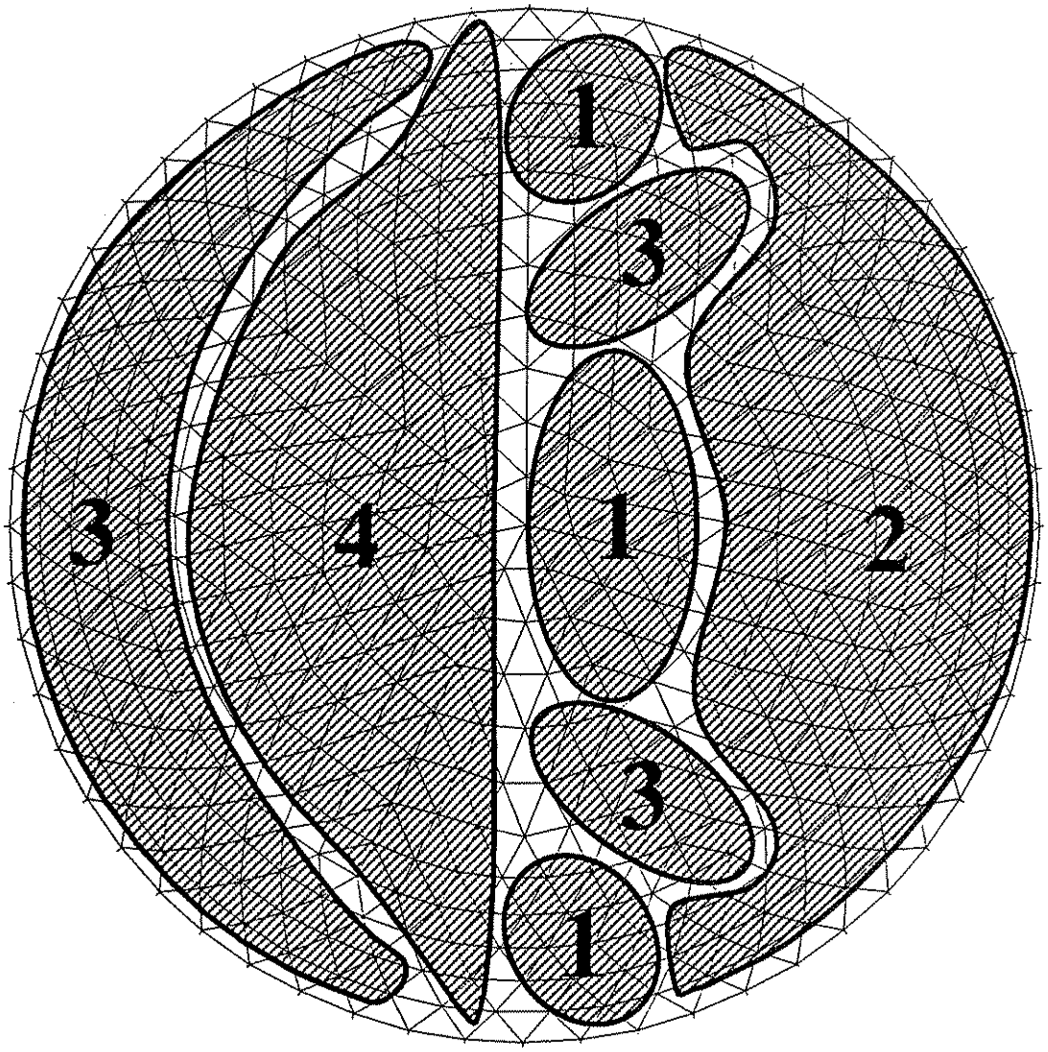

Comp (1) Transition diagonals near N & S ends, East upper rings

↕ (2) Seams, Interslice regions, Lower rings & diagonals

~0 (3) "Negligible" stress regions

↕ (4) Upper segment of unloaded surface

Max Tens Base Tension Ring

Figure 3.29: DHSNLB Axial Stress Distribution (Service Load)

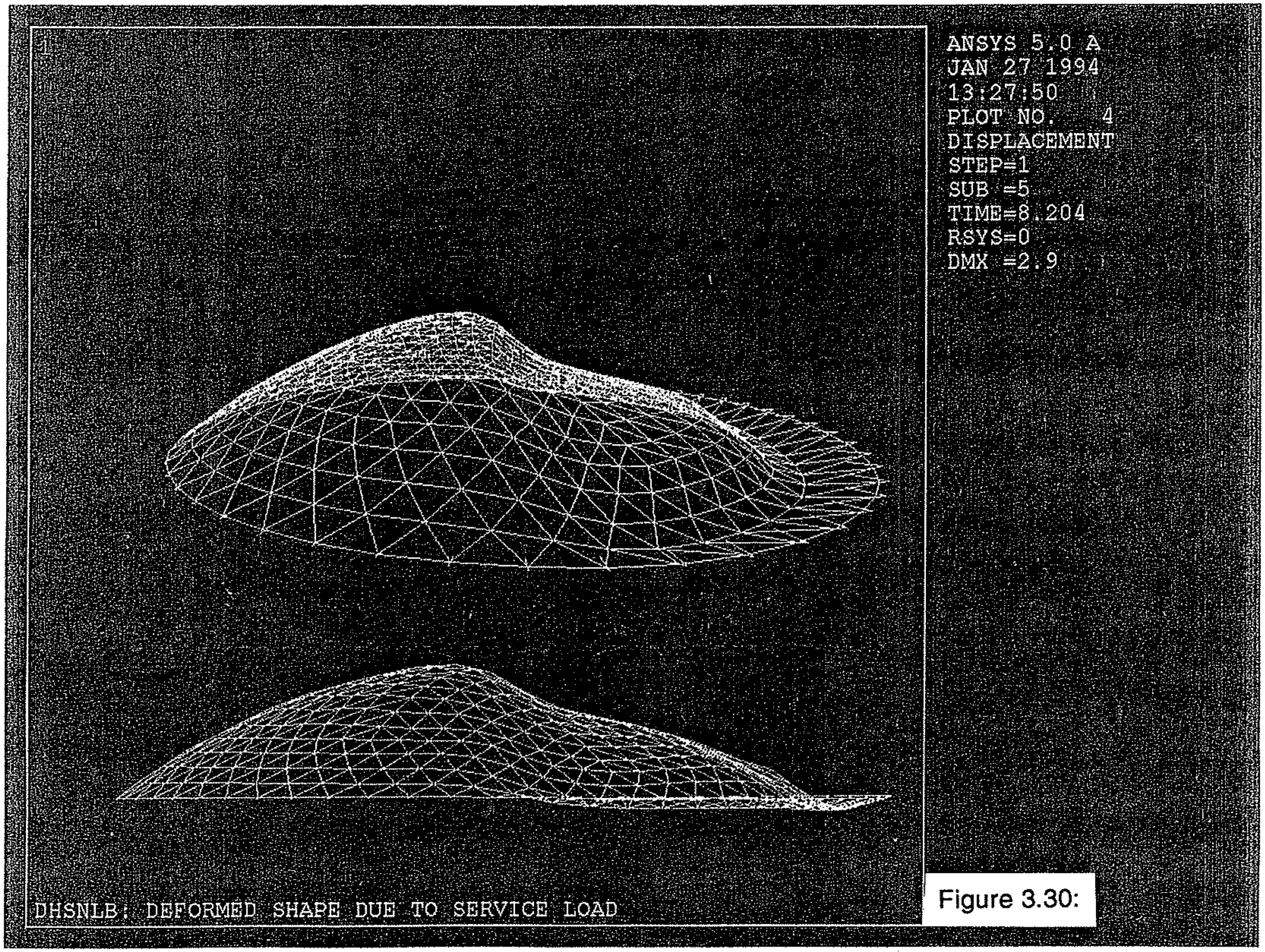
ANSYS 5.0 A
JAN 27 1994
13:27:50
PLOT NO. 4
DISPLACEMENT
STEP=1
SUB =5
TIME=8.204
RSYS=0
DMX =2.9
1
DHSNLB: DEFORMED SHAPE DUE TO SERVICE LOAD

Figure 3.30:

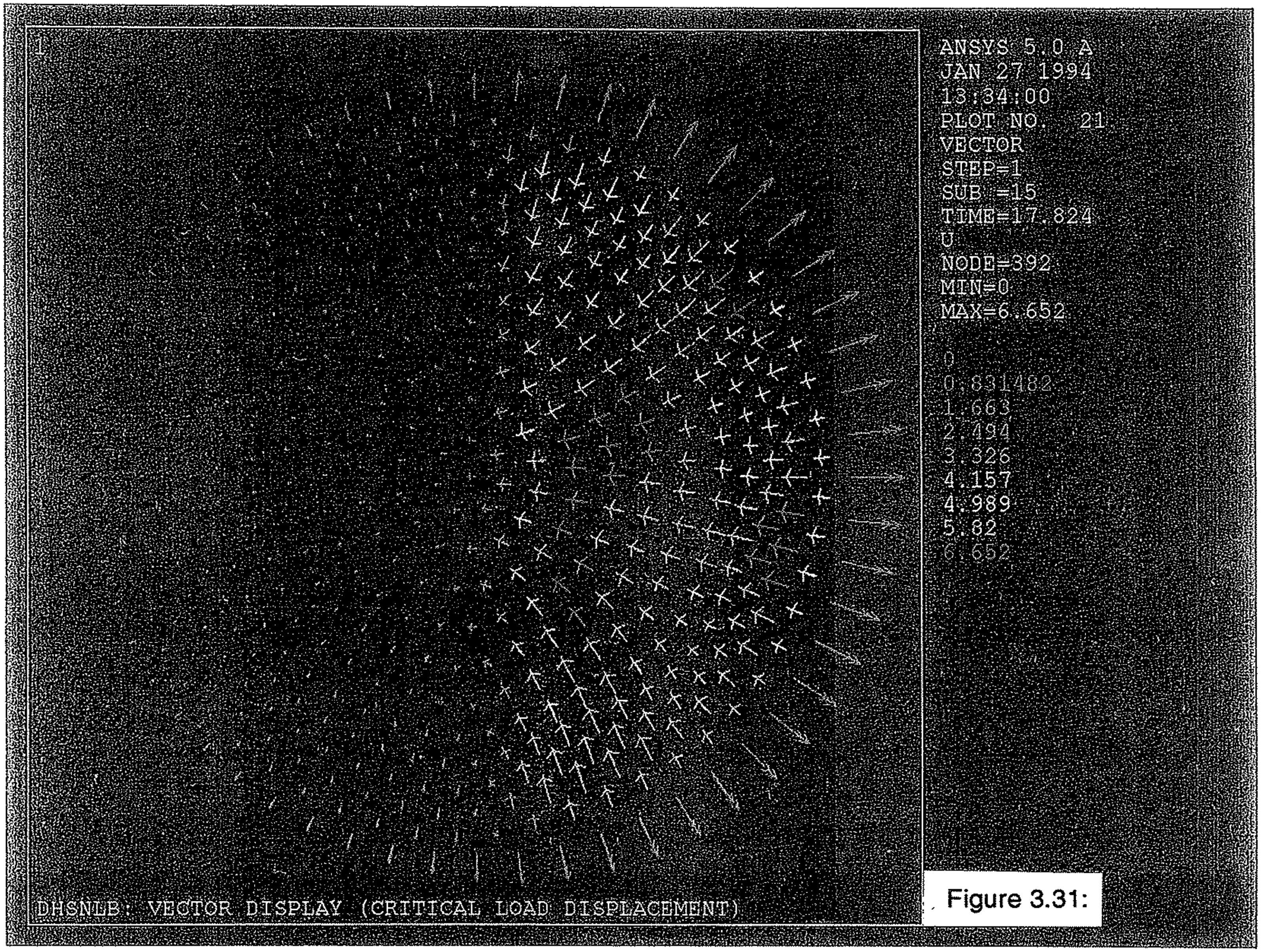
1
ANSYS 5.0 A
JAN 27 1994
13:34:00
PLOT NO. 21
VECTOR
STEP=1
SUB =15
TIME=17.824
U
NODE=392
MIN=0
MAX=6.652
0
0.831482
1.663
2.494
3.326
4.157
4.989
5.82
6.652
DHSNLB: VECTOR DISPLAY (CRITICAL LOAD DISPLACEMENT)

Figure 3.31:

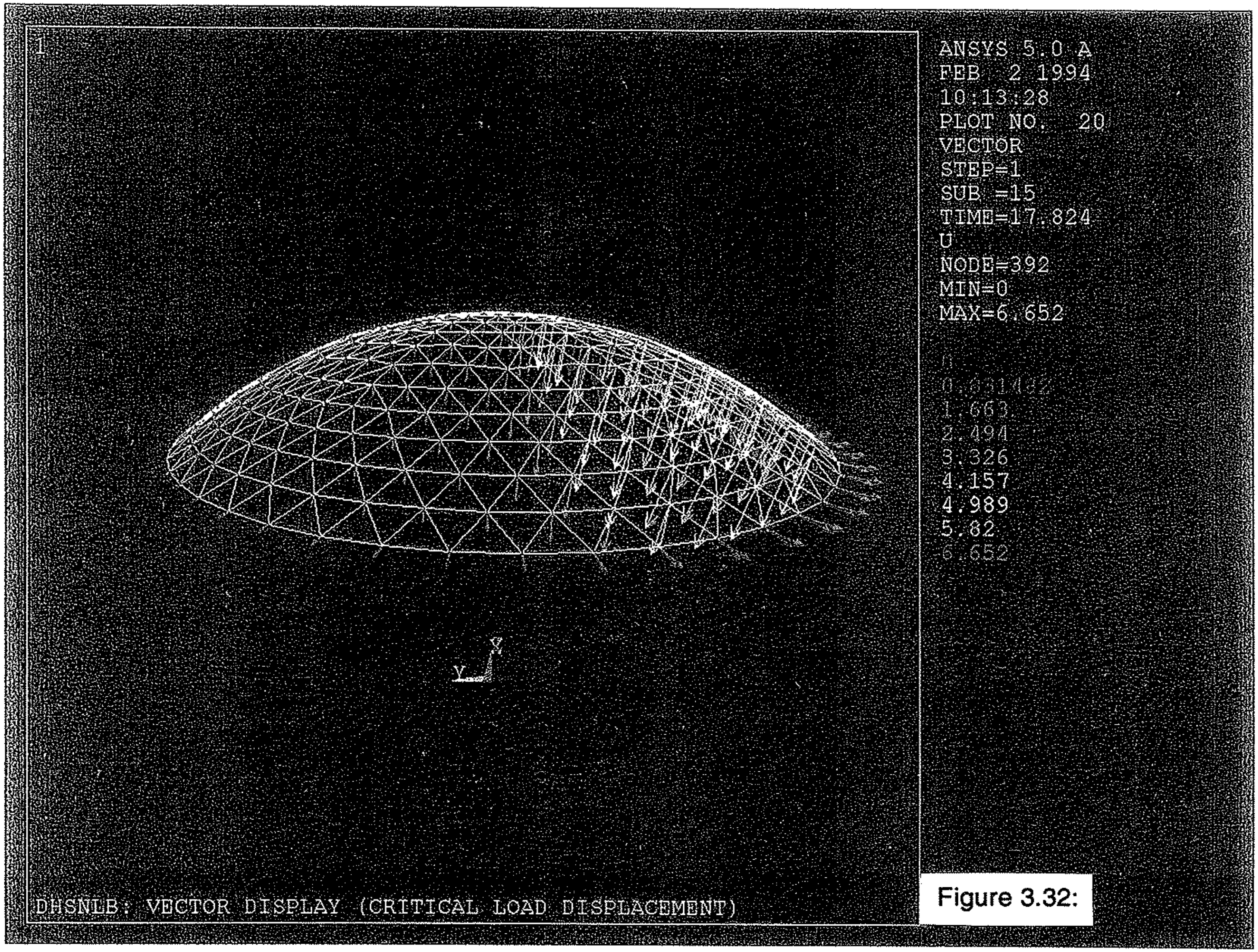
1
ANSYS 5.0 A
FEB 2 1994
10:13:28
PLOT NO. 20
VECTOR
STEP=1
SUB =15
TIME=17.824
U
NODE=392
MIN=0
MAX=6.652
0
0.831482
1.663
2.494
3.326
4.157
4.989
5.82
6.652
Y
X
DHSNLB: VECTOR DISPLAY (CRITICAL LOAD DISPLACEMENT)

Figure 3.32:

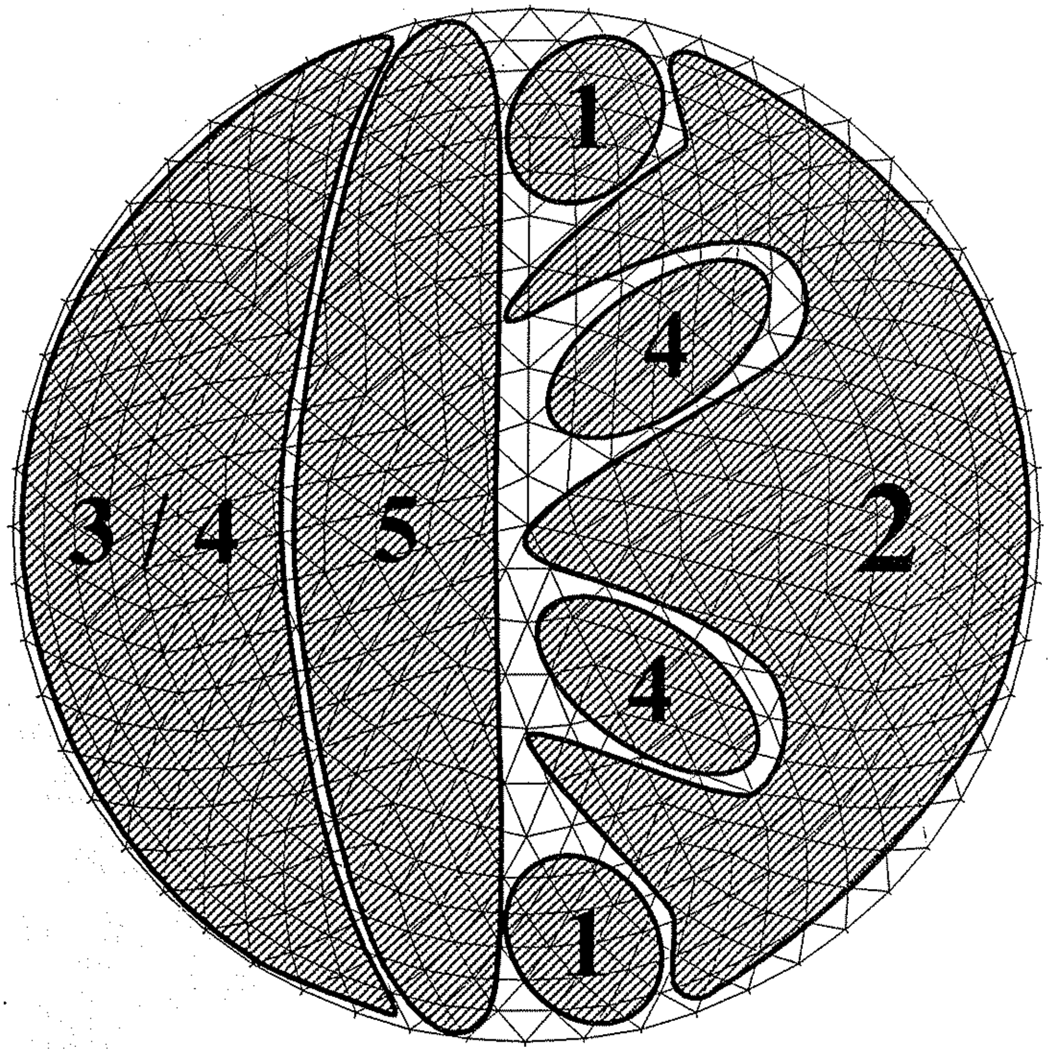

Max Comp (1) Transition diagonals near N & S ends

(2) Majority of loaded face excl. lower base ring & outer seam diags

(3) "Negligible" comp: Lower/midheight seams & diags

~0 (4) "Negligible" tens: Lower/midheight rings, outer seam diags

(5) Upper N- S oriented struts on unloaded face

Max Tens Base Tension Ring

Figure 3.33: DHSNLB Axial Stress Distribution (Critical Load)

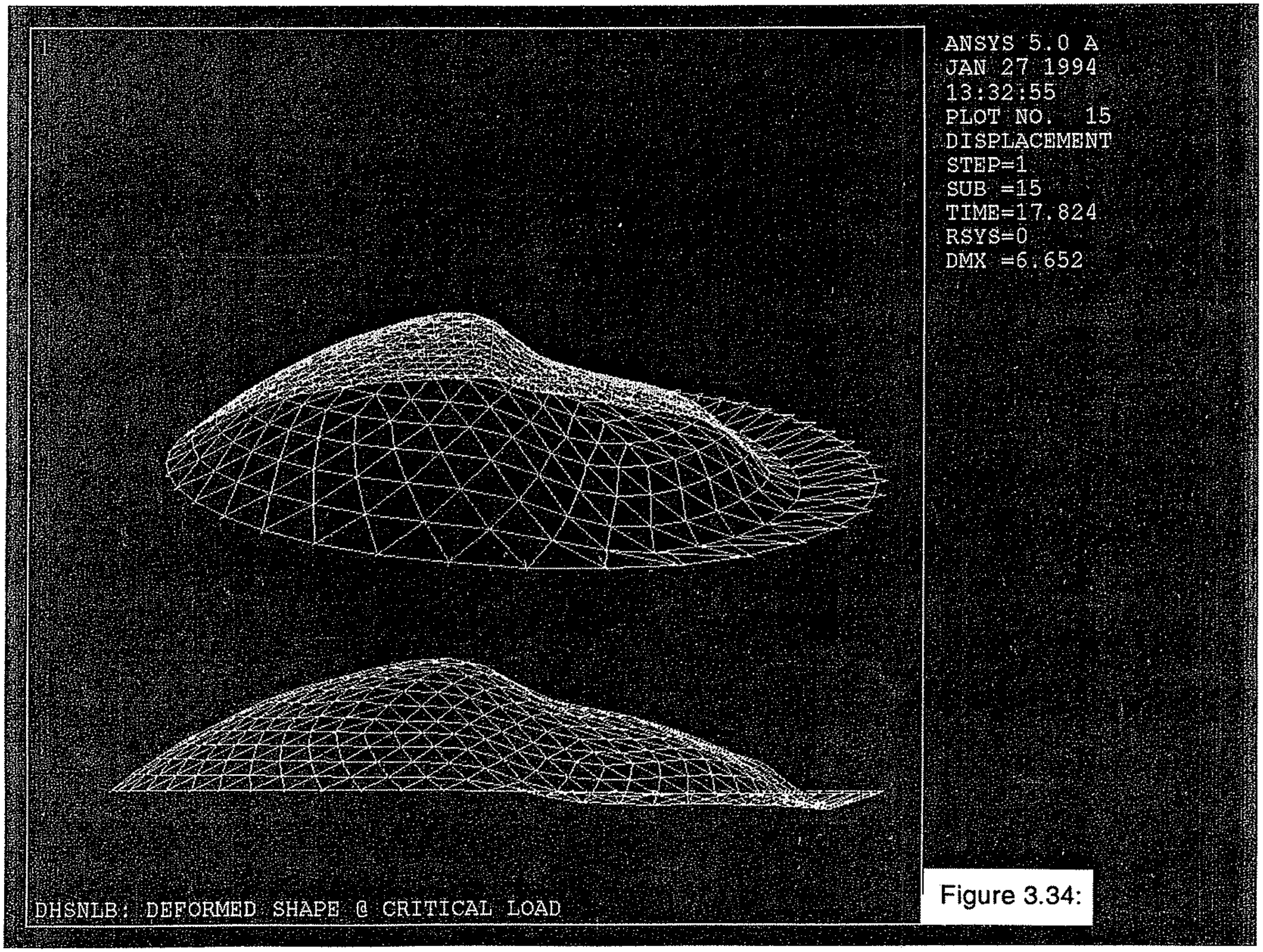
1
ANSYS 5.0 A
JAN 27 1994
13:32:55
PLOT NO. 15
DISPLACEMENT
STEP=1
SUB =15
TIME=17.824
RSYS=0
DMX =6.652
DHSNLB: DEFORMED SHAPE @ CRITICAL LOAD

Figure 3.34:

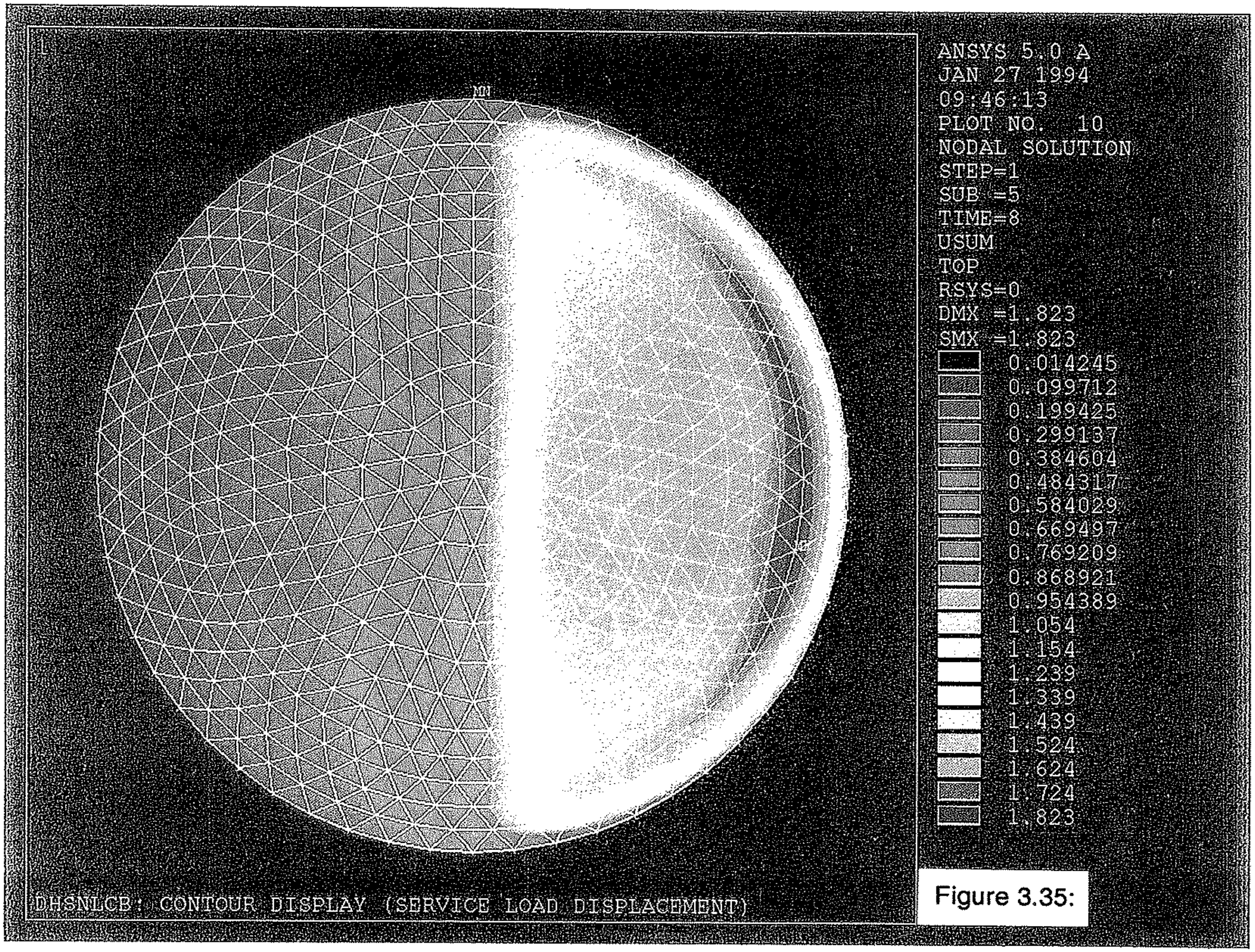
ANSYS 5.0 A
JAN 27 1994
09:46:13
PLOT NO. 10
NODAL SOLUTION
STEP=1
SUB =5
TIME=8
USUM
TOP
RSYS=0
DMX =1.823
SMX =1.823
0.014245
0.099712
0.199425
0.299137
0.384604
0.484317
0.584029
0.669497
0.769209
0.868921
0.954389
1.054
1.154
1.239
1.339
1.439
1.524
1.624
1.724
1.823
MN
MX
DHSNLCB: CONTOUR DISPLAY (SERVICE LOAD DISPLACEMENT)

Figure 3.35:

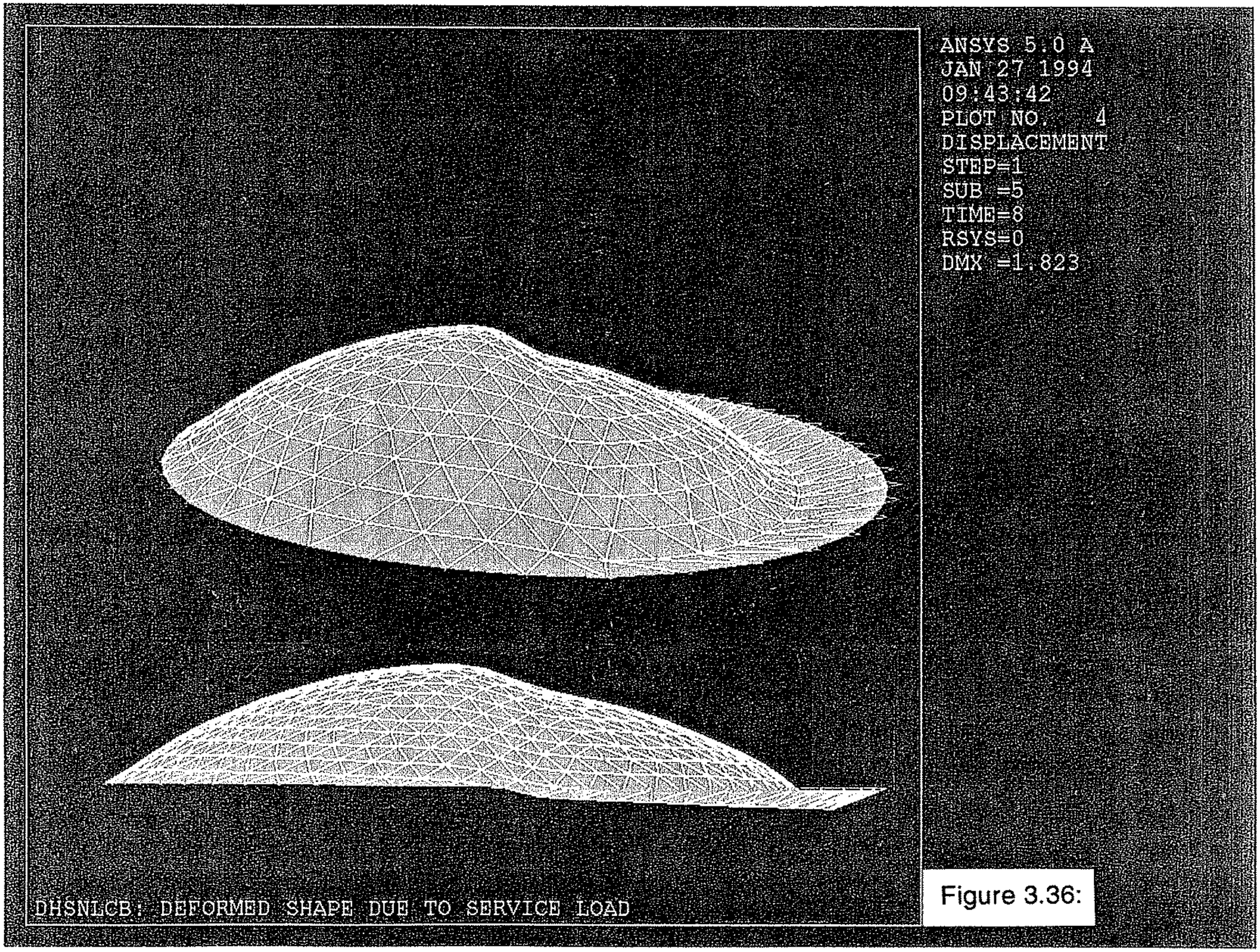

DHSNLCB: DEFORMED SHAPE DUE TO SERVICE LOAD

Figure 3.36:

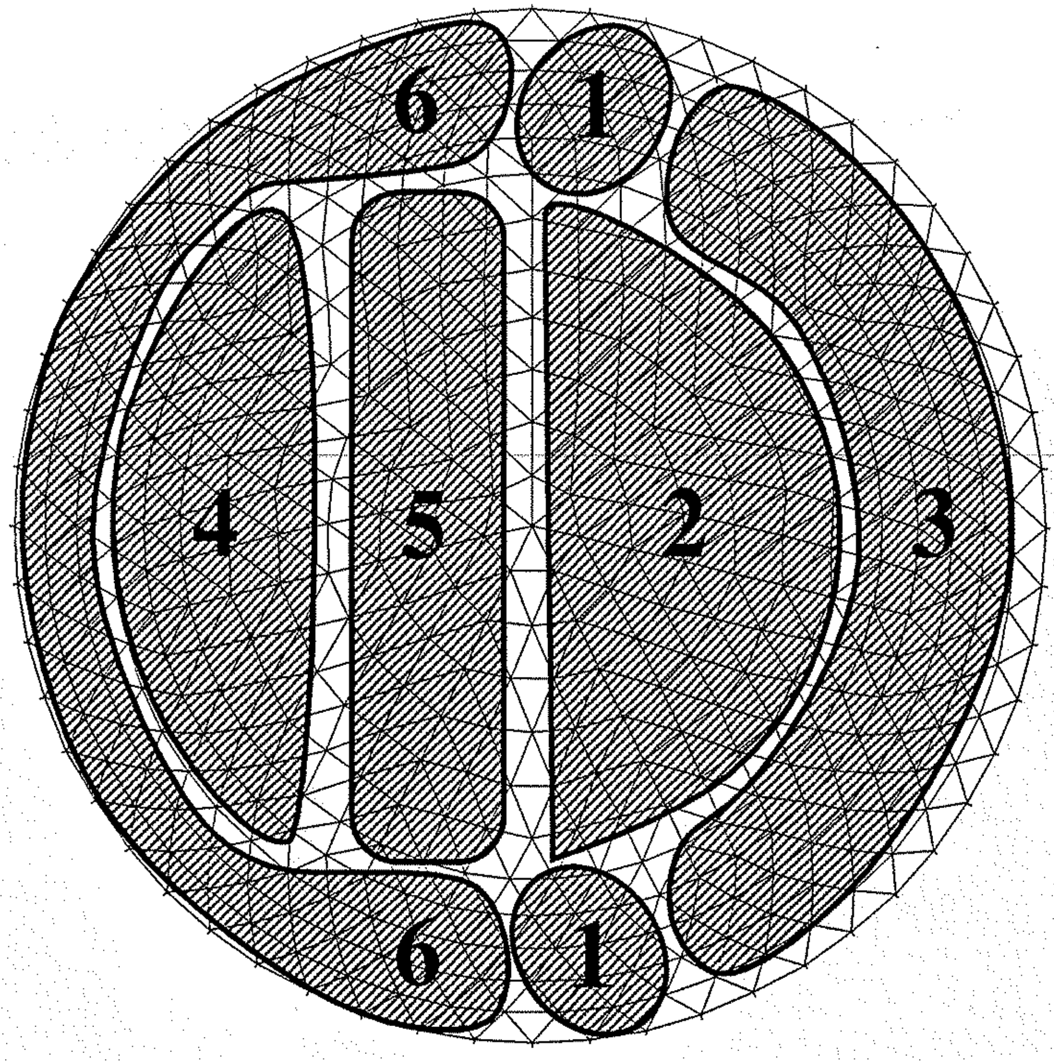

Comp

(1) Lower diagonals near N & S ends

(2) East face upper 1/2 ring segments

(3) Lower segment of loaded surface

(4) "Negligible" comp: Lower diags on unloaded surface

~0

(5) "Negligible" tens: N - S oriented upper diagonals

(6) N - S Diagonals leading into lower unloaded rings

Max Tens

Base Tension Ring

Figure 3.37: DHSNLCB Axial Stress Distribution (Service Load)

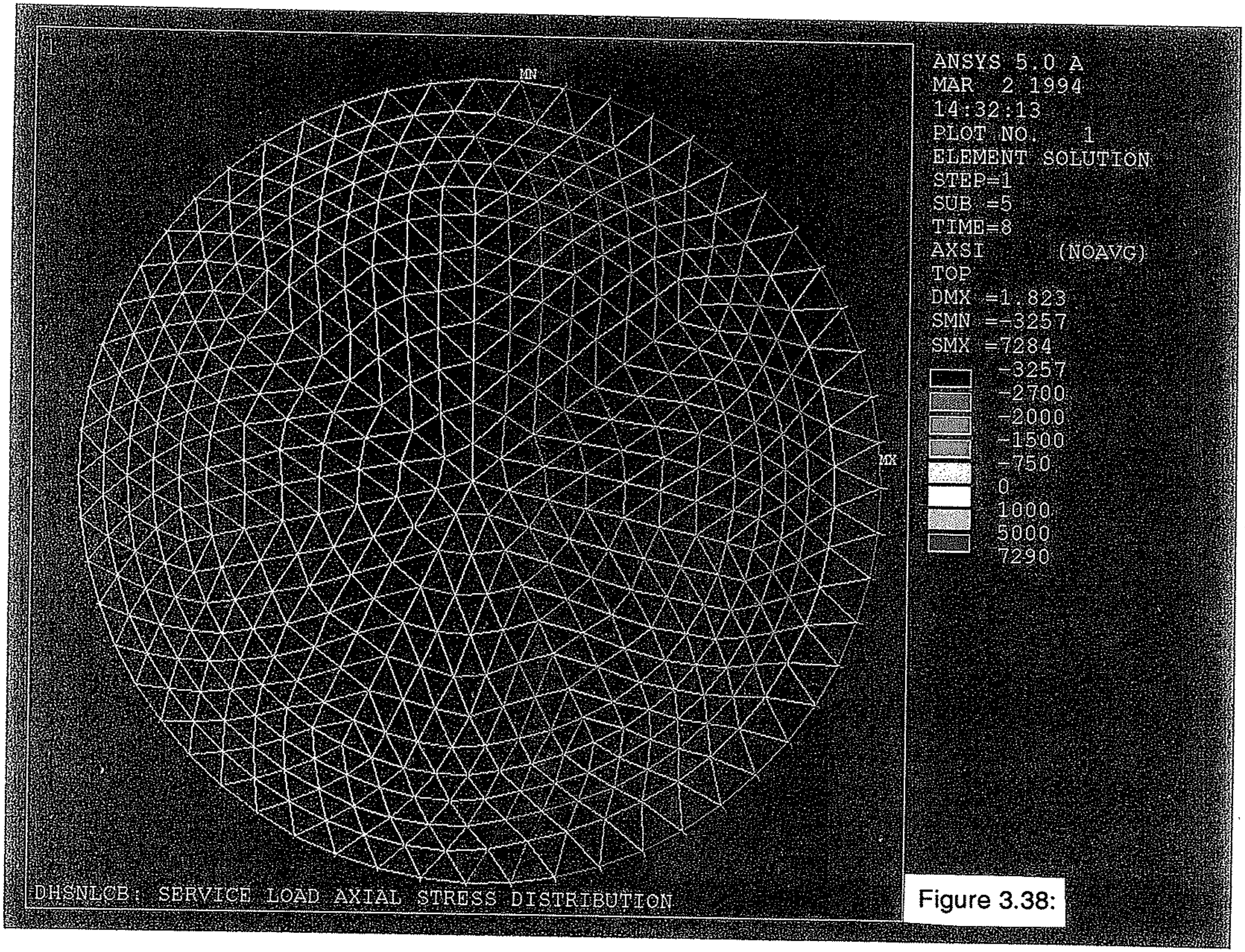
1
MN
MX
ANSYS 5.0 A
MAR 2 1994
14:32:13
PLOT NO. 1
ELEMENT SOLUTION
STEP=1
SUB =5
TIME=8
AXSI (NOAVG)
TOP
DMX =1.823
SMN =-3257
SMX =7284
-3257
-2700
-2000
-1500
-750
0
1000
5000
7290
DHSNLCB: SERVICE LOAD AXIAL STRESS DISTRIBUTION

Figure 3.38:

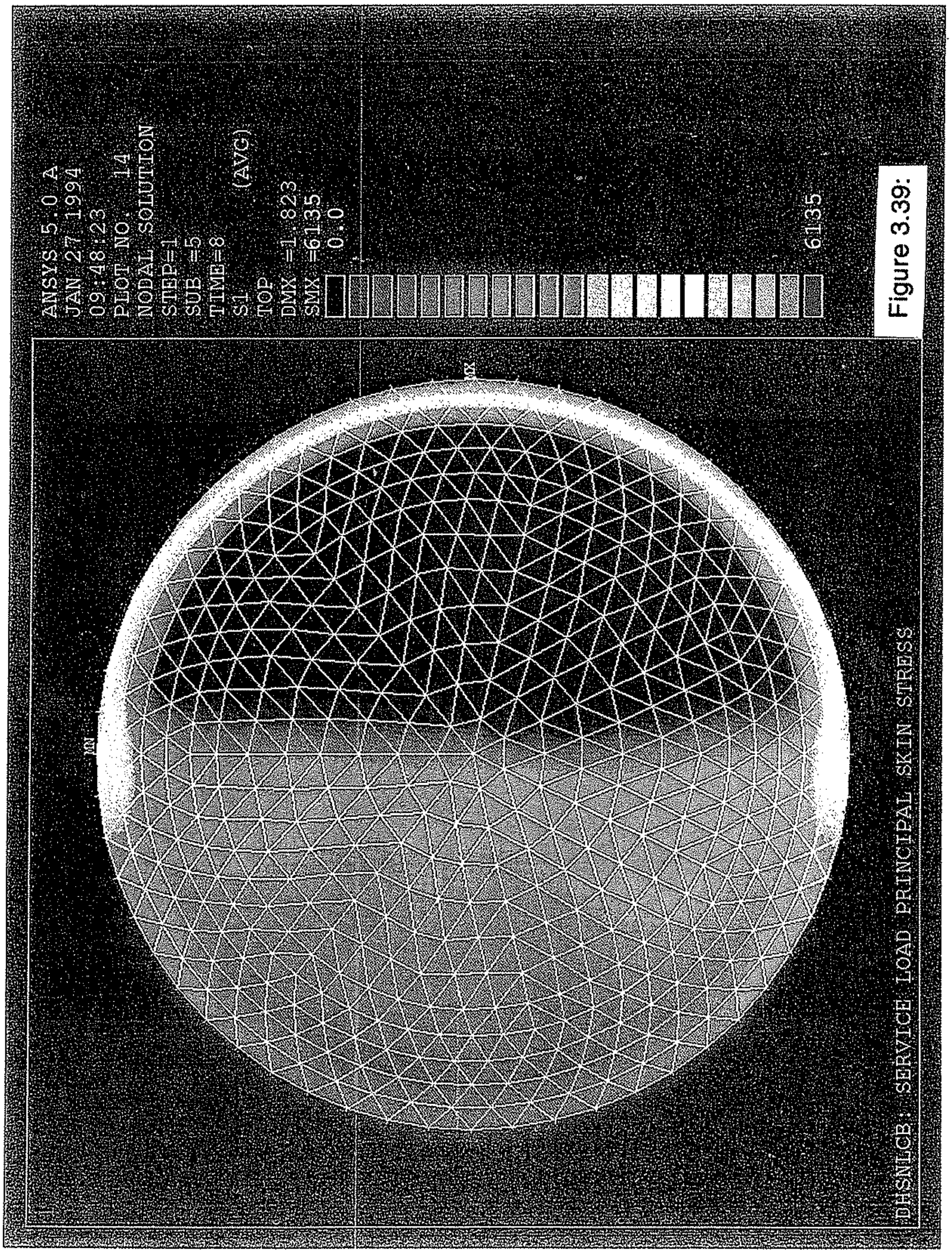
ANSYS 5.0 A
JAN 27 1994
09:48:23
PLOT NO. 14
NODAL SOLUTION
STEP=1
SUB =5
TIME=8
S1 (AVG)
TOP
DMX =1.823
SMX =6135
0.0
6135
MN
MX
DHSNLCB: SERVICE LOAD PRINCIPAL SKIN STRESS

Figure 3.39:

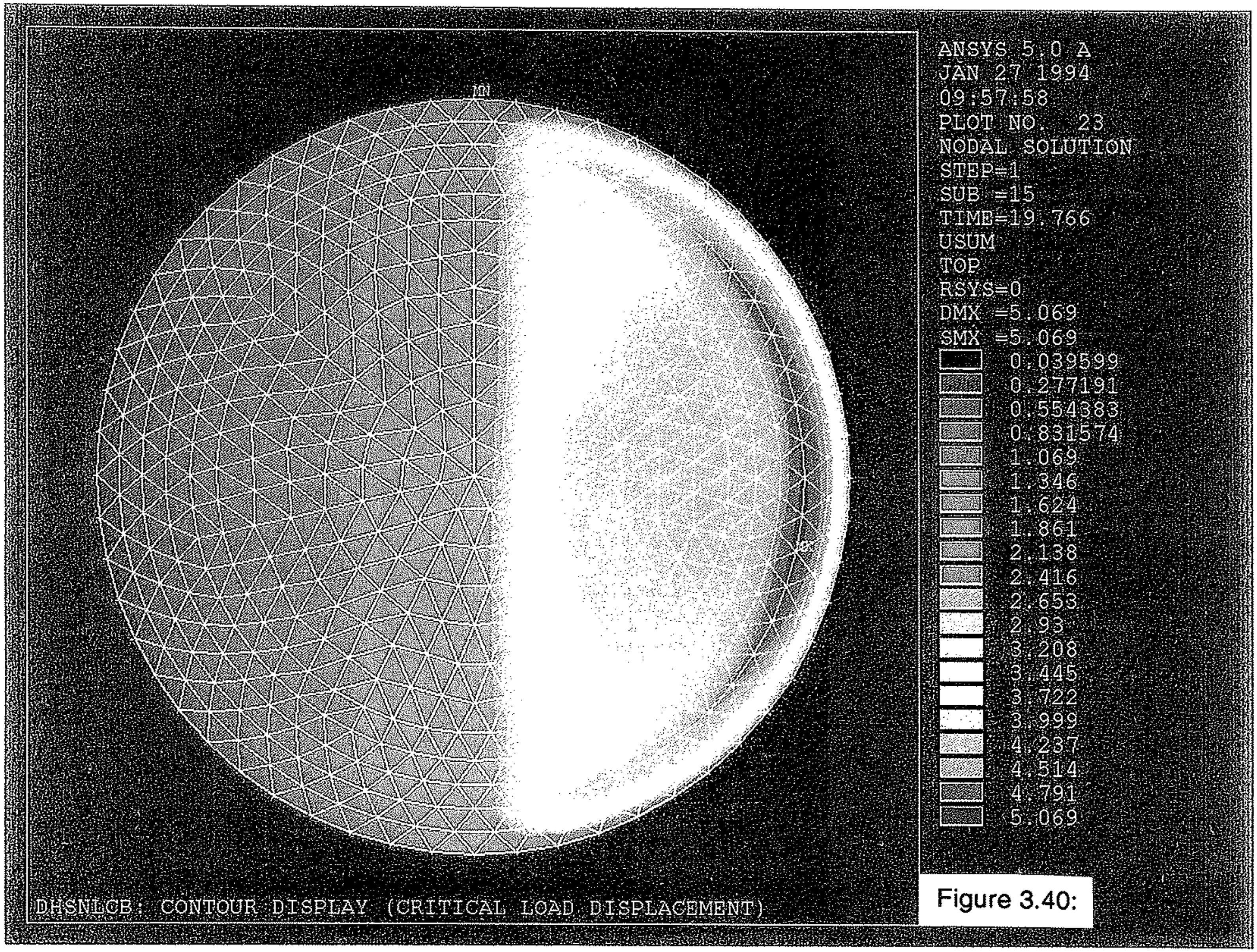
ANSYS 5.0 A
JAN 27 1994
09:57:58
PLOT NO. 23
NODAL SOLUTION
STEP=1
SUB =15
TIME=19.766
USUM
TOP
RSYS=0
DMX =5.069
SMX =5.069
0.039599
0.277191
0.554383
0.831574
1.069
1.346
1.624
1.861
2.138
2.416
2.653
2.93
3.208
3.445
3.722
3.999
4.237
4.514
4.791
5.069
MN
MX
DHSNLCB: CONTOUR DISPLAY (CRITICAL LOAD DISPLACEMENT)

Figure 3.40:

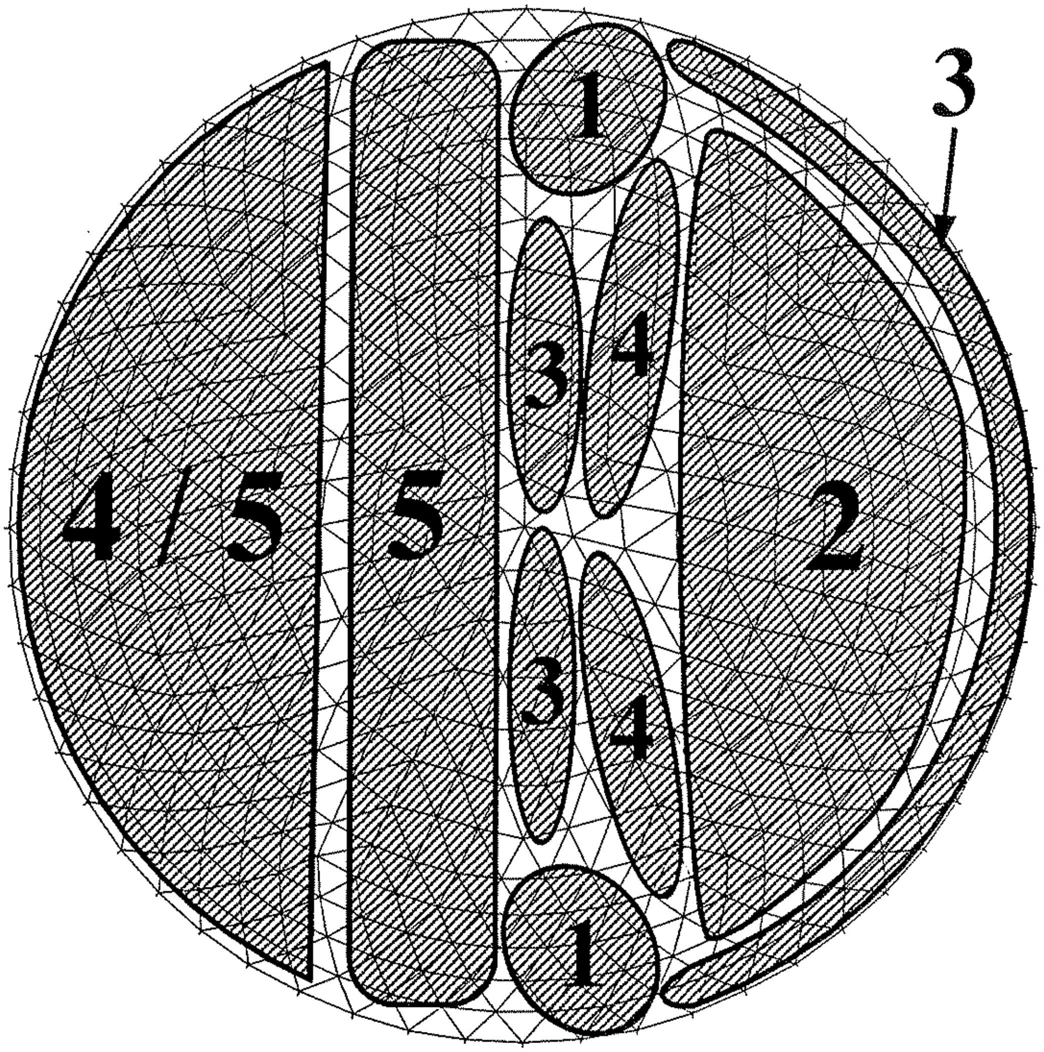

Max Comp (1) Transition Segments near N & S ends

↕ (2) East face midheight ring segments

(3) Upper diagonals on N - S meridian line, lower loaded diags

~0 (4) "Negligible" comp: Lower diags on unloaded surface

↕ (5) Lower unloaded ring segments, N - S oriented members

Max Tens Base Tension Ring

Figure 3.41: DHSNLCB Axial Stress Distribution (Critical Load)

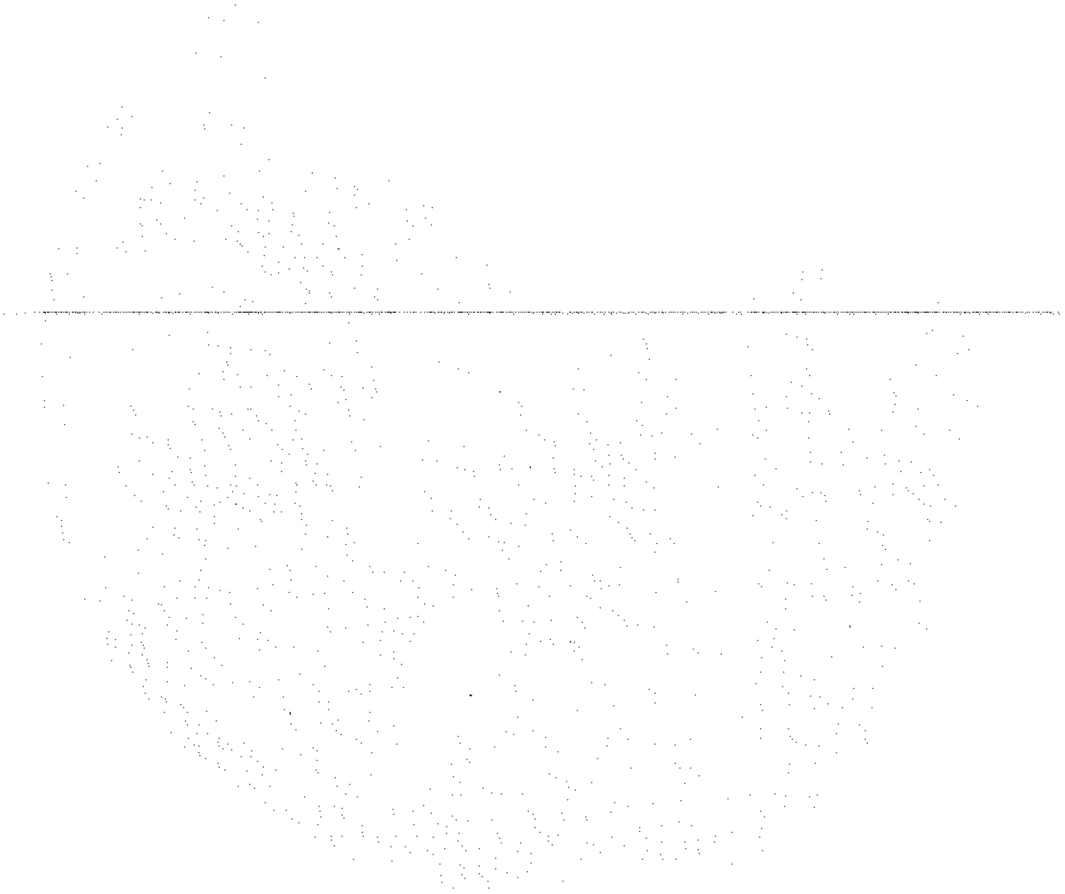

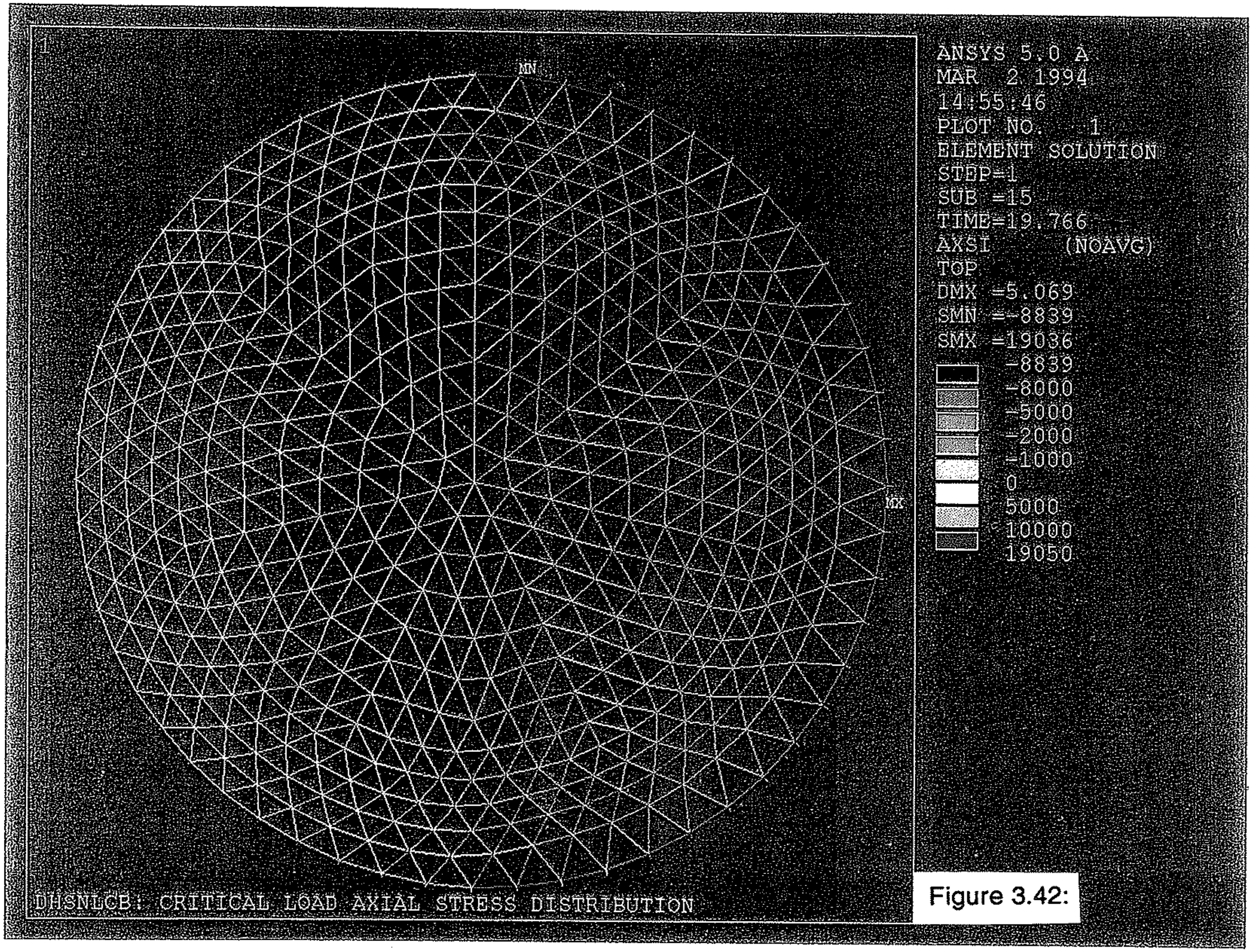
1
MN
MX
ANSYS 5.0 A
MAR 2 1994
14:55:46
PLOT NO. 1
ELEMENT SOLUTION
STEP=1
SUB =15
TIME=19.766
AXSI (NOAVG)
TOP
DMX =5.069
SMN =-8839
SMX =19036
-8839
-8000
-5000
-2000
-1000
0
5000
10000
19050
DHSNLCB: CRITICAL LOAD AXIAL STRESS DISTRIBUTION

Figure 3.42:

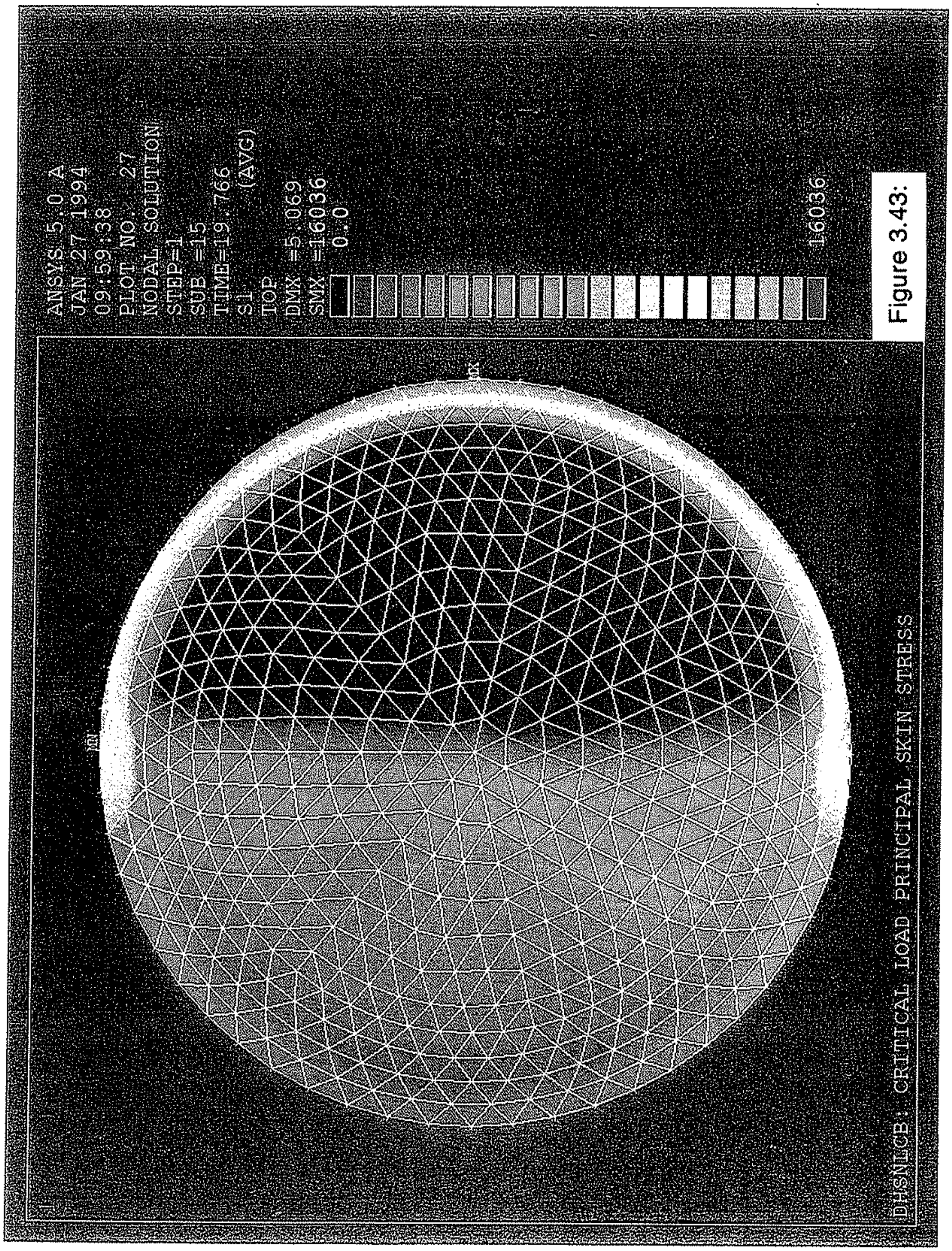
ANSYS 5.0 A
JAN 27 1994
09:59:38
PLOT NO. 27
NODAL SOLUTION
STEP=1
SUB =15
TIME=19.766
S1 (AVG)
TOP
DMX =5.069
SMX =16036
0.0
16036
MX
MN
DHSNLCB: CRITICAL LOAD PRINCIPAL SKIN STRESS

Figure 3.43:

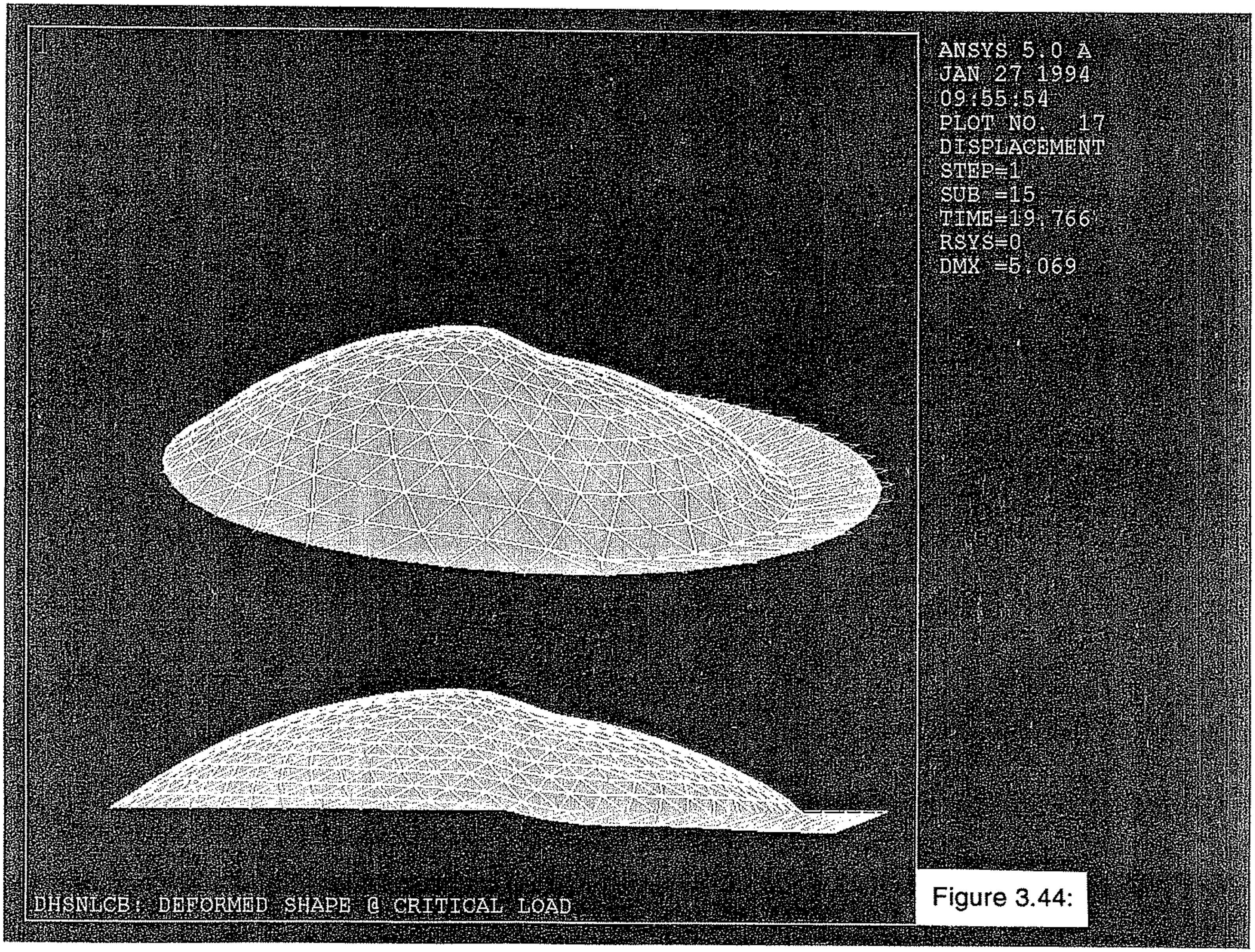
1
ANSYS 5.0 A
JAN 27 1994
09:55:54
PLOT NO. 17
DISPLACEMENT
STEP=1
SUB =15
TIME=19.766
RSYS=0
DMX =5.069
DHSNLCB: DEFORMED SHAPE @ CRITICAL LOAD

Figure 3.44:

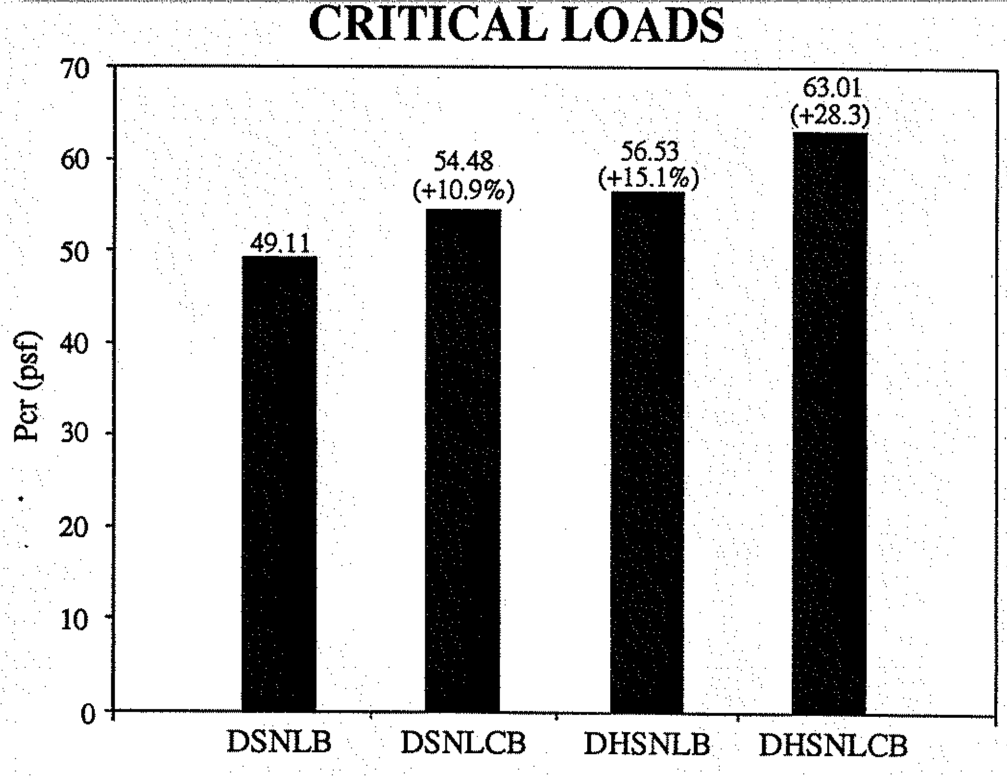

Figure 3.45: FEM Critical Buckling Loads

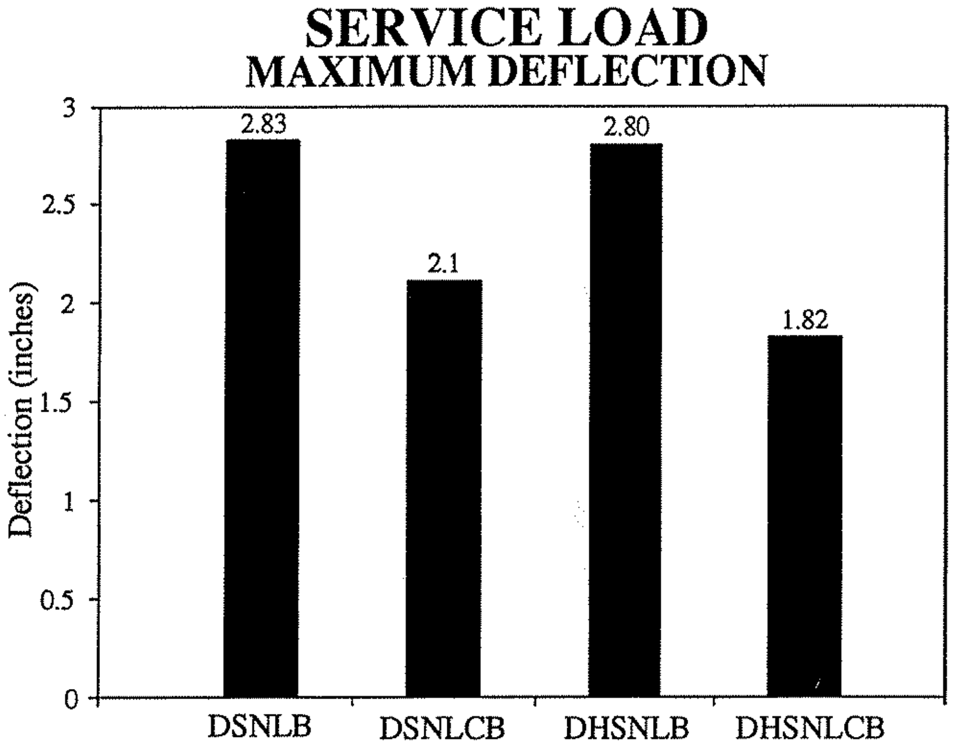

Figure 3.46: Max. Nodal Deflection Under Service Load

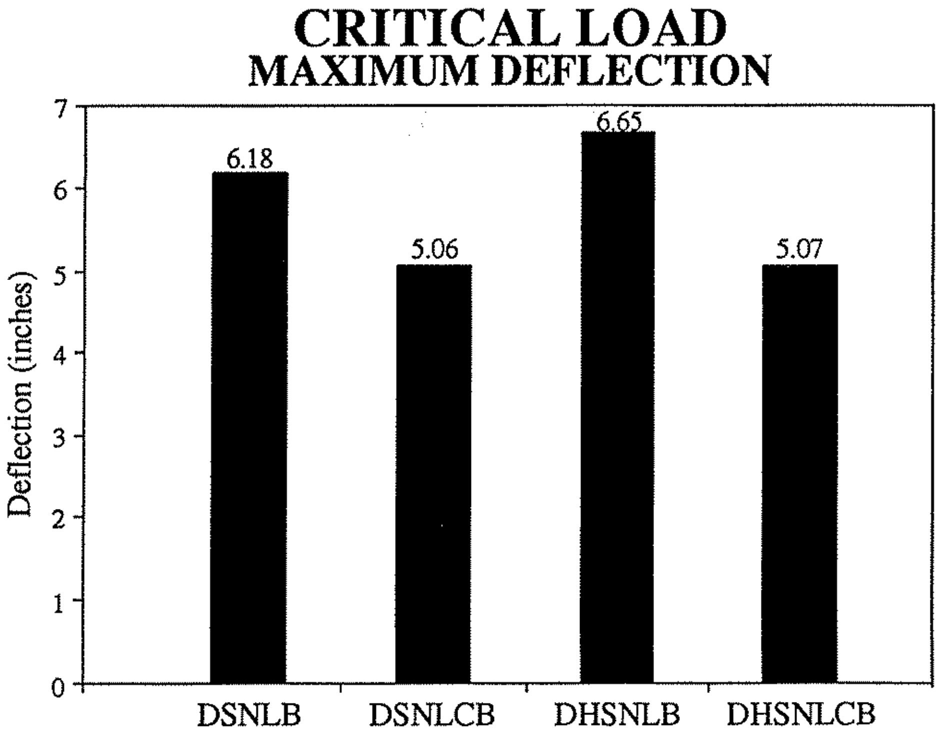

Figure 3.47: Max. Nodal Deflection Under Critical Load

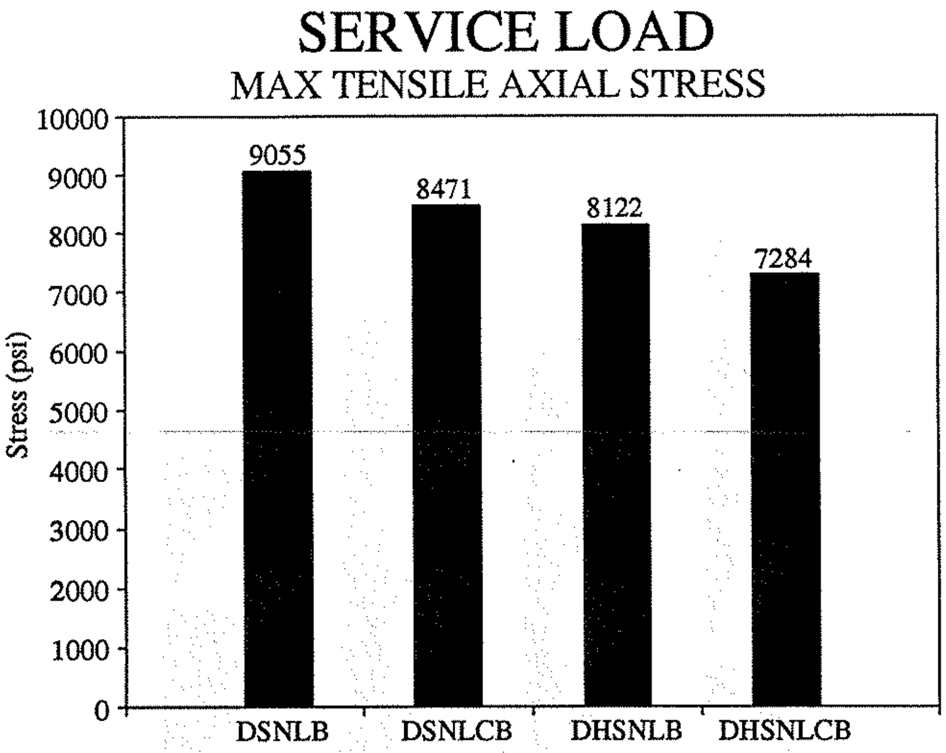

Figure 3.48: Max. Strut Tensile Axial Stress Under Service Load

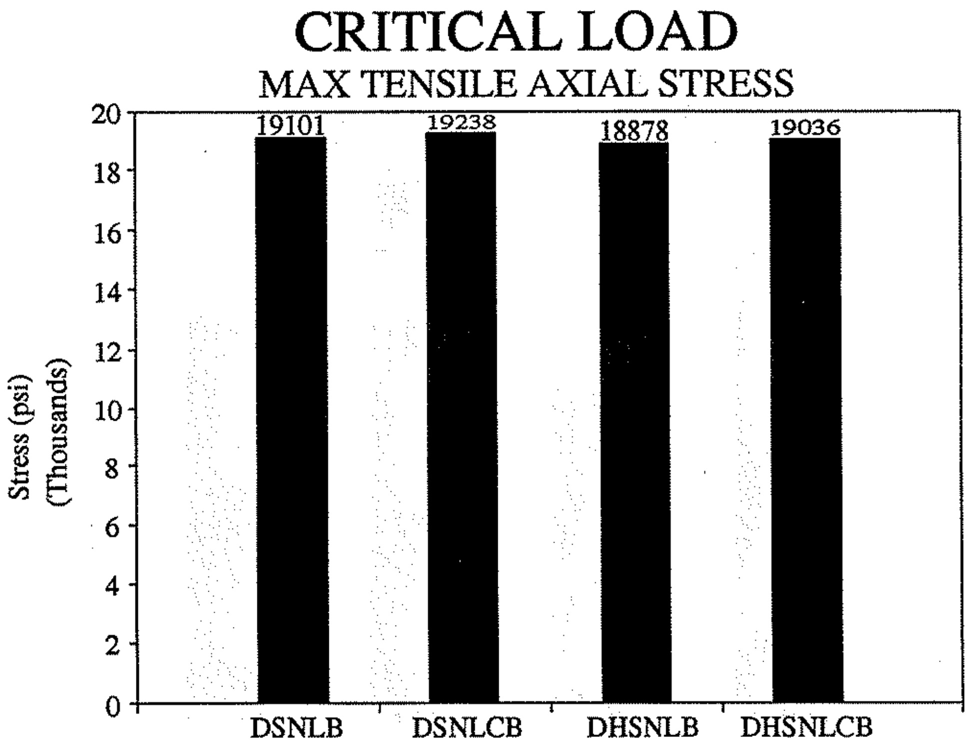

Figure 3.49: Max. Strut Tensile Axial Stress Under Critical Load

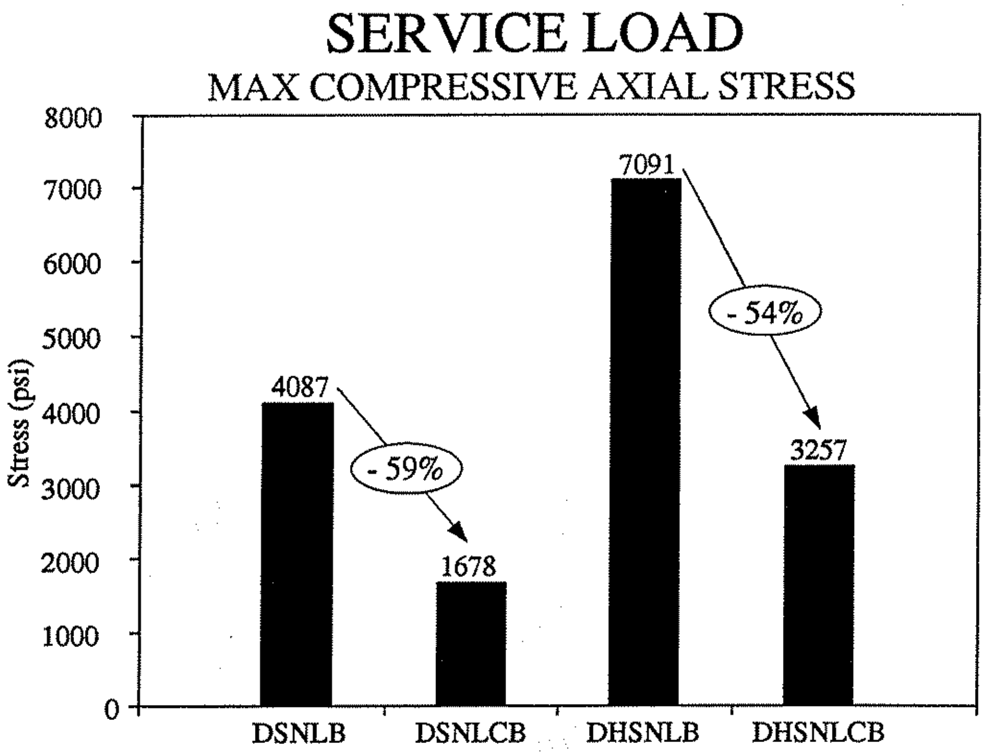

Figure 3.50: Max. Strut Compressive Axial Stress Under Service Load

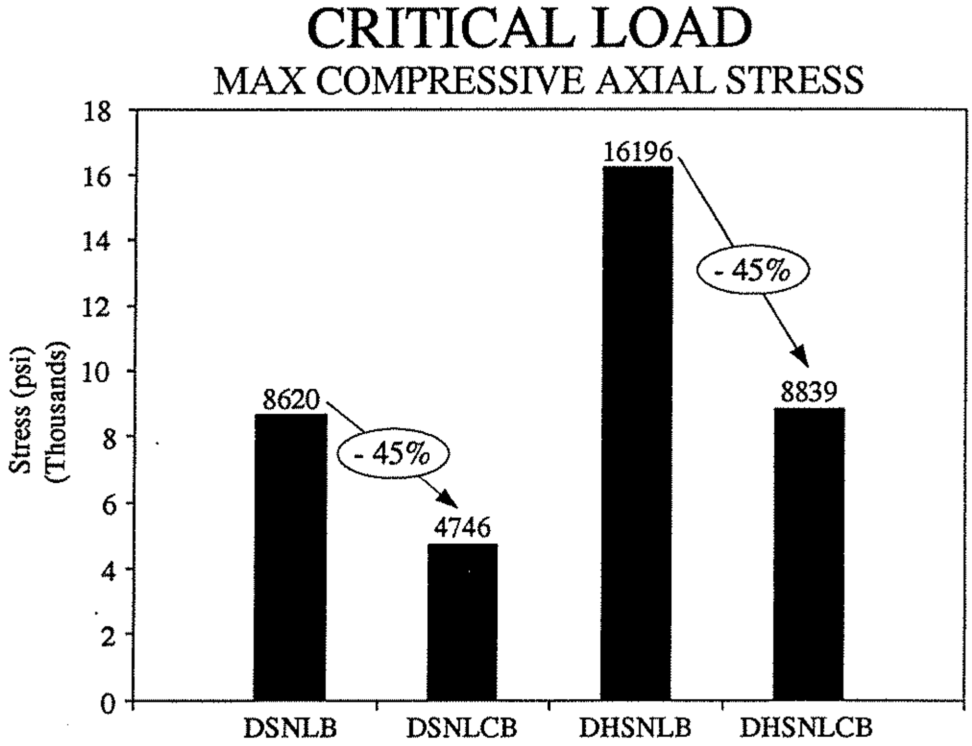

Figure 3.51: Max. Strut Compressive Axial Stress Under Critical Load

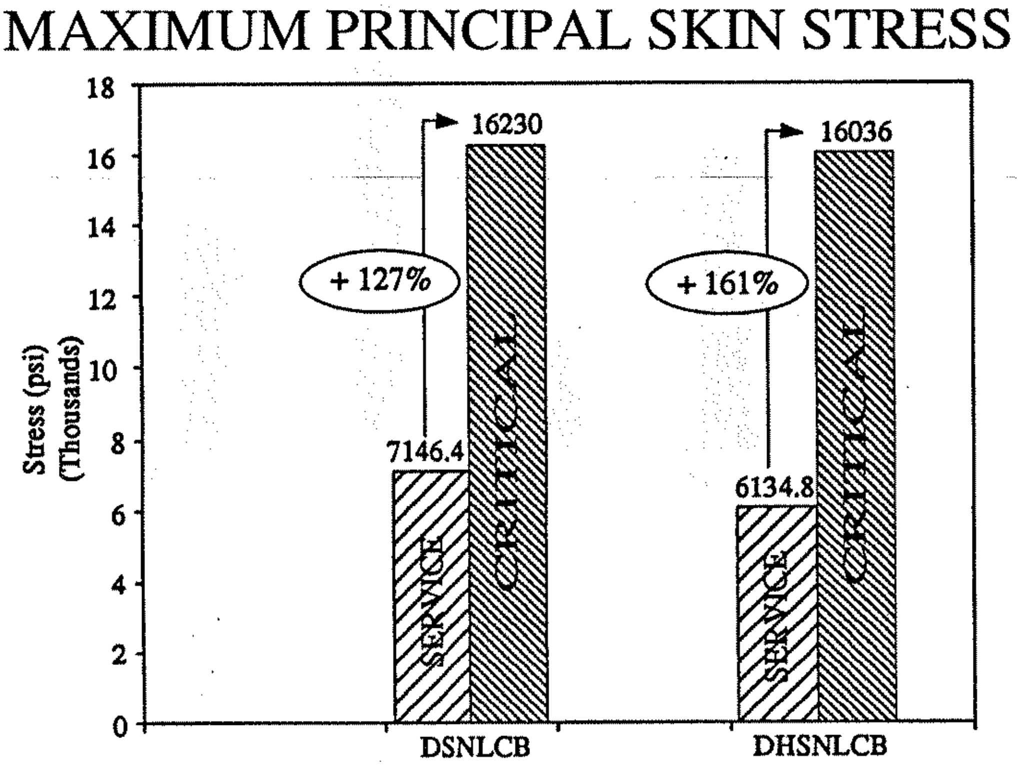

Figure 3.52: Maximum Tensile Membrane Stress Levels

4. CRITICAL BUCKLING EQUATION MODIFICATION

4.1 BACKGROUND

The method of designing the aluminum geodesic dome, as performed by Conservatek Industries, Inc., is to make use of the Wright / Buchert critical buckling equation presented in the first chapter, and through a series of trial-and-error iterations, select a dome geometry with a given selection of members which will satisfy the overall design equation.

Through the application of finite element analysis, it was found that the finite element model buckled at a load higher than that predicted by the equation. Therefore, the Wright / Buchert equation leads to a conservative dome design at service load levels. The following phase of the study will serve to develop and identify the trend between the "actual" finite element model and the theoretical critical buckling equation. The correlation between the actual and theoretical values will form the basis of a best curve fit. From this curve fit will result a modification factor which will encompass the difference in values, and in turn provide a more reasonable and efficient design.

4.2 ASSUMPTIONS

For the sake of clarity, the theoretical buckling equation is once again

$$P_{cr} = 1.55 \frac{AEr}{L_s R_s^2} \tag{4.1}$$

where

P_{cr} = Critical buckling pressure
A = Strut cross-sectional area
E = Modulus of elasticity of the material
r = Radius of gyration of the strut
L_s = Selected length of strut
R_s = Selected radius of curvature of the dome

It is important to understand the limitations of the equation with respect to its usage in a lattice-type formulation. This equation is merely an approximation based on equivalent shell theory, therefore there is no absolute relationship between mathematical theory and actuality pertaining to this study. The expression is more of an empirical formulation and, due to its empirical nature, there are many variables which are unintentionally ignored. The most obvious omission from the expression is the rise-to-span ratio of the dome. The only reference made to the overall geometry of the dome was the radius of curvature of the structure, which is independent of either the rise or the span of the dome. Another important factor which was not taken into consideration was the dome support condition. Support conditions play a major role in the performance of the dome. A fixed dome responds much differently than a slotted dome to arbitrary loading. The same can be said for a dome which has a steep slope at the base, as compared to a dome with a minimal edge slope. A blanket statement stating that the equation is valid only for shallow shell formulation was made to cover these and other shortcomings.

Weaknesses on a less global level are just as numerous. There is no reference to the degree of joint fixity, and there is no factor representing the number of members in the dome. It appears that the equation does not concern itself with the transitioned pattern of the geodesic dome, which was most likely the reason behind the conservative nature of the theoretical buckling load. The equation tends better toward a shell surface which has a regular pattern such as the triangulated arrangement within the upper 2/3 of the dome. The only member properties which are included in the equation are the cross-sectional area, radius of gyration, and average length of the members.

For this study, a number of assumptions must be made. First, it is assumed that this dome is a shallow structure (rise-to-span < 0.2), making it "reasonable" to use the above equation. The dome which serves as the benchmark structure for this modification is that analyzed in section 3. The forthcoming modified equation is truly valid for a strut length-to-spherical-radius (L/R) ratio of 0.06. In other words, any dome which is scaled to similar dimensions as the modeled dome would be governed by the modified equation. Also, the unmodified equation actually represents buckling pressure, acting normal to the surface. Therefore, based on small angle theory, it is assumed that the normal to the surface of the dome is close to vertical. Since the dome is of a shallow nature, the vertical loading of the model closely represents the pressure load indicated by the expression. Engineering judgement would indicate that this equation could be used to design domes with varying strut-to-radius ratios, but in order to validate such an assumption, additional finite element runs incorporating variable geometries must be made. Only then can the modified expression be used without hesitation for domes with different geometric properties.

4.3 MODIFICATION FORMULATION

As seen in Figures 4.1 and 4.2, the use of the unmodified equation tends itself toward many permutations, when considering parameters such as member length and dome radius. The scenario which most closely represents the "true" Conservatek Alumadome is reflected in Figure 4.2. The pattern of the geodesic dome consists of unchanged member lengths, regardless of the size of the dome. When a larger dome is required, the additional surface area is compensated for by adding members, and vice versa for a smaller dome. When the model geometry was incorporated into the unmodified equation (Figure 4.2(b)), the resulting curve fell below the curve for strut group 483. Group 483 defines the strut size which defines the upper 4/5 of the actual dome.

The next logical step in the modification was to run a series of analyses in order to ascertain an analytical curve defining the critical buckling load which, in turn, could be compared to the theoretical model curve. Since the nodal geometric pattern was given for only one dome, the pattern could not be manipulated, yet it could be scaled up or down in size. Therefore the analyses which were run represented the scaled versions of the benchmark dome. Figure 4.3 shows the correspondence between the model and theory. The data points representing the critical buckling load of the model were transformed into a function by applying a curve fitting technique to the sample space, resulting in the continuous function displayed in Figure 4.4.

$$P_{cr}(psf) = -17.6 - (\frac{1.25E{+}5}{R}) + (\frac{6.45E{+}8}{R^2}) \qquad (4.2)$$

where the spherical radius R is in inches. Equation 4.2 can be used for a quick approximation for determining buckling load for a dome with an L/R ratio of 0.06 and a selected strut cross-sectional area of approximately 3.5 inches. This L/R ratio is directly applicable to the Conservatek domes, for the ratio is indicative of domes with varying profiles and diameters. The change in profile and diameter is achieved through varying R. A larger value of R would represent a lower profile dome and a smaller R would indicate a higher profile dome. By maintaining a constant dome profile (rise-to-span ratio), a varying spherical radius would result in a dome with a different edge diameter. This geometrical technique allows for the analysis of domes with different diameters and common profiles, such as was done in this study.

In order to manipulate the unmodified expression into a more workable form for the purposes of the modification, certain mathematical relationships needed to be identified. Since the modified expression was to be formed upon the basis of a constant L/R ratio, then

$$\frac{R_s}{R} = \frac{L_s}{L} \qquad (4.3)$$

where R and L are the benchmark values of spherical radius and member length, respectively, and R_s and L_s signify the values of radius and member length of the scaled dome of interest.

By substitution of equation 4.3 into equation 4.1, the raw form of the workable equation is

$$P_{cr}=(1.55(\frac{L}{R})^{-1})\frac{AEr}{R_s^3} \tag{4.4}$$

The final form of this expression, with L/R = 0.06, is

$$P_{cr}=(25.83)\frac{AEr}{R_s^{3}} \tag{4.5}$$

where P_{cr} and E have consistent units. By approximating the finite element buckling load values with a cubic hyperbolic function, similar in form to equation 4.5, an expression which represents the modified form of the Wright/Buchert equation can be formulated. This equation is:

$$P_{cr}=20.98\frac{AEr}{R_s^3} \tag{4.6}$$

where P_{cr} and E again have consistent units. This formula represents an alternative mathematical relationship for the buckling load of the scaled profile geodesic dome with a rise-to-span ratio of 0.20 and L/R ratio of 0.06, based on the finite element buckling load values.

To obtain P_{cr} in psf when using E in usual units of ksi, equation 4.6 has the alternative form (Figure 4.5):

$$P_{cr}(psf)=3.02E{+}6\ \frac{AEr}{R_s^3} \tag{4.7}$$

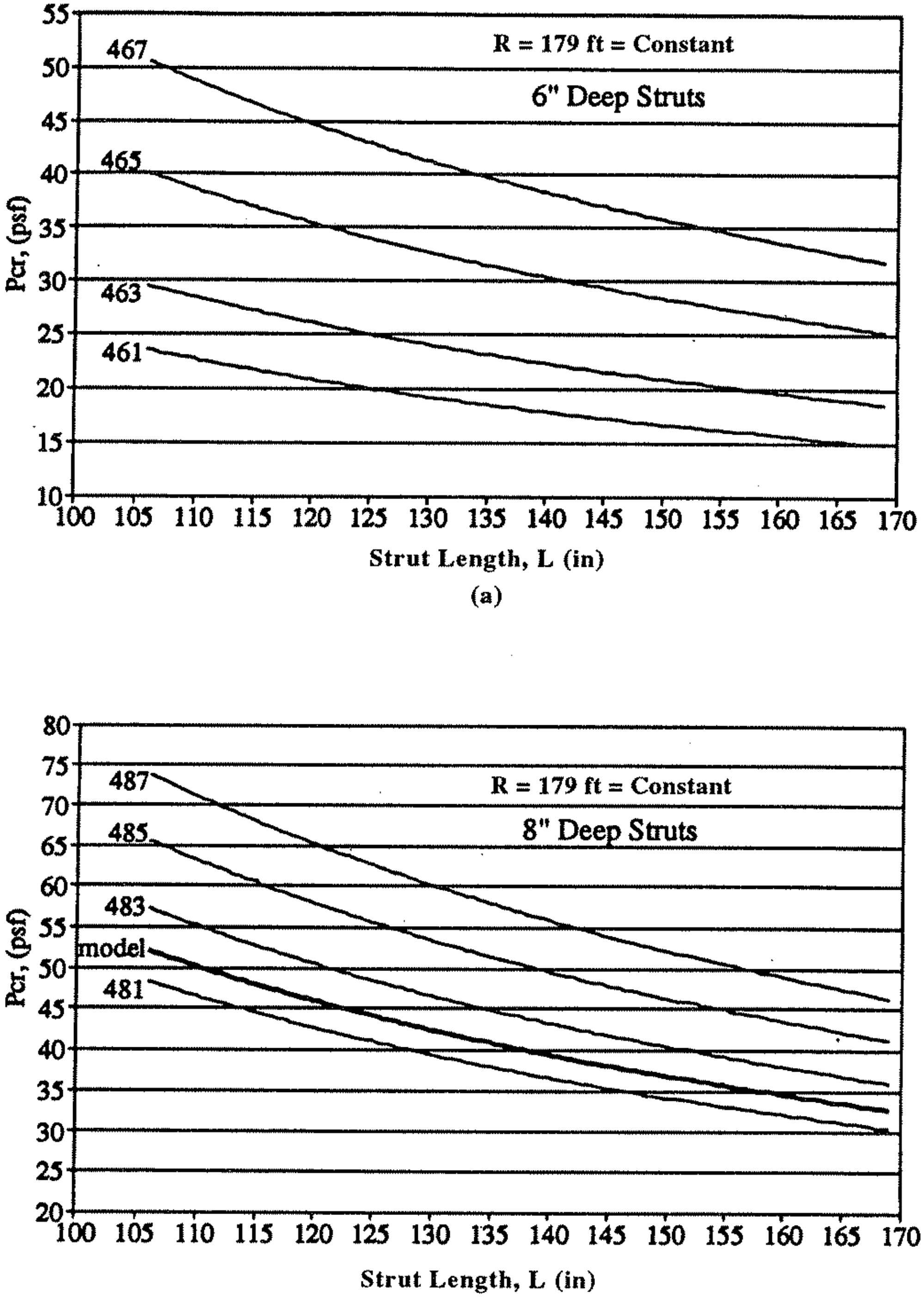

(b)

Figure 4.1: Wright / Buchert Critical Buckling Pressures vs. Strut Length

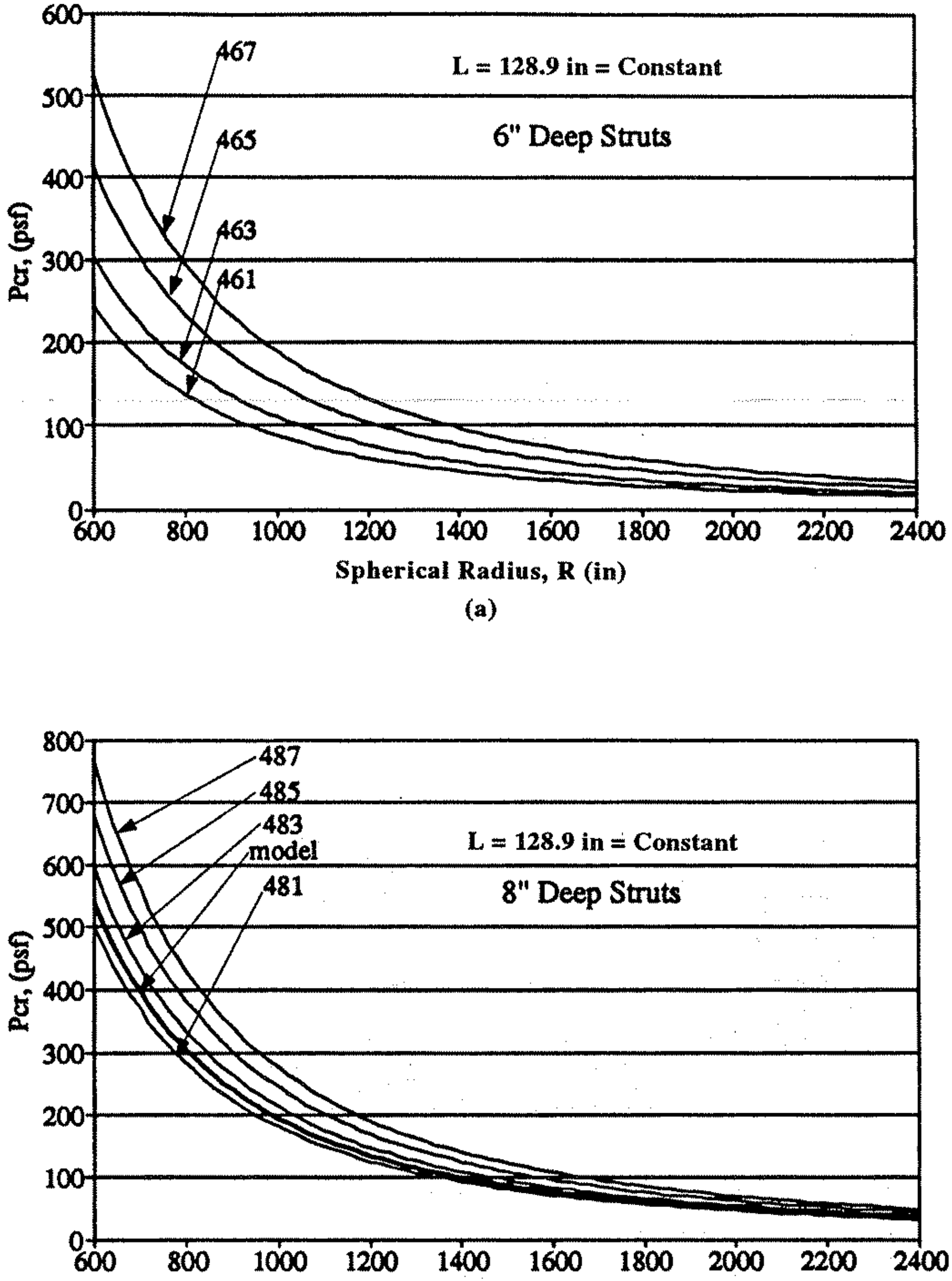

(a)

(b)

Figure 4.2: Wright / Buchert Critical Buckling Pressures vs. Spherical Dome Radius

Critical Buckling Loads

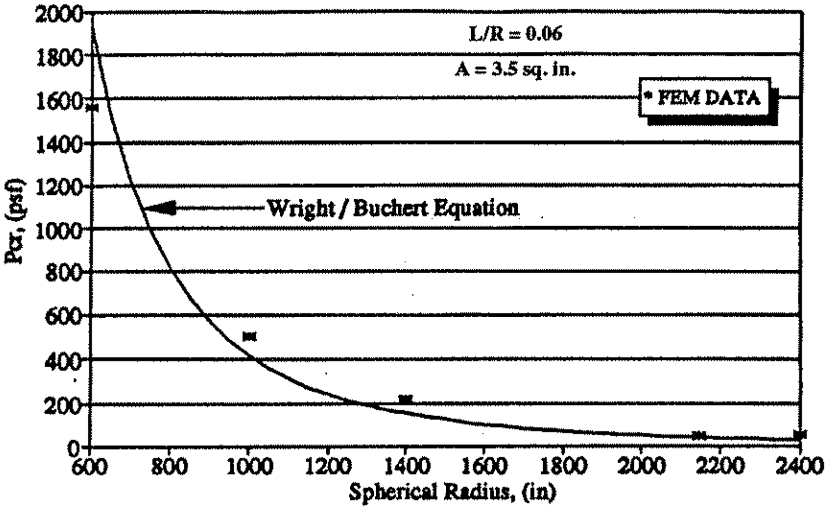

Figure 4.3: Correlation Between Wright/Buchert Equation and FEM Buckling Loads

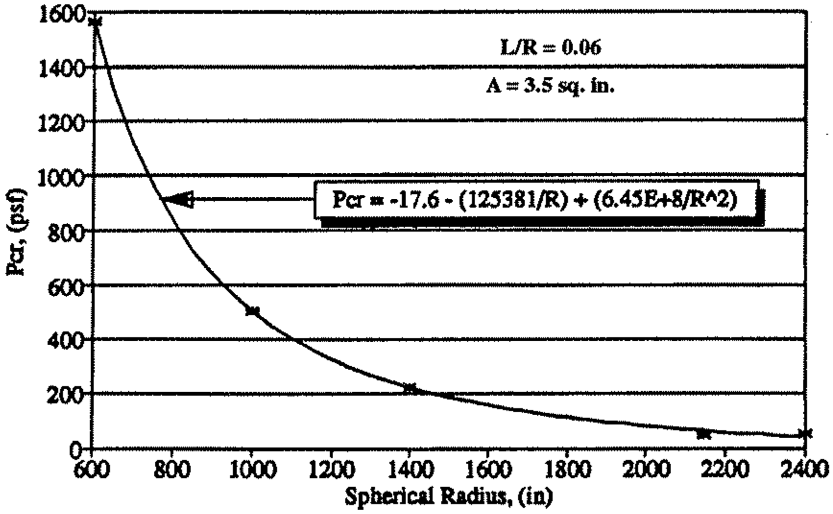

Figure 4.4: Continuous Function Approximation of FEM Buckling Loads

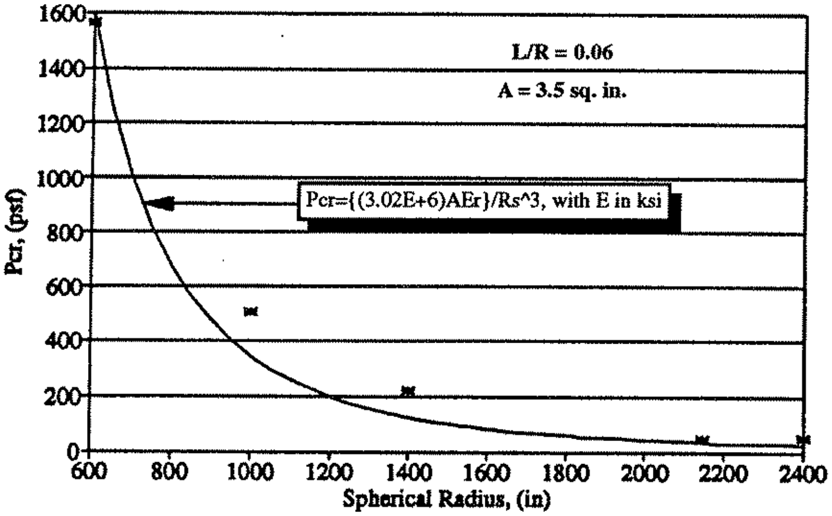

Figure 4.5: Cubic Hyperbolic Function Approximation of FEM Buckling Loads

5. SUMMARY

5.1 CONCLUSIONS

Advances made in the analysis of single layer lattice geodesic domes have been quite limited within the past few decades. Since the early 1960's, there has not been any major advance corresponding to dome analysis, with the exception of finite element modeling. As far as mathematical models are concerned, there are mainly two distinct areas of concentration, continuous and discrete models. Continuous mathematical models are reflected through classical conventional shell theory, equivalent shell theory, and the split rigidity method. Discrete mathematical models, formulated through finite difference and matrix methods, are cumbersome, therefore lending themselves quite conveniently to computer-based finite element analyses.

The use of finite element packages is most advantageous when attempting to interpret the critical performance of geodesic domes, such as the dome analyzed in section 3. The use of the **ANSYS** finite element program enabled the critical load of a particular geodesic dome to be determined. The particular dome highlighted within the study was modeled as both a bare-frame structure and a cladded structure, with snow load applied over both the full surface and a half surface. Results of the modeling showed that the bare frame dome with full snow load buckled at the lowest snow load, thus making it the most critical configuration of those studied. Although this case was the most critical of the four cases, it still exhibited a factor of safety of 1.95 above the service load, which is quite reasonable for domelike structures.

Expanding the interpretation of the critical performance of the geodesic dome, the finite element buckling loads can be used to modify the expressions used to design these complicated structures. For example, the Wright / Buchert critical buckling pressure expression is an empirically based formulation, which leaves it susceptible to differing engineering opinions on values contained within the equation. By developing a family of models, a reasonable modification of the buckling expression can be achieved. Although the modification results in an equation which seems to fit the data reasonably well, the expression is limited to a specific geometry.

The two curves which were fit to the data approximated the critical load of the L/R=0.06 family of domes fairly well. As seen in Figure 5.1, the rational approximation function fits the data better than the cubic hyperbolic function, although it is nonconservative with respect to the Wright / Buchert curve for domes with spherical radii greater than 800 inches. The cubic hyperbolic approximation is a safer modification due to the fact that the function yields critical design loads consistently lower than the Wright / Buchert curve for the entire size range of domes of the particular profile. Nonetheless, by applying the approximation which best fits the finite element model data, a structurally efficient dome design can be detailed, contributing to a savings in materials.

5.2 RECOMMENDATIONS

Due to the empirical nature of the Wright / Buchert critical buckling pressure equation, there are certain factors that are not fairly addressed within its context. This leaves much room for further study of the expression. The major areas open for further research are:

1) Development of an entirely nonempirical expression for buckling load incorporating a thorough set of geometric parameters, i.e. rise-to-span ratio, number of members, joint conditions (degree of fixity), and pattern of members.

2) Development of a complete family of curves using a modified Wright / Buchert expression encompassing numerous combinations of dome profiles, dome sizes, member sizes, and support conditions.

3) Full-scale experimental work to validate the finite element dome models.

4) Experimental / finite element research focusing on the issues of joint fixity and boundary conditions and their effect upon critical dome performance.

5.3 CLOSING COMMENTS

Although the finite element model used to interpret the structural performance of the geodesic dome in this study was thoroughly checked for proper accuracy, options do exist which would make the model even more accurate. Due to symmetry, a portion, or "slice" of the model could have been modeled. As a result, the complexity of the model would be drastically reduced, allowing for the connector hubs to be properly modeled. Although the joint fixity issue still remains unresolved, this particular finite element study, coupled with new experimental work focusing on testing the structural parameters of the connector hubs would allow for an increased understanding of the fixity problem. Finite element results are always most conclusive when experimental work is done to verify the model.

An additional area of study is to model this dome via **ABAQUS** or **ADINA** which was mentioned previously in section 2.4. By analyzing "identical" models through different finite element platforms, the emergence of different solutions would be a definite possibility. As shown by Temcor's finite element analyses of the South Pole dome [21], finite element runs of the same structure using different analysis packages or solution techniques lead to results which are not identical.

Finally, it can be stated that for domes of similar profile to the ones in this study the original Wright / Buchert formulation is evidently conservative for spherical radii greater than 800 in.

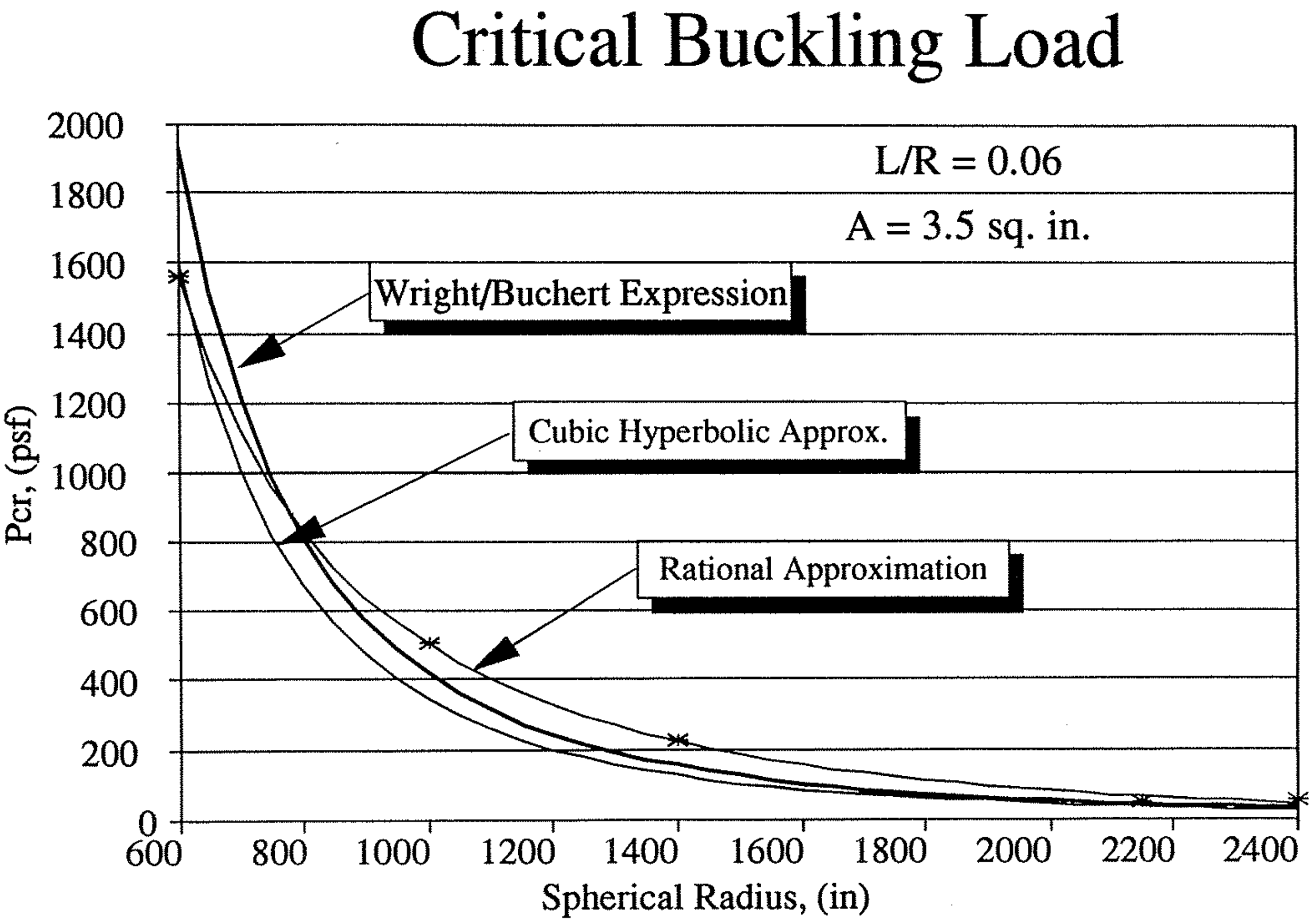

Figure 5.1: Comparison Between Approximate Functions and Wright / Buchert Expression

REFERENCES

(1) Aguilar, R.J. (April, 1967). "Snap-Through Buckling of Framed Triangulated Domes." Journal of the Structural Division. ASCE, Vol. 93, No. ST2. pp. 301 - 315.

(2) American Society of Civil Engineers. (1990). Minimum Design Loads for Buildings and Other Structures, ANSI/ASCE 7-88. New York, NY.

(3) Analysis, Design, & Realization of Space Frames. (1985). Bulletin of the International Association for Shell and Spatial Structures.

(4) Swanson Analysis Systems, Inc. ANSYS User's Manual (Revision 5.0). (1992). Houston, PA.

(5) Bathe, K-J. (1982). Finite Element Procedures in Engineering Analysis. New Jersey: Prentice Hall.

(6) Buchert, Kenneth P., PhD, P.E. (1973). Buckling of Shell & Shell-Like Structures- For Engineers, Architects, Fabricators, Builders, and Designers. Columbia, Missouri: K.P. Buchert & Associates.

(7) Buchert, K.P. (October, 1965). "Buckling of Framed Domes." Engineering Journal of the American Institute of Steel Construction. Vol. 2, No. 4. pp. 120 & 121.

(8) Buchert, K.P. (June, 1965). "Discussion of Membrane Forces and Buckling in Reticulated Shells." Journal of the Structural Division. ASCE, Vol. 91, No. ST3. pp. 298 & 299.

(9) Buchert, K.P. (July, 1964). "Stiffened Thin Shell Domes." Engineering Journal of the American Institute of Steel Construction., Vol. 1, No. 3. pp. 78 - 82.

(10) Chen, W.F. & Lui, E.M. (1987). Structural Stability Theory and Implementation. New Jersey: Prentice Hall.

REFERENCES (continued)

(11) Cook, R.D., Malkus, D.S., & Plesha, M.E. (1989). Concepts and Applications of Finite Element Analysis. (3rd ed.). New York: John Wiley & Sons.

(12) Crooker, J.O. & Buchert, K.P. (March, 1970). "Reticulated Space Structures." Journal of the Structural Division. ASCE, Vol. 96, No. ST3. pp. 687 - 699.

(13) Galambos, T.V. (1988). Guide to Stability Design Criteria for Metal Structures. 4th Ed., New York: John Wiley & Sons.

(14) Hibbitt, Karlsson, and Sorenson, Inc. (1993). ABAQUS Theory Manual. (Version 5.3) Providence, RI.

(15) Li, S. (Dec., 1962). "Metallic Dome-Structure Systems." Journal of the Structural Division. ASCE, Vol. 88, No. ST 6, Proc. paper 3358. pp. 201 - 227.

(16) Litle, William A. (1964). Reliability of Shell Buckling Predictions, Research Monograph No. 25. Cambridge, Massachusetts: M.I.T. Press.

(17) Makowski, Z.S. (1984). Analysis, Design, and Construction of Braced Domes. New York: Nichols Publishing Co.

(18) Narayanan, R. (Ed.) (1985). Shell Structures Stability and Strength. New York: Elsevier.

(19) Ramm, E. (1980). "Strategies for Tracing Nonlinear Response Near Limit Points." Non-Linear Finite Element Analysis in Structural Mechanics. Bochum, G.F.R. pp.63-89.

(20) Rapp, E.R. (Nov., 1961). "Space Structures in Steel." Architectural Record. pp. 190 -195.

REFERENCES (continued)

(21) Richter, D.L. (1975). "Temcor Space Structures Development." Proceedings of the Second International Conference on Space Structures. New York: Elsevier. pp. 1019 - 1024.

(22) Stauffer, C.D. (Apr., 1992). "Nonlinear Buckling Analysis of the Arena Auditorium Located in Laramie, Wyoming," Project Paper for Civil Engineering Course No. 5210, University of Wyoming, Laramie, WY.

(23) Sumec, Jozef (1990). Regular Lattice Plates and Shells. New York: Elsevier Science Publishing Co. Inc.

(24) The Aluminum Association. (1959). Aluminum Construction Manual. New York, NY.

(25) The Aluminum Association. (1972). Aluminum Construction Manual, Section 3: Engineering Data for Aluminum Structures. (2nd ed.). New York, NY.

(26) The Aluminum Association. (1976). Aluminum Construction Manual, Aluminum Standards and Data. (5th ed.). New York, NY.

(27) The Subcommittee on Latticed Structures of the Task Committee on Special Structures of the Committee on Metals of the Structural Division. (July, 1972). "Bibliography on Latticed Structures." Journal of the Structural Division. ASCE, Vol. 98, No. ST7. pp. 1545 - 1566.

(28) The Task Committee on Latticed Structures of the Committee on Special Structures of the Committee on Metals of the Structural Division. (Nov., 1976). "Latticed Structures: State-of-the-Art Report." Journal of the Structural Division. ASCE, Vol. 102, No. ST11. pp. 2197 - 2229.

(29) Timoshenko, S.P. & Goodier J.N. (1982). Theory of Elasticity. (3rd ed.). New York: McGraw-Hill. pp. 515 - 550.